The University of Nottingham

UNITED KINGDOM · CHINA · MALAYSIA

Performance Calculation of High Speed Solid Rotor Induction Machine

Luca Papini

Thesis submitted to the University of Nottingham
for the degree of Doctor of Philosophy

July 2017

To my family

To Carmel, Luca, Ale, Savvas, Con

and all the friends and colleagues that supported me

To Prof. Francaviglia

ABSTRACT

Solid rotor induction machines are suitable for applications which require robustness, reliability and high rotational speed. A literature review of high speed technologies is initially presented. The current limitation and challenges are detailed based on a wide collection of data. The multi-physics aspect related with electrical machines for high speed applications are discussed providing a summary of the current state of the art. The main aim of the research was to develop a multi-physic computational environment for the design and analysis of solid rotor induction machines. The electromagnetic, thermal, structural and rotor dynamics models have been developed targeting reduced computational time and accurate predictions. Numerical techniques are proposed based on the discretisation of the computational domain. The different disciplines are linked together providing a flexible and powerful tool for the characterisation of solid rotor induction machine. Another objective was to investigate the impact of the rotor material on the electromagnetic performances of the machine. Finite Element simulation are used to account for the non linear magnetic properties. The impact on the equivalent circuit parameter is discussed and general criteria for material selection presented. Three dimensional finite element calculation are performed targeting the validation of the end region correction factor and select the rotor length. The performances of a $120\,[kW] - 25000\,[rpm]$ solid rotor machine are compared with a caged rotor induction machine for waste heat recovery application.

CONTENTS

LIST OF FIGURES

LIST OF TABLES

CHAPTER

ONE

INTRODUCTION

Emission regulations and technological innovations have increased the demand of high speed electrical machines and direct drive system. The worldwide trend towards stricter emission standards and high efficiency drive system have focused the research of academia and industry into high speed machines for a wide range of applications. Emission regulations have pushed the automotive, naval, and aerospace markets towards more electric systems resulting in hybrid and full electric road-vehicle technology [2], more electric aircraft (MEA), and full electric aircraft (FEA) [3]. The introduction of wideband SiC and GaN switching device has lead the growth rate of switching frequency capabilities in power electronics modules and subsequently the research effort in increasing the operative speed of electrical machines [4]. High switching frequency, mono-directional and regenerative power converters enable the introduction of high speed drives to replace or complement existing high speed mechanical systems. Innovation in manufacturing processes and the material technology research has provided high performing material for both the electromagnetic and mechanical aspects. The combination of these factors justify the effort of researchers worldwide to increase the rotational speed in electrical machines. High speed machines are currently used for a wide range of power and speed ratings [5, 6]. Among all the electrical machines topologies adopted in high speed drives, the robustness, reliability, low manufacturing cost, and the capability of harsh environment operation make induction machines suitable for both heavy duty and niche applications [7, 8]. The robustness of the rotating element in solid rotor induction machines (SRIM) is of particular interest when the current material technology impose limits to the maximum peripheral speed that can be achieved with a laminated rotor structure. An overview of the machine topologies, technology adopted, applications and materials implemented for high speed applications are presented in the sections below.

1.1 High Speed Technology: Review

High speed technology has gained interest in the industrial and academic environment for a wide range of applications. The increasing efficiency, high power-to-weight ratio as well as power-to-volume ratio required in many environments has pushed innovation and focused research on the related issues of high speed technology. The definition of *high speed* requires the electromagnetic aspect of electrical machines to be complemented with a combination of factors that includes rotor dynamics, mechanical, thermal, fluid-dynamics, and material performances. Various studies have proposed quantitative analysis of high speed machines [7, 9–11], introduced factors to describe the severity in achieving power-speed nodes [9, 10, 12], and investigated the main challenges in high speed electrical machines. The flexibility of the design parameters and performances of high speed machines identifies the current trend for different applications and therefore different power-speed nodes. Industry is increasingly taking advantage of the high speed technology in the low power range as well as high power. The main limitations in achieving more challenging power-speed nodes is discussed according to the design parameters, cooling techniques, bearing technology, and materials selected.

In the last decades, reviews concerning high speed electrical machine technologies have been published [4, 5, 7–11, 13–20]. In Figure 1.1, the prototyped high speed machines listed in the above mentioned reviews, in addition with the most recent data found in literature, are collected together and presented in a $log_{10}(P_m) - log_{10}(\omega_m)$ double logarithm chart.

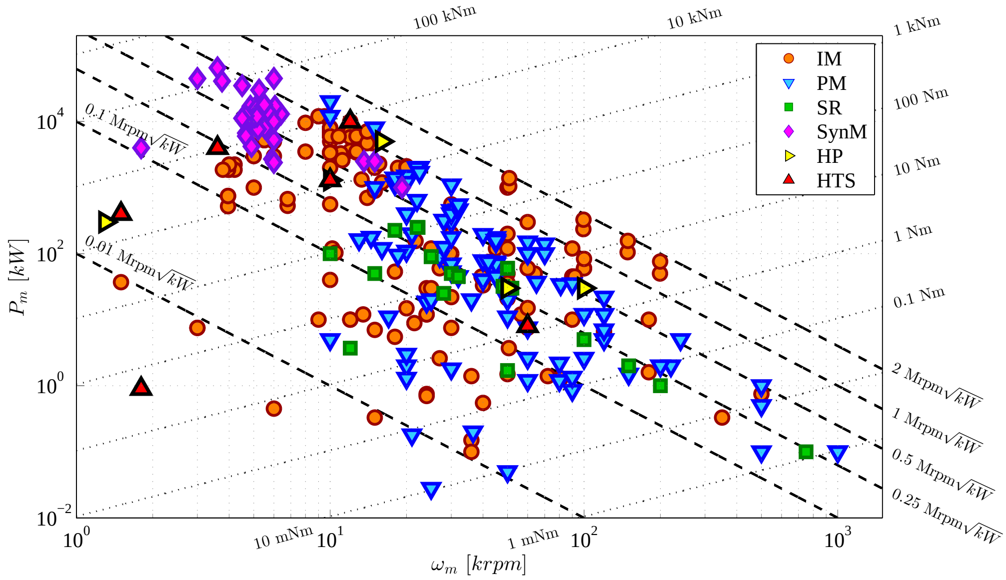

Figure 1.1: Power (P_m) against speed (ω_m) nodes of high speed technology from literature.

Induction machines (IM) and permanent magnet synchronous machine (PM) are the most common topology selected for high speed applications [5, 8, 9]. The mechanical robustness of IM equipped with a solid rotor structure can achieve high rotational speeds and high operative peripheral speeds. However, taking advantage of high tensile strength bandage material, the PM topology achieved challenging rotational speeds (e.g. $1\,[Mrpm]$ [21]). Furthermore, alternative topologies like switched reluctance (SR) and synchronous reluctance machine (SyRM) are becoming competitive in the market of high speed drives especially in the range of $10 \div 60\,[krpm]$, mainly being driven by the automotive and aerospace markets. Synchronous generators (SynM) are dominating the market in the multi-megawatt range ($> 5\,[MW]$). However, the induction machine is challenged in the megawatt range by PM machine technology which is a growing promising alternative. Examples of superconductive (HTS) and homopolar (HP) machines can be found as a technology benchmark presenting interesting results.

1.2 Application and Industry

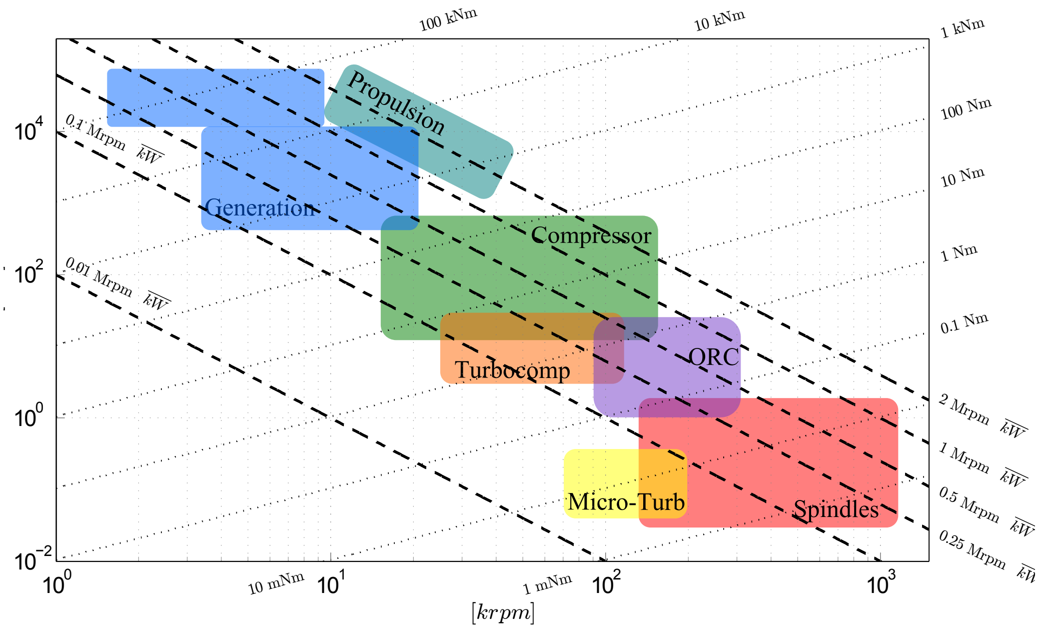

Figure 1.2: Power (P_m) against speed (ω_m) nodes and applications ranges.

The interest for high speed machines is spread across a wide power-speed range as presented in Figure 1.1. The selected operative points and environmental operating conditions are directly related to the application they are dedicated to. In Figure 1.2, the main applications and the power-speed range of interest is presented, while the technological applications are detailed below.

Examples of the MW range can be found in the Oil & Gas industry [22–25] where the high speed generator is directly coupled to gas turbines without a speed-gear, thus increasing the reliability of the overall system. The direct coupling of gas turbines with high speed generators enables the system to operate with higher efficiency in critical environments. High speed electric compression systems are an appealing oil-free solution for gas storage, transmission pipelines, and gas injection applications with reduced footprint and low maintenance. The integration and direct coupling of the motor and the compressor achieves a compact and efficient system where the cooling of the motor is performed by means of the process gas between each stage of the compressor [26]. The overall system efficiency, from the power source to the compressor, is increased whilst featuring lower maintenance, reduced installation cost, emission free, and oil free operation. The adoption of active magnetic bearings (AMB) enables the integration of the motor and the compressor, eliminating the shaft-end sealing system and reducing the auxiliaries for lube oil and cooling fluid [27].

High speed machines have found applications in energy recovery systems where the efficiency of an engine/generation system is increased extracting excess energy from the circulating fluid of the Organic Rankine Cycle (ORC) [28]. Examples of high speed machines applied to waste heat recovery systems can be found where high speed generators are coupled to high speed turbines to extract excess energy from the exhaust gasses (turbo-compounder) [29, 30]. Exhaust gas recirculation systems, aiming to reduce NO_x emission, can take advantage of a compressor driven by a high speed machine to overcome the problem arising from the differential pressure between inlet and outlet. In an internal combustion engine, high speed machines can be integrated in an electrically assisted turbocharger and used as generators during shaft speed control at high loads and as a motor in the starting condition to achieve the require operative speed. The flexibility of the system is therefore increased whilst also enhancing the efficiency.

The impact of mass and volume reduction that can be achieved by increasing the rotational speed is of particular interest in the automotive, railway and aerospace markets where fuel saving and emission reduction are key targets. The industrial interest in direct drive systems as a solution to enhance the power-to-weight ratio as well as the reliability and the efficiency, has pushed the increase of high speed machines in the automotive and aerospace industry [31, 32]. Turbocharger, turbo-compound, and micro-turbines [33] for automotive applications became an effective solution to increase the flexibility of the system and the efficiency. Some studies have also shown that a high speed flywheel can achieve comparable or even superior performance with respect to the battery technology for energy storage systems [19]. The high speed machine market has expanded to being the main propulsion system in the railway industry [34], including levitating systems. Both linear and rotatory induction machines currently dominate the market but research on novel topologies is driven by the growing need from the high speed railway industry.

Emission regulations are affecting the aerospace industry. The MEA concept has pushed aerospace companies to look into alternative technologies and different system arrangements to meet emission regulations for future transportation [35]. The concept of distributed power generation and energy storage on modern aircraft has identified high speed machines as the most suitable for such applications [36]. The advantage of high power-to-weight ratios, gear-less coupling, and oil free characteristics are pushing the research towards high speed generators, that can be directly coupled or integrated with thrust engines [37]. The increase in reliability is improving with more flexible power management thus increasing the overall system efficiency. The mechanical challenges that arise from the high peripheral speed that machines are required to withstand is combined with the critical thermal management problem in such applications.

In the low power range ($P_m < 10\,[kW]$), high speed machines find their application mainly in micro-turbines and nano-turbines [19], spindles machines [8, 38] and niche application such as air-knives. Spindles have been the pioneering applications for high speed machines and drives. The high rotational speed required to cut materials combined with the flexibility of variable speed drives has made high speed machines attractive for such applications. In order to increase high material removal rates, limit the cutting tool temperature rise, increase the accuracy, the quality and the efficiency of the work-piece manufacturing process and improve the stability of the rotating cutting tool, the spindle market has moved towards increased rotational speed power nodes. The compactness of high speed drives has opened the market to portable power generation systems where micro-turbines and nano-turbines are directly coupled with high speed generators [21]. The high power density and the flexibility to run on a variety of fuels make this technology very attractive in a constrained environment with limited available space. Particular manufacturing processes such as solar cells, dye chemicals, and semiconductors as well as in mass spectroscopy applications, CD, DVD, and hard disk production [39] requires clear, high vacuum environments which are often created with turbo-molecular pumps. The high rotational speed required to create and maintain the vacuum can be achieved by means of direct coupling the pump stage with the high speed electrical machine. Magnetic bearing technology is often adopted to achieve the operative speed and to satisfy the oil-free requirement of some applications [40].

1.3 High Speed Technology

The $\Gamma_1 = \omega_m \cdot \sqrt{P_m}$ factor has been proposed in [12] as a figure of merit for high speed machines, summarising the main challenges in achieving the power-speed node considered, including mechanical stresses, rotor-dynamic, and thermal management issues. In Figure 1.1 the corresponding lines to certain Γ_1 levels are presented. In [5], different machine topologies are classified with respect to the maximum value of $rpm\sqrt{kW}$ that can be achieved. The $\Gamma_2 = \omega_m \cdot P_m$ index has been introduced in [9] with the aim to classify high speed machines and defines trends concluding that for $\omega_m <$ 10-20 $[krpm]$, the Γ_2 factor is almost independent with respect to ω_m. In the range of higher rotational speed, Γ_2 is defined as a function of v_m^3/ω_m^2. The reason is found in the thermal limitation imposed. The reduction of the machine size lead to a limited surface that can be used to dissipate the generated losses that are strongly dependent on the rotational speed. The mechanical aspects alone are not representative of the overall challenges in high speed machines. High speed electrical machines result from a complex multi-physics system, where the interaction of the phenomena from different disciplines affect each other.

The multi-physics approach at the design stage is nowadays necessary in order to achieve high performance and exploit all the benefits of increasing the rotational speed. Furthermore, the co-design of power electronics and control strategies with the electrical machine is becoming an important aspect to maximise the system efficiency [4,41]. Qualitative analysis [10] has shown that the loss management drastically impacts the performance of high speed drives.

The combination of the above considerations lead to the identification of limits and trends for high speed technologies. Different authors have proposed curves to define the limits of existing high speed technologies. [10] and [42] presented formulations based on a combination of qualitative considerations on high speed machines and defined Γ_{BS} and Γ_M as the limit and trend for the technology, respectively. According to the data presented in Figure 1.1, the technology trends and challenge limit can be expressed in a general form by introducing the *challenge factor* Γ_c. The technological limits can be defined for each machine topology. It is proposed in a mathematical form as in (1.1)

$$\Gamma_c = \frac{\Gamma_{c,0}}{\sum_{h=1}^{\tilde{n}} \left[1 + (f_h \, \omega_m)^{\gamma_h} \right]} \tag{1.1}$$

where $\Gamma_{c,0}$ is the max power gain, $\tilde{n}$ is the maximum number of critical nodes required, f_h is the challenge level cut-off speed while γ_h is the speed-power trend coefficient, which defines the challenge level slope.

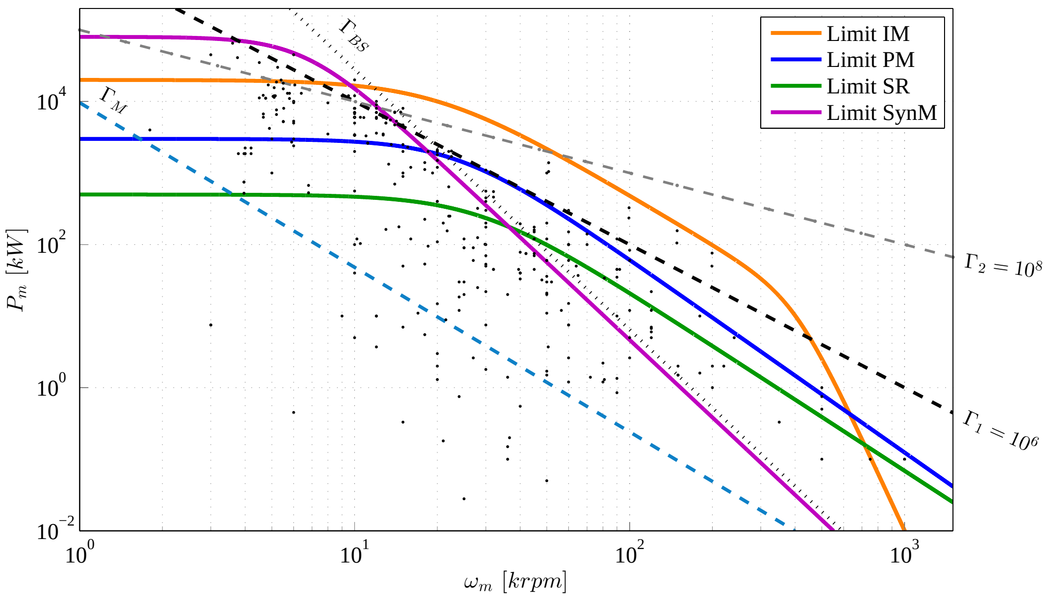

Figure 1.3: Power against speed nodes: technology limits for different machine topologies used in high speed applications.

In Figure 1.3 the limits defined according to (1.1) are presented from the data in Figure 1.1. The limits Γ_{BS}, Γ_M, $\Gamma_1 = 1\,[Mrpm\sqrt{kW}]$ and $\Gamma_2 = 100\,[Mrpm\,kW]$ are proposed as matter of comparison. According to the limits defined, the overall power-speed range can be divided into three main parts: the high power-low speed range, the medium power-medium speed range and the low power-high speed range. The chart presented highlights the actual limitations of high speed technology. The thermal challenges in the high power range become important and impose a strong limitation to the maximum power that can be achieved in electrical machines featuring high rotational speeds, because the extraction of the losses in the rotating part is a technological challenge. On the other hand, the mechanical aspects and rotor dynamics are an important factor in the limits that can be found in the high rotational speed range. The material of the rotating parts are pushed to their mechanical limits, which imposes a boundary on the rotor diameter and peripheral speed that can be achieved. A good balance between the above mentioned aspects can be found in the medium power-medium speed range where a compromise between the thermal and mechanical factors in combination with a good electromagnetic design challenges the state of the art machines.

According to the above, the peripheral speed for high speed machines is considered indicator of the rotor structure challenge. In Figure 1.4 the power against peripheral speed for the machines presented in Figure 1.1 are shown. The considered machine topologies clearly present a different peripheral speed limit mainly related with the rotor structure as reported in [5]. Induction machines, in particular solid rotor induction machines (SRIM) take advantage of the mechanically robust rotor to achieve the top tip-speed amongst all the other machines.

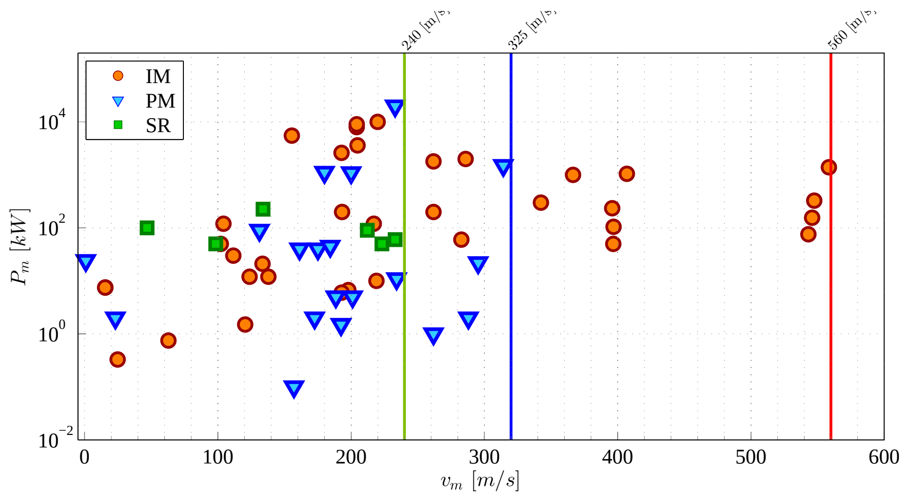

Figure 1.4: Power (P_m) against peripheral speed (v_m) from literature. The vertical lines highlight the maximum peripheral achieved by means of the different high speed machine topologies.

1.4 High Speed Induction Machines

Among the different electrical machines topologies that are used for high speed applications, induction machines (IMs) are widely adopted for various power-speed operative nodes. Different technological solutions have been found in order to enable higher rotational speeds for higher power levels. Induction machines are among the most suitable topology for high speed applications thanks to their robustness and capabilities to operate in harsh environments. All the benefits that arise from increasing the rotor speed comes along with challenges. The current limits of the high speed technologies are related with a conjunction of engineering aspects that arise from the combination of the electromagnetic performance, the thermal management, the rotor-dynamic aspects, and the mechanical stresses in the components of the machine. Various rotor structures for IMs can be found in literature as the current state of the art solution chosen for certain power-speed levels and related with specific high speed applications. Figure 1.5 presents the IMs that industry and academia have produced and prototyped according to the data presented in Figure 1.1.

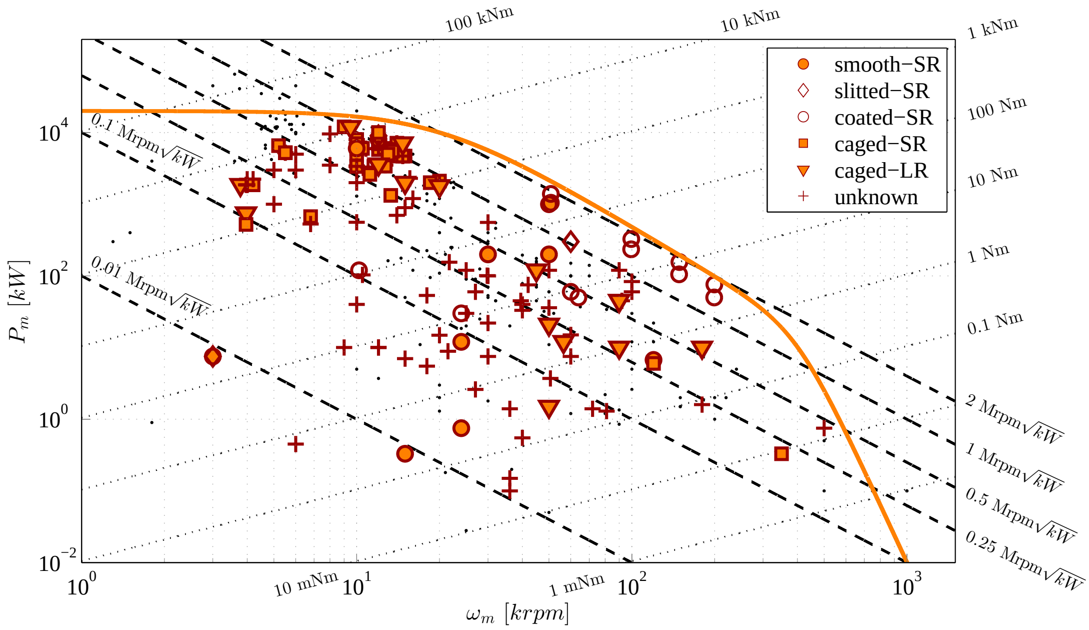

Figure 1.5: Power (P_m) against speed (ω_m) nodes: Induction Machines technology. The different markers highlight the different topologies of IMs used.

Different rotor topologies are distinguished by means of different markers to highlight the trends and technologies selected. Laminated rotor induction machines (LR) are the most common topology utilised and produced at present for a wide variety of applications and power-speed ranges. Their reliability and low cost make them suitable for specialised applications as well as for more conventional ones.

The rotor structure of a conventional induction machines consist of a high conductivity cage placed in dedicated slots machined in the rotor core as proposed in the sketch of Figure 1.6. The shape of the rotor bars is often optimised to fit the specifications of certain application requirements [43]. Laminated caged IMs configurations present limitations at high rotational speeds due to the tendency of the rotor bar to overstress the laminations slot opening (Figure 1.6-a). Alternative rotor structures and rotor bar shapes have been proposed to improve the electromagnetic performances and to withstand higher mechanical stresses [30].

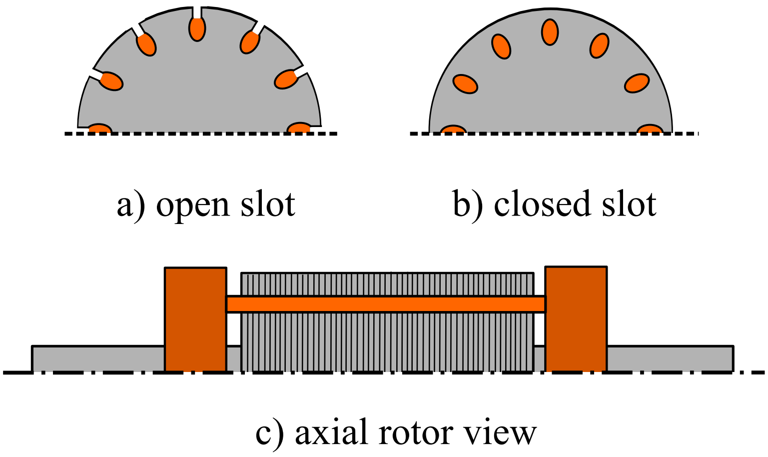

Figure 1.6: Laminated Rotor Induction Machines.

Closed rotor bar slot designs (Figure 1.6-b) resulted as an effective solution to enhance the achievable rotational speed [44,45]. Moreover, caged rotor structures are equipped with a high conductivity end ring (Figure 1.6-c) in order to minimise the path closure of the rotor current. The component design and assembly requires detailed investigation for rotors rated at high operational speeds. The mechanical stresses, the stiffness of the rotor, and the operational temperature of the material are important factors to account for. In [46], the detailed design of the end-ring designed for high speed traction applications is presented, where the multi-physics approach has been implemented to achieve a reliable and effective solution.

Solid rotor induction machine topologies were first studied in the 1920s [43]. The low production cost, simple manufacturing, and the robust structure have been the main attractive characteristics and have pushed researchers and industries to consider this topology as a viable alternative to the laminated rotor for harsh environment applications as well as for high speed. However, the simple and robust structure comes with lower efficiency and lower power factor compared to cage rotor IMs. The smooth solid rotor topology (Figure 1.7-a) is the most simple, cheap, and robust among all the different alternatives that can be found in literature. The rotor material is used as the media for both the magnetic and electrical fields. The rotor eddy current induced tends to circulate in the outer part of the rotor due to the skin effect at the rated frequency, thus leading to field shielding effects, which generate a considerable amount of surface loss. The magnetic field penetration in the rotor is a critical parameter that affects the machine performance.

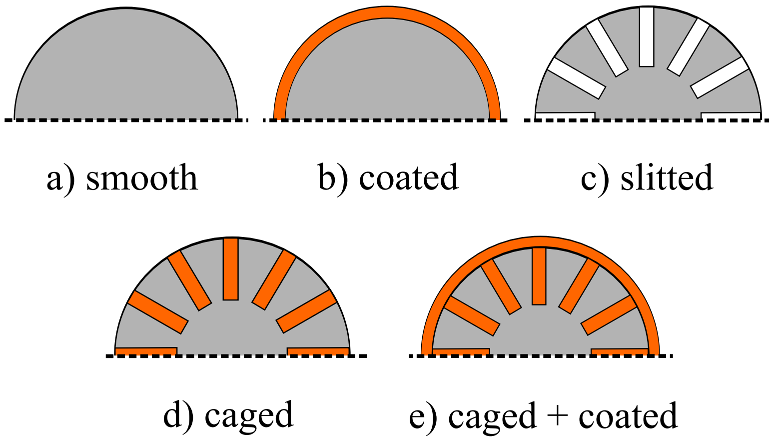

Figure 1.7: Solid Rotor Induction Machines. Cross section of different rotor topologies.

In smooth solid rotor topologies, the relatively low electrical conductivity and the magnetic properties of the iron core results in a low power factor and a reduced rated efficiency. The air gap magnetic field space harmonics strongly affect the rotor losses in smooth solid rotors as they generate high frequency harmonic losses on the rotor surface. However, despite the space harmonic effect, the characteristic of IM equipped with a solid ferromagnetic rotor can be improved by selecting proper solid rotor material, using composite (coated) structures, applying slits/grooves [47, 48] to create a preferred path for the electric and magnetic fields and applying additional cage winding [43]. High conductivity materials have been adopted as rotor coatings (Figure 1.7-b) to concentrate the electrical fields and currents in the thin coating layer thus enabling the magnetic field to penetrate the rotor core while screening the flux density high harmonic components. The mechanical adhesion of the coating and the manufacturing complexity of such structures pushed towards alternative solutions to enhance the performances of SRIMs. Slitted rotor structures

(Figure 1.7-c) have been proposed as an alternative to the coated rotor solution to enhance the magnetic field penetration in the rotor whilst reducing the surface losses due to the induced eddy currents. The higher friction losses and the reduced robustness of the rotor structure limits the application of this topology for high rotational speeds. Hybrid solutions propose the combination of the above presented alternatives, by introducing rotor bars in the solid core (open or closed slot) (Figure 1.7-d). Furthermore, more complicated structures have been investigated including anisotropic rotor structures [49], skewed-slit, spiral copper coated and shell-composite structure [50].

Moreover, the intrinsic three-dimensional field distribution in SRIM requires the investigation of the phenomena in the rotor end region. In high speed applications, the rotors axial structure has a big impact in the rotor-dynamic behaviour, in the rotor robustness and both the electromagnetic and mechanical losses distribution.

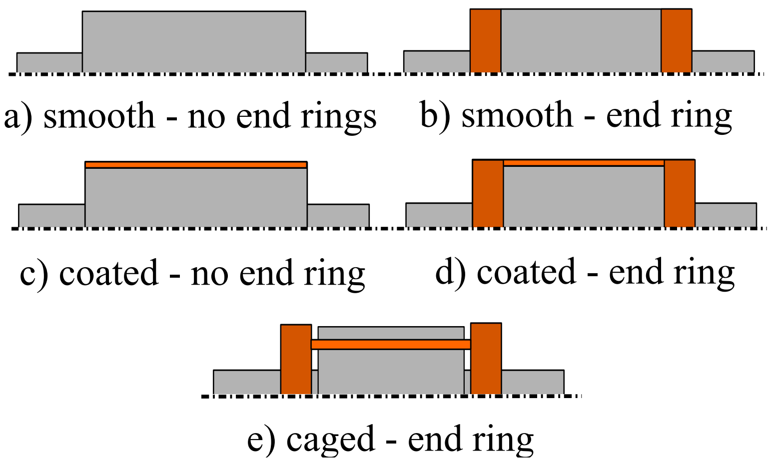

Figure 1.8: Solid Rotor Induction Machines. Axial cross section of different end region arrangements.

The field distribution in solid rotor topologies require an over-length rotating element to ensure that the closure path for the induced current in the rotor does not reduce the active length of the machine. Figure 1.8 presents some of the solutions for SRIM. High conductivity end-rings (Figure 1.8-b, Figure 1.8-d and Figure 1.8-e) reduces the axial length of the rotor structure while also reducing the robustness and increasing the complexity of the structure with respect to the simple over-length solution (Figure 1.8-a and Figure 1.8-c). The manufacturing and assembly of end rings for high speed applications could prove a difficult task as the material adhesion and the thermal aspects need to be accounted for. The performances of SRIM are mainly affected by the electromagnetic design according to the selected materials.

1.4.1 Electromagnetic analysis of SRIM

The design of SRIMs requires the calculation of the electromagnetic field within the solid ferromagnetic rotor. The calculation techniques employed for laminated caged IMs have been found ineffective for assessing the performance of SRIMs as the rotor equivalent impedance is highly dependent on the saturation level of the material, the skin effect on the conductive components, the space harmonic of the air-gap field, and the operative slip of the machine. In the last century, researchers and engineers have developed alternative analytical and computational models, taking advantage of the increased computational power available thanks to finite element analysis (FEA) software. The intrinsic three-dimensional field distribution within the rotor core suggests using a three-dimensional FEA. Despite the accuracy, the computational effort required has lead towards bi-dimensional analysis methods that result in more suitable design and analysis. tools The introduction of equivalent electromagnetic rotor material properties enables bi-dimensional analysis and accounts for the losses and magnetic field distribution occurring in the rotor end region. The non-linearities of the rotor materials are accounted for in FEA, which relies on the accuracy of such rotor material models implemented. Time-domain (TD) FEA is the most accurate technique adopted for performance prediction of SRIM [51]. However, FEA-TD results in high computational effort required due to the large rotor electromagnetic time-constant. The steady-state condition for the electromagnetic field is necessary to achieve a reliable solution. Alternatively, time-harmonic (TH) solutions can be computed by means of FEA resulting in a drastic reduction of the computational time, however it requires an equivalent harmonic material model to be computed and implemented. The accuracy of the solution considering FEA-TH is dependent on the magnetic model of the ferromagnetic materials as well as on the stability of the solver and its capability of computing non-linear solutions. As the single-phase steady state equivalent circuit (EC) is among the most popular modelling technique for IMs, FEA are usually used to estimate and investigate the non-linear dependencies of the lumped parameter of ECs [52]. The no load test and locked rotor test are simulated in the FE environment by means of static simulations (FE-ST) and either FEA-TD or FEA-TH, respectively.

Furthermore, analytical models based on electromagnetic field theories can evaluate the magnetic flux density and current density distribution within the solid rotor core [53]. Modified equivalent circuits have been adopted and the parameters evaluated through power balance or electromagnetic field considerations [26]. Numerical techniques, focused on finite element [54] (FE) and finite difference (FD) methods have also been investigated in order to minimise the computational time required for the calculation of the field distribution [55], and to account for space harmonics effects. The Multi-Layer-Transfer-Matrix (MLTM) has been proposed [56, 57] as a numerical technique that results in a good compromise between the computational time and the detail of the description. However, the method requires the initialization of electromagnetic quantities which needs to be accurately estimated in order not to affect the final solution. Equivalent model of materials have been introduced to account for the three-dimensional field distribution as well as the material non-linearities.

1.5 The Multi-Physics Aspects

Given the considerations described in the previous sections, the detailed analysis of the phenomena that occur in high speed machines involves different disciplines and their interaction. It suggests that the design of high speed machines in general, and of SRIM in particular, requires the attention of engineers at the design stage for the thermal, mechanical and rotor-dynamic aspects in combination with the material properties. The characterisation of the electromagnetic, thermal and mechanical properties of high speed machines is a key aspect when it comes to enhancing the power density and rotational speed. The rotor electromagnetic field distribution and losses are affected by the electromagnetic material properties and the operational conditions. In order to assess the impact of the cooling technique on the performance of the machine, the heat extraction from the rotor and its dissipation requires detailed investigation. Furthermore, the integrity of the rotor structure is dependent on the operative conditions as well as on the temperature of the rotor materials. The above considerations are summarised in Figure 1.9 where the conceptual multi-physics loop is depicted. In the following sections an introduction to the main aspects that need to be accounted for in the different disciplines are presented.

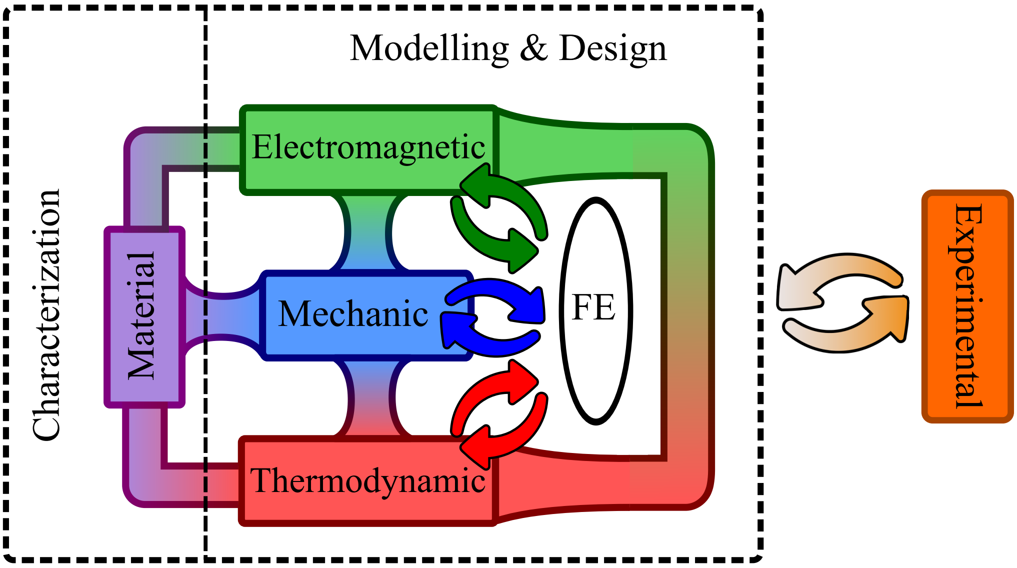

Figure 1.9: Multi-Physics Loop for high speed machine design

1.5.1 Mechanical Aspects

The mechanical challenge is gaining more importance due to pushing the peripheral speed of electrical machines towards the limits imposed by the current material characteristics. The peripheral speed of the rotor surface is identified as a limiting factor of the maximum allowed rotational speed [58]. In particular, the mechanical limits are imposed by the materials and the rotor structure [59]. The impact of the mechanical properties of the material can be determined by simply considering the solutions of the differential equations that govern the stress distribution in a rotating cylinder [59]. The radial and tangential strain components enable an approximation of the maximum stress in the rotor element of electrical machines. The peripheral speed is defined as the product of the shaft angular speed $\omega_m\,[^{rad}/_{s}]$ and the rotor external radius $r_R\,[m]$ (1.2).

$$v_m = \omega_m\, r_R \tag{1.2}$$

Considering a parametric material featuring an arbitrary tensile strength $\sigma_T\,[MPa]$, the maximum achievable peripheral speed can be expressed according to (1.3) defining $\delta\,[^{kg}/_{m^3}]$ as the mass density and $\nu\,[pu]$ as the Poisson ratio.

$$v_{Max} = \sqrt{\frac{\sigma_t}{\delta}\,F(\nu)} \tag{1.3}$$

The factor $F(\nu)$ is dependent on the rotor structure and its formulation can be found in [59].

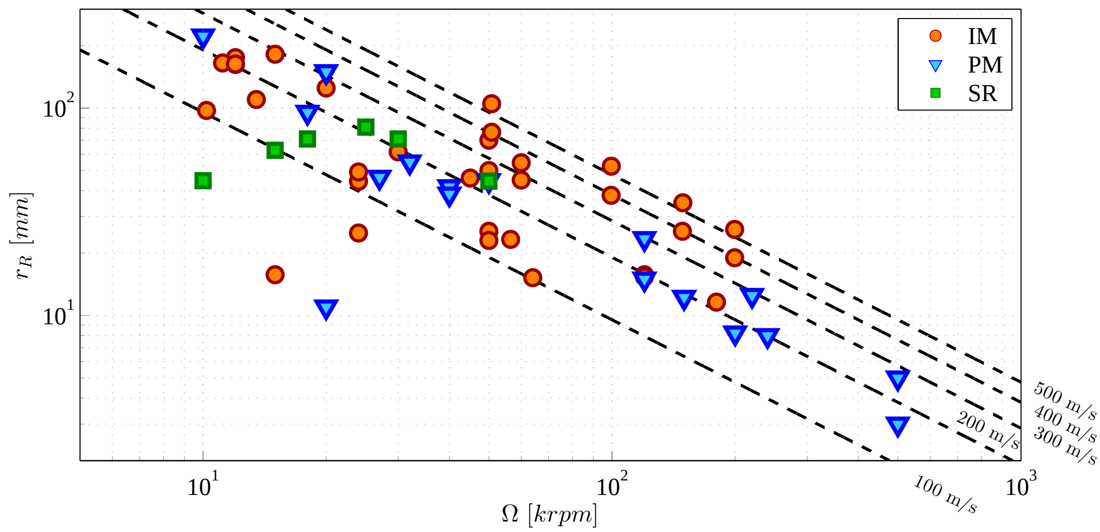

Figure 1.10: Rotor radius (r_R) against the angular speed (ω_m). The rotor radius related with a given maximum peripheral speed is highlighted with the dashed line.

High speed machines are developed considering different topologies and therefore different rotor structures. In Figure 1.10, the selected rotor radius against angular speed for the machine found in literature are presented, highlighting the peripheral speed achieved by means of the different rotor topologies. The design aspects concerning the retraining sleeve [60, 61] and copper coating sleeve [62] in PMSMs has gained lot of interest as the technological element which enables the reduction in the rotor losses and increases the rotating speed of the machines without compromising the integrity. The design of the multi-layer structure and copper coated rotor for high speed SRIMs requires detailed mechanical analysis in order to account for the mechanical integrity of the structure operating at high peripheral speeds. The stresses on the rotor element combined with the thermal effect due to the losses are critical aspects to be accounted for at the design stage. Furthermore, the mechanical design of the end-ring for IMs is of equal interest as it results in a critical component for high speed applications [63]. The soldering-braising of the end-ring with the rotor bars or the coating structure becomes critical for the machine integrity and relevant for the performances of the machine [33]. Moreover, the mechanical aspects and limitations impact on the output power. In literature, many sizing equations for electrical machines relating the output power with the geometry, material property, operative conditions and performances of the device can be found [64, 65]. The torque required for a fixed power level is inversely proportional to the rotational speed ($T_{em} \propto 1/\omega_m$) and dependent on both rotor radius and active length of the machine. As the output power is proportional to the rotor volume, the rotor diameter limitations imposed by the mechanical aspects impact on the performance and capabilities of the machine.

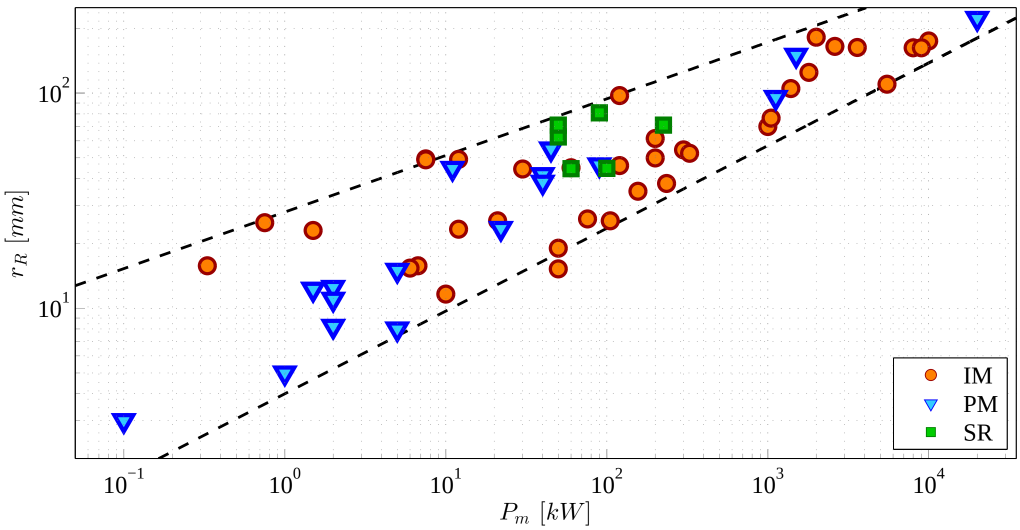

Figure 1.11: Rotor radius (r_R) against the power level (P_m). The rotor radius selected lays between the dashed lines that highlight the boundaries.

The rotor radius selected for the high speed machine in the review section are presented in Figure 1.11. The induction machine takes advantage of the rotor robustness in the low power range (high speed) where bigger rotor radii are selected with respect to one of the PMSM topologies. Furthermore, the rotor volume is defined at the design stage in relation to the rotor losses while the capabilities of loss extraction are strictly related with the cooling techniques selected.

1.5.2 Rotor-Dynamic Aspects

The rotor diameter affects the electromagnetic and thermal conditions of the SRIM. The axial length is another critical parameter which plays an important role in the above mentioned disciplines as well as affecting the rotor-dynamic aspect. The rotor diameter and length in combination with the rotational speed affects the rotor-dynamic performances of electrical machines in terms of the vibration level, mechanical stability, reliability and noise level [66]. The tendency towards high speed machines and integrated drives is enhancing the importance of good rotor-dynamic analysis and monitoring to achieve reliable operative conditions. The critical speed of the drive-shaft can be defined as the angular speed that excites the natural frequency of a rotating component causing a drastic increase in the system vibrations. The natural frequency of the rotor is strongly dependent on the stiffness of the shaft and its supports, the total mass and the geometry of drive-shaft, the unbalance of the mass with respect to the axis of rotation and the damping capabilities of the system. The rotor structure should be accurately designed in order to avoid dangerous vibration levels and operation in proximity of the critical speeds [22]. Megawatt generators and pipeline compressors feature articulated drive-trains that are required to cope with the high rotational speed and the external excitation forces on the shaft generated by the turbine/compressor and the generator [22, 67, 68]. Spindle machines are required to withstand axial load at high rotational speed [69]. The application and the mounting conditions in which the machines are required to operate impose additional excitation component such as inertial, radial and axial forces arising from gyroscopic effect or external disturbances. The reduction of the radial force component generated in electrical machines due to the interaction of the high frequency component of the air-gap magnetic flux density is necessary to avoid over-stress on the support element. Furthermore, the balancing of rotor for high speed operation requires fine tolerances and good accuracy in order to avoid forced responses that could damage the machine [70, 71].

Simplified formulations can be found to roughly evaluate the natural frequency of shafts [15, 72]. Considering the axial length of the shaft between the bearing location as $\ell_b = \alpha\,\ell_A$ (ℓ_A is the active length of the machine), the critical frequencies can be predicted according to the geometry and mechanical properties of the rotor and the stiffness of the supports [72, 73]. Simple formulations can be found for homogeneous rigid rotor. Complex rotor structure as well as flexible rotor one requires more accurate calculations to predict the critical frequency and the vibrations for certain operative conditions. Based on the state model of the rotor structure, the *Campbell diagram* enables to identify the critical frequencies of rotors. The advantage of self-centring operation comes along with the problem of the high vibrations arising while crossing the critical frequency [72]. The core axial length has direct consequences on the rotor-dynamics of high speed machines as well as on the efficiency of IM. Another element which impacts the natural frequency of the drive shaft is the bearing technology implemented, in terms of their stiffness and damping effect as discussed in the following section.

1.5.3 Bearing Technology

The mechanical issues arising from the stresses on the rotating component have to be combined at first instance with the rotor-dynamics of the drive shaft. The prediction of critical speed and vibrations enables designs of the rotor structure and its rotating support (bearing) to safely operate the machine at high rotational speed. The application requirements as well as the above mentioned considerations are the main factors in the bearing choice for high speed applications. In Figure 1.12 the bearing technologies applied to the different power-speed nodes presented in Figure 1.1 are depicted.

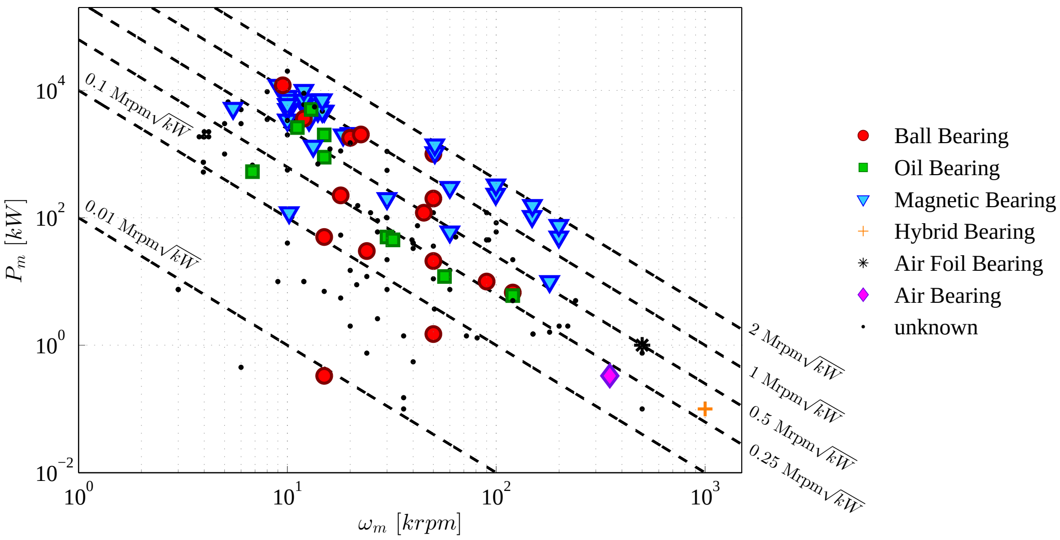

Figure 1.12: Power(P_m) against speed (ω_m) nodes: bearing technology review.

The rotor supports for high speed machines needs to be selected to withstand the mechanical stresses arising from the rotational speed and comply with the low loss, high reliability requirement of most applications. Moreover, the bearings are required to withstand the torque load, provide the necessary damping and stiffness to achieve good rotor-dynamic performance at high speed. In Table 1.1 the bearing technologies adopted for high speed applications are collected and quantitatively compared according to manufacturer data and from [7, 74].

Table 1.1: Bearing technology summary.

Material	BB	OB	MB	AB	HB
ND $[mm/min]$	$1e6$	$2.5e6$	$4.5e6$	$4e6$	$4e6$
Max Speed $[m/s]$	160	105	200	225	225
Max Temperature $[°C]$	230	90	540	650+	/
Min Temperature $[°C]$	-30	30	-180	-180	/
Damping	$--$	$-$	$+/-$	$++$	$+$
Misalignment Tolerance	$--$	$-$	$++$	$+/-$	$+$
Stiffness $[kN/\mu m]$	7	10	$-$	$-$	$-$
Friction	$--$	$-$	$++$	$+/-$	$+$
Weight	$-$	$--$	$+/-$	$+$	$-$
Stability	Passive	Passive	Active	Passive	Active
Fault Tolerance	None	None	Good	None	None

Ball bearing (BB) technology is widely used for most commercial products. However, the choice of bearing for high speed applications requires consideration concerning the limits of the materials, operative temperature and the specific application requirement to achieve high stiffness and low friction losses. Ball bearing, oil sleeve bearings (OB), and magnetic bearings (MB) are the most popular technologies for bearings in high speed machines [7, 15]. Air foil bearings [38], air bearings [75] (AB) and recently proposed hybrid bearings (HB) technologies [76] are gaining interest in the high speed range as depicted in Figure 1.12 for niche applications to overcome the limitations of other bearing technologies and achieve high system integration.

The mechanical and thermal properties of the rolling balls are the main limiting factor in ball bearing technologies. The maximum operative speed of bearing ω_{MAX} $[rpm]$ is an important factor in the bearing selection. However, the bearing lifetime is strongly dependant on the bearing peripheral speed, therefore proportional to the rotor shaft diameter. The "*speed factor*" ND is the parameter considered for bearing selection in high speed applications [69].

Magnetic bearing (MB) technology is often considered as a reliable, efficient and oil free solution for many applications alternatively to ball bearing [77]. The capability to operate in harsh environment ($-180\,[°C]$ to $540\,[°C]$ [7]) and the flexibility given by the active control of the system rotor-dynamic behaviour are characteristics which lead MB to be applied in high speed electrical machines and turbo-machinery applications. Passive (PMB) and Active (AMB) magnetic bearing are designed to achieve radial and/or axial control of the rotor shaft. The modulation of the magnetic field in the air-gap enables the system to generate the levitating forces which are directly proportional to r_R^2 according to the Maxwell Stress Tensor (MST). The magnetic field is required to penetrate the rotor structure and therefore magnetically permeable material needs to be adopted. The limitation arising from the mechanical stresses due to the rotational speed and the losses generated by the induced eddy current in the rotor have to be accounted at the design stage to achieve efficient design. AMBs can achieve ND values which are roughly twice the limiting factor of advanced contact bearing defined at $ND \approx 2 \cdot 10^6$ [78]. Furthermore, the MB technology requires auxiliary power electronics and advanced control techniques to achieve high performance as well as special features to enable fault tolerance operative conditions. Tuning procedures are required thus increasing the cost and limiting the mass production of this bearing topology. On the other hand, OB, AB and HB require auxiliary elements to guarantee the rated supply of cooling and lubricants necessary for the operation.

Hydrostatic (micro-nozzle bearing) and hydrodynamic (foil bearing) air bearing (AB) technologies use a thin film of pressurized air to support the rotating element avoiding any contact between the solid element of the machine. The force transmission is achieved through the pressurization of the air in the bearing area created by external means (hydrostatic air bearing) or by the bearing rotation itself (hydrodynamic air bearing). The oil free characteristic, combined with the wide operative temperature range of such technology, comes together with the drawback that usually a custom design is required. The low stiffness that can be achieved with such technology is limiting the application range to rotating speed $\omega_m < 100\,[krpm]$ [79].

1.5.4 Thermal Management

The high rotational speed allows a reduction in the rotor size for a given power. The high efficiency requirements imposed by the applications have a strong impact on the electromagnetic design and material selection to achieve minimum losses. However, despite minimised, losses still generate heat that must be extracted from the machine. The increased power-to-volume ratio achieved by increasing the rotational speed comes with the drawback of reducing the heat dissipation surface. More aggressive cooling techniques have to be put in place in order to maintain the material within their safe operative temperature range. On the other hand, the loss distribution within the machine structure is becoming an important aspect to account in order to maximise the effect of the cooling technique.

In Figure 1.13 the main cooling techniques applied to different power-speed nodes are proposed. In the MW range, the thermal management has a big impact on the limitations imposed to the achievable output. The extraction of the rotor losses has pushed investigation towards cooling techniques for the rotating element e.g. flooded design [43], liquid cooling system [80–82] or targeting design with minimum rotor losses. The physical distance between the heat source and the cooling media is the main challenge in the heat dissipation through the stator outer bore [43]. Cooling channels in the stator structure [83], high thermal conductivity paths inbuilt in the winding structure as well as flooded cooling arrangements [84] have been proposed to overcome the above mentioned problem. Different cooling techniques have been proposed, implemented and are currently state of the art for high speed applications.

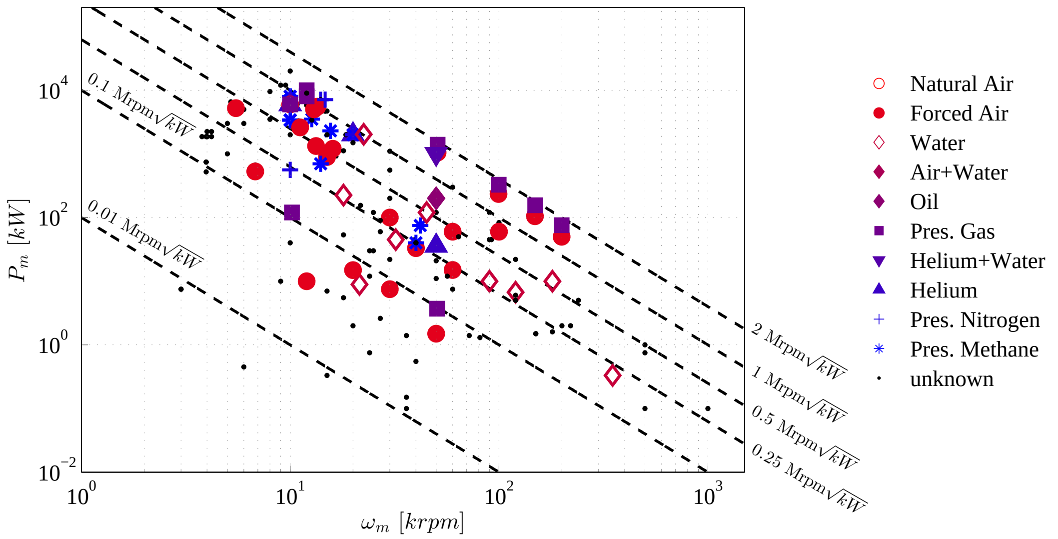

Figure 1.13: Power(P_m) against speed (ω_m) nodes: thermal management review.

The efficiency η is a *per-unit* value that defines the losses that take place in the power conversion process of a system. The location of the losses, with respect to the system and the environmental conditions, is an important factor when it comes to their management and extraction. Qualitative analyses have been proposed [9, 10, 85] to assess the impact of high rotational speed on the losses in electrical machines. The operative temperature of the machine is the result of the balance between the heat generated and the heat removed (neglecting the thermal capacity). The losses in electrical machines can be divided according to the heat source location and type. The computation of the losses, their impact on the material properties and the efficiency of the heat extraction techniques adopted is a challenging task which requires expertise in computational fluid dynamics (CFD), thermodynamics and electromagnetism. The coupling among the disciplines has gained a lot of interest aiming to improve efficiency and push the boundaries in high speed applications [43, 86].

The prediction of the temperature distribution within electrical machines is achieved adopting equivalent thermal circuit models [87], lumped parameters network [88, 89], finite difference or finite element analysis (CFD). To achieve good accuracy, the geometry and the properties of the material adopted need to be accurately modelled as well as their dependency with respect the thermal and electromagnetic operative condition of the machine. The main challenge in loss management for electrical machines is the heat extraction from the rotor structure and the heat dissipation through the heat exchange surfaces which are strongly dependant on the heat transfer coefficient that characterises the overall structure. Analytical formulations and CFD analysis, supported by experimental validations, provide tools that enable the prediction of the impact of different cooling techniques.

In high speed SRIM, the rotor losses are a critical aspect to be accounted for. The minimization of the losses has been investigated by optimising the rotor copper coating thickness [90] or by reducing the air gap harmonic components by means of semi-magnetic wedges on the stator slot openings [57]. The thermal dissipation of the rotor losses depends on the convection thermal resistance of the air gap that requires the evaluation of the heat transfer coefficient h_g. The estimation of the air-gap heat convection coefficient has been the subject of many studies [91, 92] and empirical formulae have been experimentally validated providing effective tools to predict the thermal management capabilities. In Figure 1.14, the dependency of the air gap convection heat transfer coefficient against the rotor speed and the air gap thickness ε_g is presented according to [91]. The selection of the physical clearance between rotor and stator is an important aspect as impacts not only on the cooling efficiency as highlighted in Figure 1.14, but also on the electromagnetic performances as well as on the mechanical losses generated by means of the fluid flow generated by the rotating element. Analytical formulation can be found in literature [65, 85] to select the air gap thickness with respect to the output power and main rotor dimension.

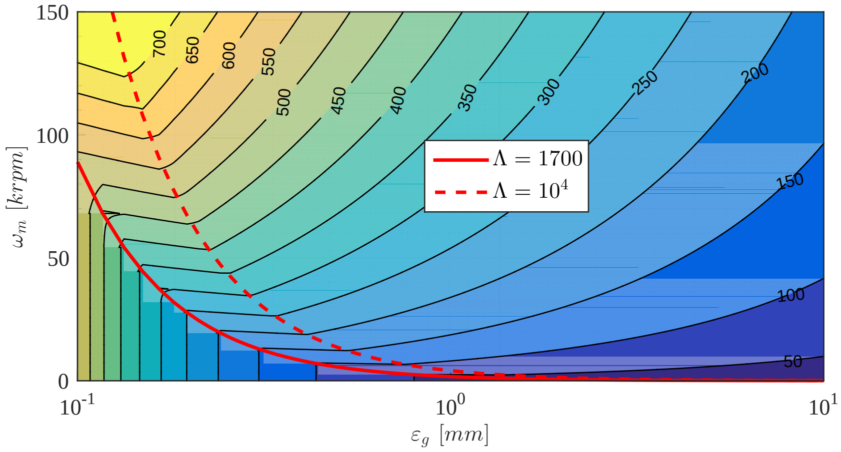

Figure 1.14: Contour of air gap convection heat transfer coefficient ($h_g\,[W/(m\,K)]$) against air gap thickness ($\varepsilon_g\,[mm]$) and rotor speed ($\omega_m\,[krpm]$). The calculations are performed considering a rotor radius of $r_R = 45\,[mm]$, kinematic viscosity of $\mu = 2.1e{-}5\,[m^2/sec]$ and thermal conductivity of $k = 0.025\,[W/(m\,K)]$

1.6 Materials for High Speed Applications

The push towards high performance drives, higher efficiency and targeting higher rotational speed is challenging material engineers. The properties and performances of the materials currently used are required to achieve accurate models and performing devices. That results in a challenging task when it comes to detail and to model the losses in materials excited by means of the time varying field, and to also account for the variation in their properties with respect to their mechanical and thermal operative conditions.

High performance laminations are currently available and they enable a drastic reduction in the eddy current losses in electrical steel resulting in higher efficiency machines. Innovation in the manufacturing process of electrical steel, variations in the silicon content of *SiFe* laminations and the thickness reduction are just examples of the material trend among the currently available in the market. Amorphous material and soft ferromagnetic powder cores are rapidly gaining interest for high speed application as they feature significantly reduced mass density and low losses at high frequency while featuring an increasing saturation flux density level within the last years. Furthermore, the conductive elements of the machine are important and should be carefully selected in order to obtain efficient and robust rotor structures. Copper alloys (*CuCrZi* and *CuBrZi*) became commercially available for the manufacture of end rings and rotor bars that are capable of withstanding the high stresses in the rotor at high speed. In Figure 1.15 a review on the best performing high conductivity materials are presented, highlighting the trends achieved considering various doping elements (e.g. *Si*, *Cr*, *Ni*, *Zn*) in different quantities. The electrical conductivity is presented in per unit with respect to the one of the pure copper ($\% IACS = 100$).

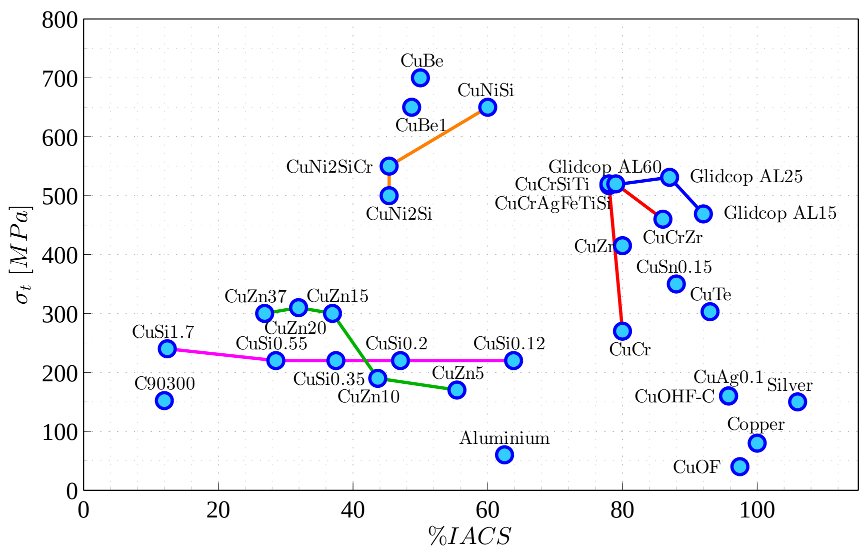

Figure 1.15: Conductive material literature review: tensile strength (σ_t) against electrical resistivity related to copper ($\% IACS$).

High tensile strength laminations have been developed, providing an advanced material that has found application in the rotor construction of high speed electrical machines [5, 93]. However, solid materials for SRIM and the performances of such topologies are very sensible to the mechanical and electromagnetic material characteristics. The characterisation of the magnetisation curve of solid materials as well as their electrical conductivity is required to achieve accurate prediction of the machines performance at the design stage [5, 93].

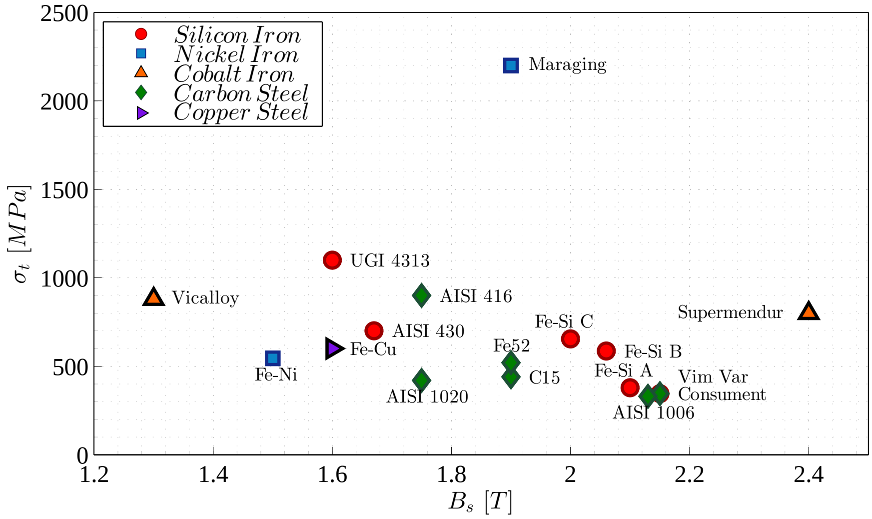

Figure 1.16: Solid material literature review: tensile strength (σ_t) against saturation flux density (B_s).

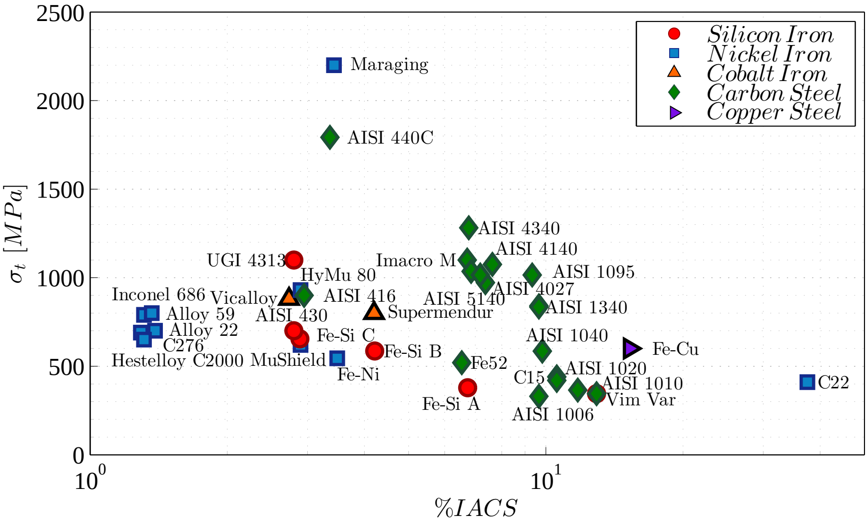

Figure 1.17: Solid material literature review: tensile strength (σ_t) against electrical resistivity related to copper ($\%IACS$).

Materials for solid rotor applications are selected based on a trade off of magnetic permeability, electric resistivity and high mechanical performances [1, 43]. The frequency of the time-varying field in the rotor structure is related to the fundamental frequency by the slip. The material characterisation of their magnetic properties as well as losses requires low frequency excitation and various models have been developed which enable material loss prediction [94].

In Figure 1.16 and Figure 1.17, the solid material commonly used for SRIM are presented and their mechanical characteristic are presented against the magnetic (saturation flux density) and electrical (electrical conductivity) characteristics, respectively. High carbon content materials feature mechanical characteristics that enable high peripheral speed.

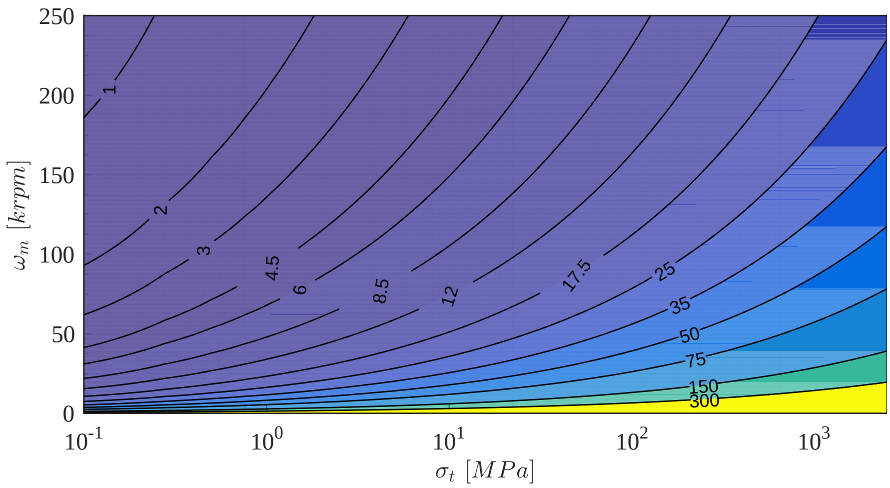

Figure 1.18: Rotor radius (r_R) contour plot against rotor material tensile strength (σ_t) and angular speed (ω_m). The calculations are performed for $\delta_r = 8000\,[{kg}/{m^3}]$ and $\nu = 0.3$ with a safety factor $\kappa_\sigma = 2$.

According to (1.3) in combination with the peripheral speed definition, the maximum rotor radius for a given structure can be calculated. A safety factor is introduced to guarantee a margin for errors in the calculations. The contour plot presented in Figure 1.18 presents the trend of the maximum rotor radius for different rotor angular speed and material tensile strength. The case of a smooth rotating cylinder is considered in (1.3) as representative of the smooth solid rotor structure and enables to achieve the rotational speed that are prohibitive the other rotor topologies. However, the poor electromagnetic properties of carbon based materials result in low efficiency machines at high rotational speed. The metal industry is becoming aware of the increasing demands of high performance solid materials, and novel materials are being developed in order to achieve enhanced mechanical and electromagnetic performances.

1.7 Thesis Outline

The calculations of the performances of solid rotor induction machines is presented in the following part of the document.

The performance of SRIM is strongly affected by the electromagnetic field distribution in the rotor structure. In *Chapter* 2, the solution of the *Maxwell's* equations in the rotor domain is presented. The discrete domain method (DDM) is proposed as an analytical model developed to account high space harmonic and non homogeneous rotor structures, enabling to compute the performance of multi-layer structure and copper coated solid rotor.

P.1 [95] L. Papini and C. Gerada, "Analytical-Numerical Modelling of Solid Rotor Induction Machine," *ELECTRIMACS 2014*, 19th-22ndMay 2014, Valencia, Spain.

The importance of the multi-physics approach in the analysis and design of high speed machines highlighted in the literature review (*Chapter* 1) is further considered and discussed in *Chapter* 3. The multi-physics design aspects are presented and the thermal, mechanical and rotor-dynamic models are separately described. Furthermore, the flexibility and capabilities of the proposed modelling techniques are applied to assess the impact of the thermal management and temperature distribution prediction on the performances of SRIM.

P.2 [96] L. Papini and C. Gerada, "Thermal-electromagnetic analysis of solid rotor induction machine," *7th IET International Conference on Power Electronics, Machines and Drives (PEMD 2014)*, Manchester, 2014, pp. 1-6. doi: 10.1049/cp.2014.0462

P.3 [97] L. Papini, C. Gerada, D. Gerada and A. Mebarki, "High speed solid rotor induction machine: Analysis and performances," *2014 17th International Conference on Electrical Machines and Systems (ICEMS)*, Hangzhou, 2014, pp. 2759-2765. doi: 10.1109/ICEMS.2014.7013968

The parametrised material is introduced in *Chapter* 4 as a fictitious rotor material. The electromagnetic characteristics of the material has been fully parametrised and the impact of the saturation flux density B_s, relative magnetic permeability $\mu_{R,r}$ and electrical resistivity ρ_r on the equivalent circuit parameters of smooth solid rotor induction machine is discussed. The selection of suitable material for SRIM is detailed providing measurement of magnetisation curve for construction steel.

P.4 [98] L. Papini and C. Gerada, "Sensitivity analysis of magnetizing inductance in solid rotor induction machine," *2016 19th International Conference on Electrical Machines and Systems (ICEMS)*, Chiba, 2016, pp. 1-6.

P.5 [99] L. Papini and C. Gerada, "Sensitivity analysis of rotor parameters in solid rotor induction machine," *2017 International Electric Machines and Drives Conference (IEMDC)*, Miami, 2017.

Before summarising the main aspect discussed in the thesis and recaping the relevant results in the conclusion in *Chapter* 6, the performances of SRIM for a waste heat recovery (WHR) application are presented in *Chapter* 5. The FE three dimensional analysis is performed in order to validate the electromagnetic calculations of the previous chapters. Furthermore, the performances of SRIM are compared with an induction machine featuring a laminated caged rotor characterised by closed rotor slots. The details of the case study machine are presented below. The rotor dynamic aspects of the SRIM are discussed and compared with experimental measurements.

P.6 [30] L. Papini, D. Gerada and C. Gerada, "Development and testing aspects of high speed induction machines," *2016 19th International Conference on Electrical Machines and Systems (ICEMS)*, Chiba, 2016, pp. 1-6.

1.7.1 Case Study Induction Machine

A three-phase 120[kW]-25[$krpm$] induction machine for waste heat recovery (WHR) application is considered as a case study. The cross section of the machine is presented in Figure 1.19.

Table 1.2: Case Study Machine Data

Parameter	**Symbol**	**Value**
Pole Pair	p	1
Mechanical Power	P_m	120[kW]
Maximum Speed	$\omega_{m,M}$	32[$krpm$]
Rated Speed	ω_m	25[$krpm$]
Rated Torque	T_e	45.8[Nm]
Rated Voltage	V_s	400[V]
Power Density	$P_m/\mathcal{V}$	30[MW/m^3]
Peripheral speed	v_m	210[m/s]
Ambient Temperature	T	300[$°C$]

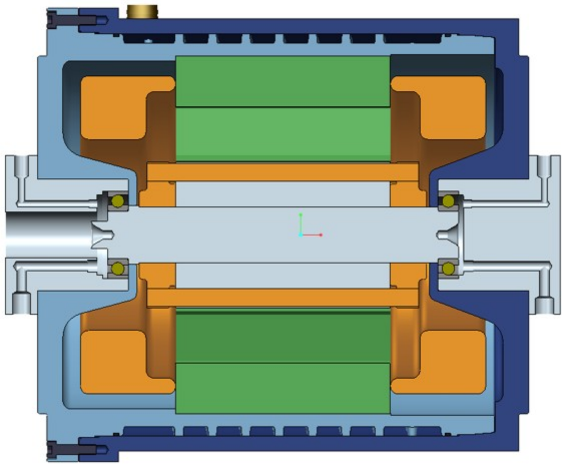

Figure 1.19: Cross section cut view of the case study caged rotor IM considered.

Closed slot rotor structure is selected in order to achieve the required mechanical robustness at high rotational speed [30]. The rotor bar shape is optimised in order to maximise the efficiency. The parameters of the IM are listed in Table 1.2. The caged rotor is replaced with a smooth solid rotor structure while the stator structure, comprehensive of the three-phase winding structure, remains unvaried. The analytical, thermal, mechanical and rotor dynamic modelling of the solid rotor induction machine (SRIM) are discussed in order to create a flexible tool that enables rapid performance computation. The performances of the caged rotor induction machine (CRIM) are compared with the SRIM designed for the same power-speed node.

CHAPTER

TWO

ELECTROMAGNETIC MODEL

The design and analysis of solid rotor induction machines requires the computation of the electromagnetic field distribution in the structure. The electromagnetic performances are strongly affected by the the magnetic field penetration, the induced eddy currents and, consequently, the power losses distribution in the rotor media. The effects of the intrinsic three-dimensional field distribution in solid rotor structure are not negligible.

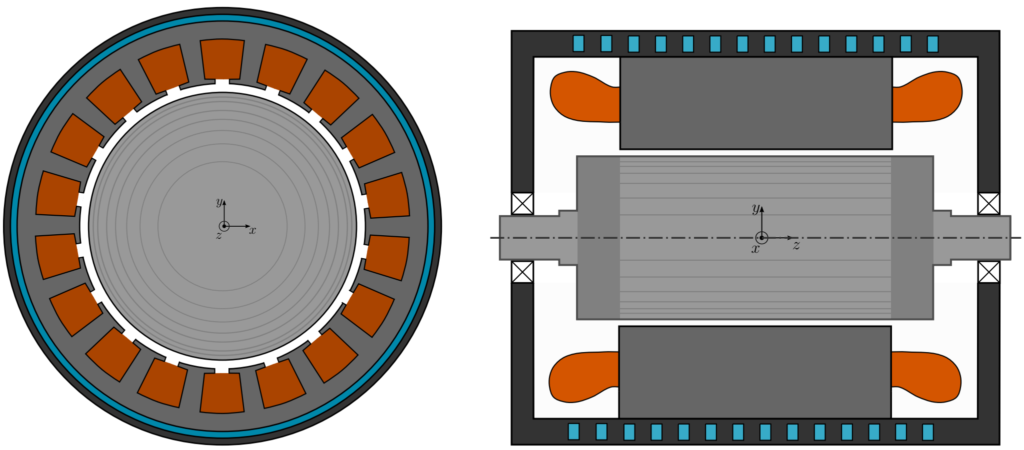

(a) $x - y$ cross section **(b)** $z - y$ cross section

Figure 2.1: SRIM schematic cross section representation

Bi-dimensional approximated model are widely adopted and correction factors have been introduced to account for the rotor end region effects. The computation of the field distribution is solid rotor induction machine with homogeneous and multi-layer structure is introduced and calculations are presented considering a SRIM which is schematically represented in Figure 2.1. The $x-y$ and $z-y$ cross sections are presented to highlight the main geometry modelled in the following section.

2.1 The Solid Rotor Induction Machine

The SRIM, as most electro-magneto-mechanic devices, consist of a group of (mechanically connected) solid rigid bodies in relative motion in an electromagnetic field. Both mechanical and electromagnetic models are required in order to achieve a full description of the device. The graphical representation of the general model considered is presented in Figure 2.2.

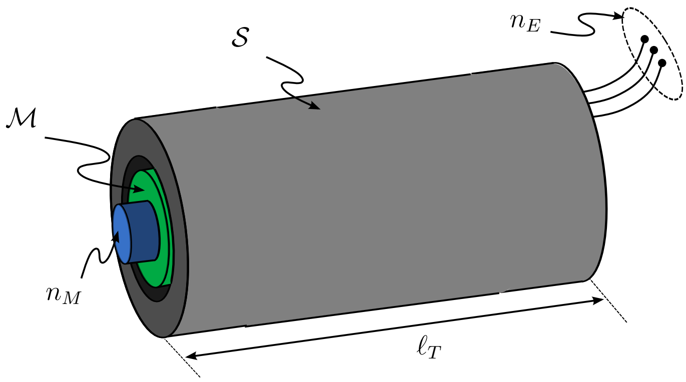

Figure 2.2: Idealised machine

Let's consider the physical space occupied by the device $\mathcal{D}$ as a finite subset of the euclidean measure space $\Sigma' \subset \mathbb{R}^3$ where the dot product is defined.

An inertial reference frame $\mathcal{C}_o = (O_o, {}^o\mathcal{E})$ is assigned by means of the orthonormal base ${}^o\mathcal{E} \in \mathbb{R}^3 : {}^o\mathcal{E} = [{}^o\tilde{\mathbf{e}}_1 \;\; {}^o\tilde{\mathbf{e}}_2 \;\; {}^o\tilde{\mathbf{e}}_3]$ defined as the space and it's O_o center of observation. Considering a coordinate system defined by means of the orthonormal base, the position of the generic point of the space $P \in \Sigma'$ for a time instant $t \in \mathbb{R}$ is described by means of the algebraic position vector ${}^o\bar{p}(t) : \mathbb{R} \mapsto \mathbb{R}^3$.

The rigid body approximation allows the deformation to be neglected and therefore the distance between two points of the same body is time-invariant in amplitude. Let's define the continuous function mass density $\varrho : \mathbb{R}^3 \mapsto \mathbb{R}^+$. The mass of a rigid body is defined as the integration of the volume of the mass density of all the material points which belong to it. The mechanical status and motion of rigid bodies is completely described by means of the law of motion of a representative material. An equivalent formulation is applied to the center of the mass of each body [100]. The solid bodies in which the device $\mathcal{D}$ consist of are classified with respect to their mechanical status and motion with respect to the inertial reference frame. The static body $\mathcal{S}$ consists of all the material points of the space that are defined by the time-invariant position vectors with respect to $\mathcal{C}_o$. Consequently, the set of the material points of the space that constitute the rigid body in relative motion with respect to the static parts are referred to as the moving body $\mathcal{M}$. The absolute complement of the static and rotating bodies in the space $\Sigma^{'}$ is defined as the fluid gap $\mathcal{G} = \Sigma^{'} \setminus (\mathcal{M} \cup \mathcal{S})$ and therefore $\mathcal{D} = \mathcal{S} \cup \mathcal{M} \cup \mathcal{G}$.

Considering an inner rotor-outer stator SRIM as in Figure 2.2, the static bodies consist of the magnetic stator core and the stator phase winding while the moving bodies are identified as the solid rotor element. The following analysis is based on SRIM structures which feature the characteristics listed below [101]:

(E.1) right cylindrical shape extruded rotor geometry;

(E.2) right hollow-cylindrical shape extruded stator core geometry;

(E.3) stator core and rotor axial extrusion length larger than the external transversal size;

(E.4) coaxial rotor and stator components physically separated by a hollow-cylindrical shape air gap region;

(E.5) constrained relative position between the static and rotating structure by means of bearings which apply reaction forces enabling the procession, nutation and linear motion to be neglected;

(E.6) cylindrical rotor structure featuring length ℓ_R, radius r_R, and consisting of an isotropic conductive soft ferromagnetic material;

(E.7) stator phase windings composed of a conductive material located in the stator core slots with a geometrically closed shape;

(E.8) hollow cylindrical stator core structure featuring length ℓ_S, inner radius r_S and outer radius r_T consisting of isotropic non conductive soft ferromagnetic material;

(E.9) stator magnetic core featuring straight slots parallel to the extrusion direction with small openings facing the main air gap.

These assumptions lead to interesting conclusions and enable a radical simplification of the model. Let's define $s \in \mathbb{N}$ as the number of bodies which the static solid rigid body amounts to. A local inertial reference frame $\mathcal{C}_s = (O_s, {}^s\mathcal{E})$ is assigned by means of the orthonormal base ${}^s\mathcal{E} \in \mathbb{R}^3$ and the center of the reference frame O_s, defined as the center of the mass of the static body. The *Galilean transformation* defines its motion with respect to $\mathcal{C}_o$ in order to account for inertial forces acting on the system, which are neglected here. Let's define $m \in \mathbb{N}$ as the number of bodies that the moving solid rigid body consists of. The number of the mechanical degrees of freedom $n_M \in \mathbb{N}$ of the device in the inertial reference frame $\mathcal{C}_o$ results as

$$n_M = \left[6\,s - \sum_{i=1}^{n_I}(6 - f_i)\right] + \left[6\,m - \sum_{j=1}^{n_J}(6 - f_j)\right] \tag{2.1}$$

where $n_I \in \mathbb{N}$ defines the number of inertial constraints applied to the static body $\mathcal{S}$ each featuring $f_i \in \mathbb{N} : f_i \leq 6\,\forall i \in [1, ..., n_I]$ degrees of freedom. Moreover, $n_J \in \mathbb{N}$ joints are defined as the constraints related with the mechanical contact between the bodies. Each joint features $f_j \in \mathbb{N} : f_j \leq 6\,\forall j \in [1, ..., n_J]$ degrees of freedom. The contribution of the static body and inertial constraint in (2.1) is neglected as the system is considered fixed to the inertial reference frame. Moreover, the hypothesis **[(E.5)]** depicts a scenario where $\sum_j(6 - f_j) = 5$ which, substituted in (2.1), results in a single degree of freedom $n_M = 1$ defined for the system. According to the previous considerations, Lagrangian mechanics [100] here is preferred as the description of the mechanical state and the motion of the rigid bodies by introducing the vector of the generalised positions $\bar{\chi}(t) : \mathbb{R} \mapsto \mathbb{R}^{n_M}$. The description of the motion of a rigid body requires the definition of a reference frame $\mathcal{C}_m(t) = (O_m(t), {}^m\mathcal{E}(t))$ fixed with the moving body and centred in the center of the mass of the moving body [100].

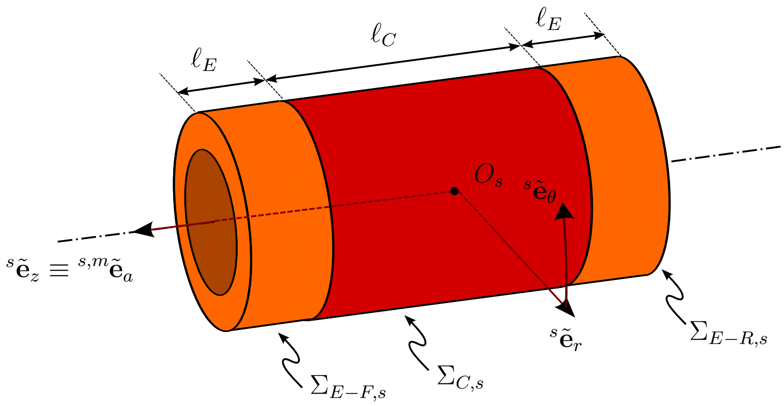

(a) Idealised static component

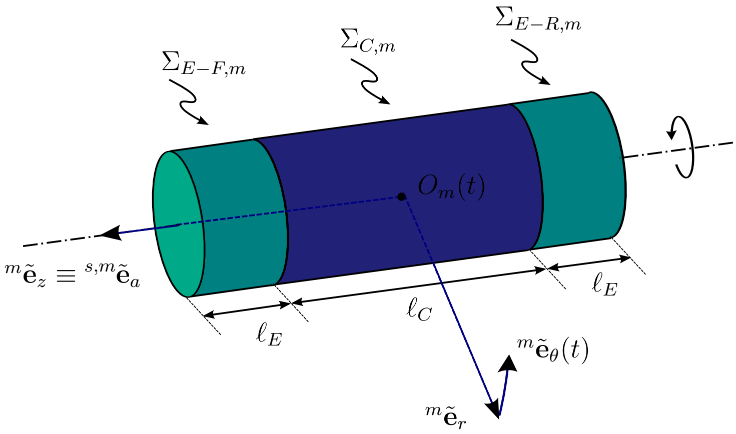

(b) Idealised moving component

Figure 2.3: Static and moving component idealised representation

In Figure 2.3a and Figure 2.3b a representation of the static and moving component is presented according to the assumptions introduced above. The cylindrical nature of the rigid bodies **[(E.1)]-[(E.2)]** implies that the axes of rotational symmetry, defined as ${}^{s}\tilde{\mathbf{e}}_s$ and ${}^{m}\tilde{\mathbf{e}}_s(t)$ for the static and the moving axes, respectively are coincident with their principal axes of rotation, ${}^{s}\tilde{\mathbf{e}}_z$ and ${}^{m}\tilde{\mathbf{e}}_z(t)$ [100]. The concentric nature of the moving and static bodies **[(E.4)]** in combination with the motion constraint **[(E.5)]** defines the alignment conditions and the alignment axis, ${}^{s,m}\tilde{\mathbf{e}}_a$ which is equivalent to the axis of rotation for the moving body.

The center of the mass of the static and moving bodies is defined coincident by means of the alignment condition and results in an identical center of all the reference frames defined, where $O_o \equiv O_s \equiv O_r$. The axes of rotational symmetry and the principal inertial axes for both static and moving elements and one direction of the inertial reference frame $\mathcal{C}_o$ are parallel to each other; they are also defined coincident with the alignment axis ${}^{m}\tilde{\mathbf{e}}_z \, (\equiv {}^{m}\tilde{\mathbf{e}}_s) \equiv {}^{s}\tilde{\mathbf{e}}_z \, (\equiv {}^{s}\tilde{\mathbf{e}}_s) \equiv {}^{o}\tilde{\mathbf{e}}_3 \equiv {}^{s,m}\tilde{\mathbf{e}}_a$. The center of the mass and the principal axis of rotation for the moving body is time-invariant according to the hypothesis **[(E.5)]**.

Having defined one direction for all the reference frames to be coincident, the couple of orthonormal vectors that complete their bases have to be selected. While the choice is arbitrary for what concerns the static reference frames, a preferable choice for $\mathcal{C}_r(t)$ is identified. According to the definition of the rigid body, in combination with *Euler's rotation theorem*, the reference frame is selected in order to achieve the description of the rotational motion by means of a single time varying coordinate in the reference frame. The orthonormal base is identified and a cylindrical coordinate system is defined. The unit vector corresponding to the same direction is considered, superimposed at the initial time instant ${}^{m}\tilde{\mathbf{e}}_r(t_0) \equiv {}^{s}\tilde{\mathbf{e}}_r \equiv {}^{o}\tilde{\mathbf{e}}_1$ and ${}^{m}\tilde{\mathbf{e}}_\theta(t_0) \equiv {}^{s}\tilde{\mathbf{e}}_\theta \equiv {}^{o}\tilde{\mathbf{e}}_2$.

According to the above assumption, the computational domain $\Sigma \subset \Sigma'$ is restricted to the finite subset of the space featuring a cylindrical shape, which encloses all the components of the device.

In SRIMs, as for many electrical machines, the structure of the front and rear part of the device, arbitrarily defined according to the reference system defined, look significantly different from the central region. Defining the length of the cylindrical computational domain Σ as ℓ_T as in Figure 2.2 and according to

the above considerations, the domain is divided in three different regions along the direction ${}^{s}\tilde{\mathbf{e}}_z$. The subset Σ_C of length ℓ_C is defined as the central region of the machine. The remaining part $\Sigma_E = \Sigma \setminus \Sigma_C$ of length $\ell_E = 1/2(\ell_T - \ell_C)$ is defined as the end region consisting of the rear Σ_{E-R} and front Σ_{E-F} domain, in symbols $\Sigma_E = \Sigma_{E-R} \cup \Sigma_{E-F}$.
Along with the axial division, the coaxial nature of the structures allows the division of the domain with respect to the radial direction. Since the cylindrical rotor structure is coaxial with the air gap and stator hollow-cylindrical regions, it is possible to identify a finite subset, which encloses the elements of each structure, Σ_r, Σ_g and Σ_s, respectively. The subsets extend for the entire axial length ℓ_T. The combination of the aforementioned division achieves a division of the device based on its structure as presented in Figure 2.3a and Figure 2.3b. The axial development of the stator's magnetic core is considered by defining a central region. Therefore, since $\ell_S = \ell_C$ the central region is expressed as $\Sigma_C = \Sigma_{C,r} \cup \Sigma_{C,g} \cup \Sigma_{C,s}$. The stator end region $\Sigma_{E,s}$ is the location of the end-closure of the stator phase winding, which is considered to be developing mainly in the tangential direction. Both the rear and front stator end regions are generally characterised by the absence of ferromagnetic material. Similarly in other electrical machines that feature a rotor winding structure, for example, a cage-rotor IM, or a field wound synchronous motor, the rotor end region $\Sigma_{E,r}$ is the location of the phase winding conducting elements enabling a closure path for the flowing current. In SRIMs the electric and magnetic field share the same electromagnetic media and therefore the rotor end-region is (full or partially) filled with conductive (sometimes ferromagnetic) material as a continuous axial extension of the rotor structure itself or as solid end-rings. This enables the rotor current density field to find its natural closure path and localises this effect outside the central region of the device.

Having defined the domain of analysis, the geometry of the motion of the bodies of the device, the characteristic of the electromagnetic field in SRIM is now discussed. The state variable model is commonly adopted to characterise the behaviour of the machine. A set of electromagnetic state variables $\bar{i} \in \mathbb{R}^{n_E}$ is selected and highlighted in Figure 2.2. The state variables are usually selected as the currents flowing in the stator winding structure. The electromagnetic state of the machine is however determined by the state functions flux linkages defined as $\bar{\varphi}(\bar{i}, \bar{\chi}) : \mathbb{R}^{n_E \times n_M} \mapsto \mathbb{R}^{n_E}$ and determined according to the *Faraday-Lentz Law* [102]. The magnetic field distribution within the computational domain Σ is required in order to accurately estimate the electromagnetic state of the device and to achieve a quantitative description of the machine's behaviour. The *Maxwell* equation [103] governs the distribution of the electrical and magnetic vector fields at each point $P \in \Sigma \ \forall t \in \mathbb{R}$ and their solution is therefore required. According to the *Helmholtz Theorem*, the magnetic vector potential field $\vec{\mathbf{A}}({}^s\bar{p}, t) : (\Sigma \cup \mathbb{R}) \mapsto \mathbb{R}^3$ is defined as the vector field which describes the electromagnetic status of the device $\forall \ {}^s\bar{p} \in \Sigma$ and $t \in \mathbb{R}$ [104], where ${}^s\bar{p}$ is the vector of the coordinate of a generic point of the domain.

$$\vec{\mathbf{A}}({}^s\bar{p}, t) = A_r({}^s\bar{p}, t)\, {}^s\tilde{\mathbf{e}}_r + A_\theta({}^s\bar{p}, t)\, {}^s\tilde{\mathbf{e}}_\theta + A_z({}^s\bar{p}, t)\, {}^s\tilde{\mathbf{e}}_z \tag{2.2}$$

2.1.1 The 2-D Field Approximation

According to the shape and distribution of the active sides of the coils, the homogeneous characteristic of the constitutive material in combination with the geometry of the magnetic cores, the vector potential distribution in a significant part of the domain Σ of the machine features only the ${}^s\tilde{\mathbf{e}}_z$ component. Moreover, the energy transformation phenomena that take place in electrical machines are mainly concentrated in the main air gap region, Σ_g and in particular in the subset $\Sigma_{C,g}$ [101]. Combining the above consideration, an equivalent active computational domain $\Sigma_A \subset \Sigma$ is usually implemented for the evaluation of the performance of electrical machine. The fictitious domain is characterised by an electromagnetic field distribution which does not vary along the z-coordinate and can be approximated as bi-dimensional in nature.

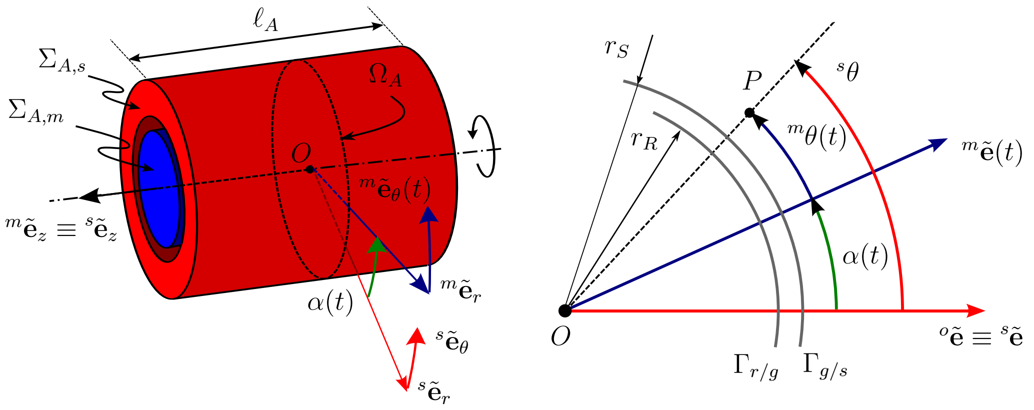

(a) 2-D model approximation **(b)** 2-D reference frame

Figure 2.4: Model reduction: 3-D → 2-D approximation

In Figure 2.4a the active part of the idealised machine model is presented. Within the defined region, the magnetic vector potential is considered featuring only the axial component.

$$\vec{\mathbf{A}}({}^s\bar{p}, t) \approx A_z({}^s r, {}^s\theta, t)\ {}^s\tilde{\mathbf{e}}_z \quad \forall\ {}^s r, {}^s\theta, {}^s z \in \Sigma_A \vee t \in \mathbb{R} \tag{2.3}$$

According to the *Maxwell* equations, the assumption of a bi-dimensional field distribution implies that the magnetic vector field function $\vec{\mathbf{B}}({}^s\bar{p}, t)$ and the magnetic strength vector field function $\vec{\mathbf{H}}({}^s\bar{p}, t)$ feature only radial and tangential components. Furthermore, the electric vector field function $\vec{\mathbf{E}}({}^s\bar{p}, t)$ and current density vector field $\vec{\mathbf{J}}({}^s\bar{p}, t)$ feature instead only the axial component.

The domain Σ_A where the above assumptions are valid consist of the stator, air gap and rotor subregion, defined as $\Sigma_{A,s}$, $\Sigma_{A,g}$ and $\Sigma_{A,r}$, respectively, highlighted in Figure 2.4a. The active stator region considered consists of a soft ferromagnetic region and the stator winding conducting elements. Thin laminations are adopted for the stator's magnetic core in order to minimise the eddy currents induced, which can be neglected. Applying *Ampere's law* [104] with the assumption of a high relative permeability and a negligible hysteresis effect of the stator soft ferromagnetic core materials, the magneto-motive-force (m.m.f.) drop related with the field lines inside the aforementioned core results negligible. The region of interest for the electromagnetic field distribution is therefore limited to $\tilde{\Sigma}_A = \Sigma_{A,g} \cup \Sigma_{A,r}$. However, the conductors of the stator phase winding, which defines the path of the electrical currents density field imposed, are located in dedicated slots in the stator core. In the central region of the device, the active sides of the winding structure as well as the stator slots geometry, runs parallel to the direction of the axial development of the structure. Let's define the equivalent stator current density as the infinitesimal current sheet imposed on the interface's cylindrical surface $\Omega_{s/g} : F \mapsto \mathbb{R}^2 := \partial\,\Sigma_{A,s} \cap \partial\Sigma_{A,g}$ with $F \subset \mathbb{R}^2$. It is considered featuring only the axial component and is constant along the z-coordinate, therefore $\vec{\mathbf{J}}_S({}^s\bar{p}, t) \triangleq J_S({}^s\theta, t)\ {}^s\tilde{\mathbf{e}}_z$ and is representative of the effect that the current flowing on the conductor of the stator phase winding has on the field distribution. The effect of the opening of the stator slot on the side facing the main air gap are accounted for in this equivalent model and therefore, the stator structure can be simplified further by considering an idealised magnetic core featuring a smooth cylindrical surface $\Omega_{s/g}$ facing the main air gap. The assumption of the bi-dimensional constant field along the axial coordinate allows a generic cross section $\Omega_A \in \mathbb{R}^2$ orthogonal to the axial development of the machine within its central region as the computational domain represented in Figure 2.4a. The surface Ω_A is considered as the generatrix of the domain $\tilde{\Sigma}_A \in \mathbb{R}^3$ by means of extrusion along the direction ${}^s\tilde{\mathbf{e}}_z$.

In Figure 2.4b, the reference frame's relative position for a generic time instant $t \in \mathbb{R}$ is defined by means of the angular coordinate $\alpha(t) = {}^s\theta - {}^m\theta(t)$. The position of the generic point that belongs to the domain $P \in \Omega_A$ is represented by its coordinates expressed either with respect to the mover reference frame $({}^m r, {}^m\theta(t))$ or the stator one $({}^s r, {}^s\theta)$. The *Galilean transformation* is therefore defined as

$$\bar{\mathcal{V}}_{s,m} \in \mathbb{R}^3 : ({}^s\bar{p}, t) \mapsto ({}^m\bar{p} - \bar{\mathcal{V}}_{s,m}\, t, t) \;\Rightarrow\; \bar{\mathcal{V}}_{s,m} = [\,0\ \alpha(t)\ 0\,]^T \tag{2.4}$$

The active length ℓ_A is defined as the axial development of Σ_A such as the energetic transformation effects are identical to the one that occurs in the real device [101]. An equivalent macroscopic description of the phenomena taking place in the non-active region $\Sigma_{NA} = \Sigma \setminus \Sigma_A$ is required in order to increase the accuracy of the calculations. The effect of the closure path of the stator and rotor winding structures is often included in the models while not modelled in terms of punctual field distribution. The above approximation has been widely adopted and validated for the analysis of various types of machine [65] featuring ${}^{\ell_A}/_{\ell_C} \approx (1 \div 0.9)$.

The rotor field distributions have an intrinsic three-dimensional nature in SRIMs. The effect in the end region of the rotor structure has quite a significant impact on the performance and can not be neglected. The bi-dimensional approximation is widely adopted, however particular attention is dedicated to the inclusion of the rotor end region effect within the domain Ω_A and is discussed later in the chapter.

2.1.2 The 2-D Eddy-Current problem

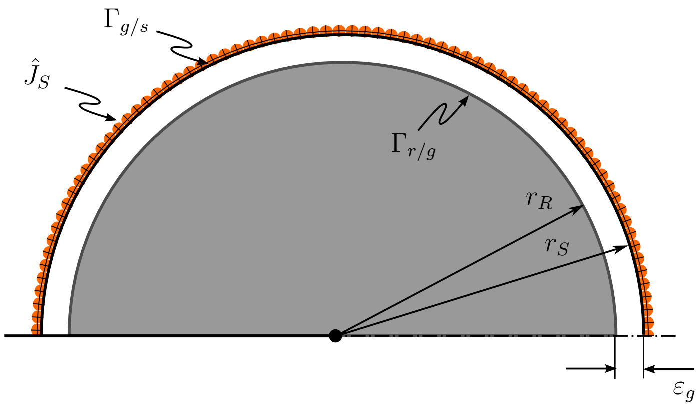

Figure 2.5: Smooth solid rotor model for 2-D eddy-current problem

The bi-dimensional computational domain considered is formed of the union of the air gap and the rotor subset $\Omega_A = \Omega_{A,r} \cup \Omega_{A,g}$ and is considered as an idealised cross section of the machine orthogonal to the direction ${}^s\tilde{\mathbf{e}}_z$. Figure 2.5 presents the schematic of the bi-dimensional domain. The rotor subset $\Omega_{A,r}$ is limited by the closed continuous curve $\Gamma_{r/g} : I \mapsto \mathbb{R} := \partial\Omega_{A,r} \cap \partial\Omega_{A,g}$ with $I \subset \mathbb{R}$. The cylindrical nature of the structures considered uniquely identifies the curve $\Gamma_{r/g}$ with its radius, namely the rotor outer bore radius $r_R > 0$. The air gap subset is instead defined as the region of the space $\mathbb{R}^2$ limited by

$\Gamma_{r/g}$ and $\Gamma_{g/s} : I \mapsto \mathbb{R} := \partial\Omega_{A,g} \cap \partial\Omega_{A,s}$. Similarly, the curve $\Gamma_{g/s}$ is uniquely identified by the stator inner bore radius $r_S > r_R > 0$. The main air gap thickness results $\varepsilon_g = r_S - r_R$. The finite computational domain are therefore defined as (2.5) and (2.6) $\forall -{}^{\ell_A}/_2 < z < {}^{\ell_A}/_2$

$$\Sigma'_{A,g} := \left\{ (r,\theta) \in \mathbb{R}^2 \,\middle|\, 0 < \theta < 2\,\pi\,,\; r_R < r < r_S \right\} \tag{2.5}$$

$$\Sigma'_{A,r} := \left\{ (r,\theta) \in \mathbb{R}^2 \,\middle|\, 0 < \theta < 2\,\pi\,,\; 0 < r \leq r_R \right\} \tag{2.6}$$

The electromagnetic characteristics of the materials in the different domains strongly affect the field distribution and the phenomena that take place.

The main air gap considered is filled with an isotropic homogeneous medium which features a constant permeability ($\mu_g \approx \mu_0$) and is non-conductive ($\sigma_g = 0$), having defined $\mu_0 = 4\pi \cdot 10^{-7}\,[{}^{H}/_{m}]$. Let us define the air gap vector potential function in $\Omega_{A,g}$ as $\vec{\mathbf{A}}_g({}^s\bar{p},t) \triangleq A_{g,z}({}^s\bar{p},t)\;{}^s\tilde{\mathbf{e}}_z$. According to *Maxwell's* equations, the second order elliptic partial differential equation (PDE) which governs the field distribution in $\Omega_{A,g}$ takes the form of the scalar *Laplace* equation (2.7) [102]

$$\nabla^2 A_{g,z}({}^s\bar{p},t) = 0 \quad \forall\, P \in \Omega_{A,g} \tag{2.7}$$

The rotor domain $\Omega_{A,r}$ considered constitutes a non-homogeneous isotropic material which results conductive and features a linear magnetic behaviour $\mu_r({}^s\bar{p},t) = \mu_{r,R}({}^s\bar{p},t)\,\mu_0$. The relative permeability of the rotor material $\mu_{r,R}({}^s\bar{p},t)$ and its electric conductivity $\sigma_r({}^s\bar{p},t) \neq 0$ are considered as function of the spatial coordinates and time at first instance. Defining $\vec{\mathbf{A}}_r({}^s\bar{p},t) \triangleq A_{r,z}({}^s\bar{p},t)\,\tilde{\mathbf{e}}_z$ as the rotor vector potential function in the rotor domain $\Omega_{A,r}$, the electromagnetic problem is defined by the second order elliptic PDE (2.8) [102]

$$\nabla^2 A_{r,z}({}^s\bar{p},t) = \mu_r({}^s\bar{p},t)\,\sigma_r({}^s\bar{p},t)\,\frac{\partial\, A_{r,z}({}^s\bar{p},t)}{\partial\, t} \quad \forall\, P \in \Omega_{A,m} \tag{2.8}$$

The dependency of the rotor material parameters upon the spatial coordinates and the time enables the solution for the homogeneous smooth SR case to be extended to a multitude of cases. Different rotor structures are able to be investigate such as copper coated SRIM and in general concentric multi-layered structures. The temperature distribution, magnetic loading, mechanical stresses, operative frequency in general have an impact on the material performances which can be adjusted accordingly. Finally, the formalisation of the problem enables to extend the problem defining an *"ah hoc"* discretisation, in order to increase the accuracy of the calculation or account for different material properties. It is important to note that the magnetic field distribution problem in $\Omega_{A,r}$ degenerates to (2.7) for a time-invariant magnetic vector potential.

2.1.3 The Harmonic Decomposition

The problem of the eddy current in the time domain is defined by (2.7) and (2.8). The calculation of the steady state solution is required. A subset of the possible solutions is investigated as significant for this study. Two additional assumptions have to be considered:

(E.9) periodic time-varying nature of the electromagnetic field quantities features a constant fundamental angular frequency ω_e;

(E.10) constant mechanical angular velocity $\vec{\omega}_m = \omega_m \, {}^m\tilde{\mathbf{e}}_z$ of the rotor body.

The axisymmetric nature of the domain $\Sigma_A^{'}$ in combination with the hypothesis **[(E.9)]** depicts a scenario in which the electromagnetic function is periodic with respect to both the angular coordinate ${}^s\theta$ and the time variable. Any periodic real function may be written as a series of sinusoidal terms, also called *Fourier series*. *Euler's formula* defines the *Fourier series* in the complex domain $\mathbb{C}$ which present an equivalent harmonic representation of the electromagnetic fields defined in the domain Ω_A. The magnetic vector potential in the air gap region $\Omega_{A,g}$ and mover region $\Omega_{A,m}$ are therefore expressed as (2.9a) and (2.9b) respectively.

$$A_{g,z}({}^s r, {}^s\theta, t) = \Re\left\{\sum_{\varsigma\in\mathbb{Z}}\sum_{\nu\in\mathbb{Z}} {}^{\nu\varsigma}\hat{A}_{g,z}({}^s r)\, e^{\jmath\,\nu\omega_e t}\, e^{-\jmath\,\varsigma\, p\, {}^s\theta}\right\} \;\forall\, P \in \Omega_{A,g} \tag{2.9a}$$

$$A_{r,z}({}^s r, {}^s\theta, t) = \Re\left\{\sum_{\varsigma\in\mathbb{Z}}\sum_{\nu\in\mathbb{Z}} {}^{\nu\varsigma}\hat{A}_{r,z}({}^s r)\, e^{\jmath\,\nu\omega_e t}\, e^{-\jmath\,\varsigma\, p\, {}^s\theta}\right\} \;\forall\, P \in \Omega_{A,m} \tag{2.9b}$$

where $\Re$ denotes the real part of the complex number and $\jmath = \sqrt{-1}$. The periodicity of the electromagnetic functions in the cylindrical domain Ω_A with respect to the tangential coordinates ${}^{s}\theta$ and ${}^{m}\theta(t)$ is defined by the number of pole pairs $p \in \mathbb{N}$ introduced in (2.9a) and (2.9b). $\nu \in \mathbb{Z}$ and $\varsigma \in \mathbb{Z}$ are the harmonic orders in the time and spatial domain, respectively and the notation $\wedge$ is introduced to identify quantities defined in the complex domain. The space harmonic order considered is directly related with the number of inner stator bore slot openings featured [90, 105].

A reference frame synchronous with respect to the stator's fundamental electrical quantities of frequency ω_e is defined by ${}^{e}\tilde{\mathbf{e}}(t)$. Moreover, the hypothesis **[(E.10)]** identifies the subset of all the possible mechanical operative conditions discussed here. The relative motion of the static and moving bodies and consequently of their reference frames is considered to happen at a constant angular speed. According to Figure 2.4b, the reference frame motion is described by the relation $\alpha(t) = \dot{\alpha}\, t + \alpha(t_0)$ where $\alpha(t_0) = 0$ and $\dot{\alpha} = \omega_m$. An additional reference frame ${}^{r}\tilde{\mathbf{e}}(t)$ is introduced as rotating at a constant electrical angular speed, $\omega_r = p\,\omega_m$. The steady state, constant speed operative condition of IMs is therefore defined by $\chi(t) = {}^{e}\theta(t) - {}^{r}\theta(t)$ according to Figure 2.6.

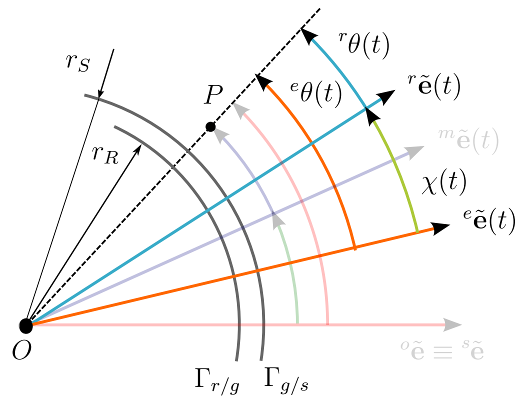

Figure 2.6: Moving reference frames representation for time harmonic 2-D eddy current problem

Substituting the previous transformation in the above relation, the *fundamental slip*, 's' parameter is introduced as the per-unit measure of the fundamental angular speed difference between the stator's and rotor's electromagnetic field with respect to the stator field's fundamental angular speed.

$$s = \frac{\omega_r}{\omega_e} = \frac{\omega_e - p\,\omega_m}{\omega_e} \tag{2.10}$$

The *Galilean transformation*, which links the stator reference frame to the rotor reference frame, is therefore defined as $\bar{\mathcal{V}}_{s,r} = [0 \quad -(1-s)\,\omega_e\,t \quad 0]^T$. The above considerations group the exponential of the harmonic decomposed form of the rotor vector potential and defines the *harmonic slip*

$$^{\nu\varsigma}s = \nu - p\varsigma\,(1-s) \tag{2.11}$$

The stator slotting and more complex rotor structures introduce space-harmonics in the magnetic field, which are important to be considered in order to correctly estimate the behaviour of the device. Furthermore, the time varying nature of the fields is considered. Power electronic devices are currently widely adopted in variable speed drives and for high speed applications [4], thus leading to their current and voltage waveforms to exhibit a harmonic content that impacts on the main characteristic of the machine. The rotor considered in the analysis features a multi-layered structure and therefore the rotor material is defined as isotropic, time-invariant and non-homogeneous but only in the radial distribution of the material properties, resulting in $\mu_r(^s\bar{p},t) \approx \mu_r(^s r)$ and $\sigma_r(^s\bar{p},t) \approx \sigma_r(^s r)$. The harmonic formulation of the vector potential (2.9b) with respect to the rotor reference frame therefore results in (2.12)

$$A'_{r,z}(^m r, {}^m\theta(t), t) = \Re\left\{\sum_{\varsigma\in\mathbb{Z}}\sum_{\nu\in\mathbb{Z}} {}^{\nu\varsigma}\hat{A}'_{r,z}(^m r)\, e^{\jmath\,^{\nu\varsigma}\omega\, t}\, e^{-\jmath\,\varsigma\, p\,^m\theta(t)}\right\} \tag{2.12}$$

having defined $^{\nu\varsigma}\omega = {}^{\nu\varsigma}s\,\omega_e$. The governing equation of the field distribution in the main air gap (2.7) and rotor structure (2.8) can be written in their complex form as (2.13a) and (2.13b) for the stator and rotor reference frame, respectively.

$$\nabla^2\ {}^{\nu\varsigma}\hat{A}_{g,z}(^s r) = 0 \tag{2.13a}$$

$$\nabla^2\ {}^{\nu\varsigma}\hat{A}'_{r,z}(^m r) = \jmath\ {}^{\nu\varsigma}\omega\,\mu_r(^m r)\,\sigma_r(^m r)\ {}^{\nu\varsigma}\hat{A}'_{r,z}(^m r) \tag{2.13b}$$

The solution of (2.13b) in a closed form is possible in the case of a constant rotor magnetic relative permeability and electrical resistivity.

The non-linear nature of the problem induces an inaccurate prediction when the saturation has a relevant effect on the field distribution. Different methods have been proposed to account for the magnetic saturation on the field diffusion in solid ferromagnetic cores. In literature, various methods can be found which attempt to include non-linear effects in the modelling. The *Agarwal* [106] approximation is commonly used to account for the saturation curve of the material in electromagnetic field calculations; *Barth* considered a complex Fourier decomposition of the electromagnetic field in solid iron where the coefficient may be calculated by way of harmonic analysis of the measured, static hysteresis loops. *Wood* [107] develop an approximated analytical model based on [106] having considered high saturated rotor media. Furthermore, the impact of the hysteresis losses in a SRIM could significantly affect the power balance calculation and accurate models have been proposed to account for this effect. *O'Kelly* [108] presented a solution of the electromagnetic field distribution including both hysteresis and eddy currents effects by considering only the fundamental harmonics and having the hysteresis modelled as an idealised elliptical magnetisation curve. Different loss models are proposed in [109] based on modelling the electromagnetic properties of the soft ferromagnetic material. The complex permeability is introduced as an alternative analytical method to account for the hysteresis losses and saturation effects in the field distributions within a solid ferromagnetic material [110]. The definition of the complex relative permeability for solid ferromagnetic steel (2.14) is discussed and experimentally validated in [26, 110].

$$\hat{\mu}_r = \mu_{r,R}(\mu^{'} - \jmath\,\mu^{''}) = \mu_{r,R}\left(\alpha_R\,\alpha_X - \jmath\left[\frac{\alpha_R^2 - \alpha_X^2}{2}\right]\right) \tag{2.14}$$

Gieras in [110] proposes $\alpha_R = 1.45$ and $\alpha_X = 0.85$ as reasonable values for a solid material thus leading to $|\hat{\mu}_r| = 1.4125$ and $\angle\hat{\mu}_r = -29.24°$. The equations (2.13a) and (2.13b) have been defined considering a complex rotor permeability leading to interesting conclusions and accurate predictions presented in [26]. The above techniques leads to approximated solution. Non-linear FEA methods are capable of tackling the problem of soft iron material saturation,however requiring their correct description results in a non-trivial task and increased computational time.

2.1.4 Discrete Domain Method (DDM)

The accuracy of the computation highly depends on the quality of the problems description and formalisation. The penetration depth of the time-space harmonics couple (ν, ς) strongly impacts the field distribution calculation as well as the computational domain geometry [111]. The effect of the rotor curvature impacts the result of the electromagnetic calculation especially for low harmonic orders. The geometrical nature of the structure is accounted for by solving the PDE in a cylindrical coordinate system as defined in the model presented in Figure 2.7a. The accuracy of the numerical solution of the vector potential is increased by means of considering the equations defined with respect to a Cartesian (high harmonic order) coordinate system, depicted in Figure 2.7b.

The above considerations allow a more stable solution of the field distribution. In order to improve the accuracy, the domain subdivision is also considered [95, 96, 105]. In general, the layer thickness distribution can be arbitrarily chosen to improve the solution quality or to reduce the computational time. As the penetration depth of the field in the rotor media is variable with respect to the slip frequency and the spatial harmonic order considered, a high spatial order leads to low penetration depth values and therefore the accuracy of the mesh in the outer region of the rotor media is required to achieve high computational accuracy. The extension of the governing equations (2.13a) and (2.13b) assumes that the variation of the vector potential within each layer is negligible [112, 113]. The considerations about the full solid structure are still valid if a concentric multi-layer model is considered.

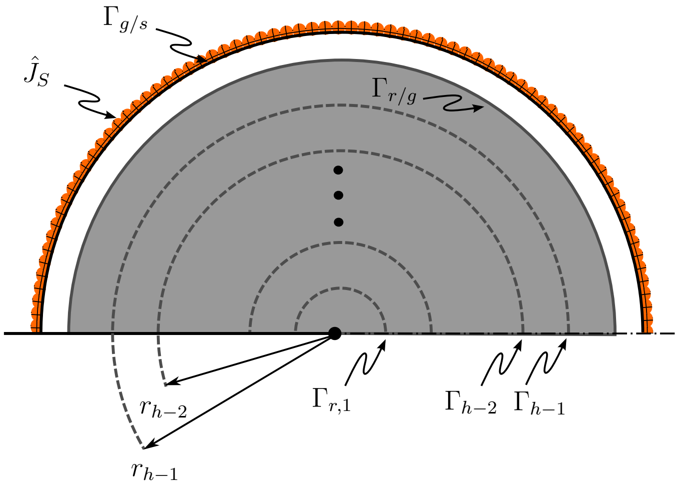

(a) Cylindrical model (low order space harmonics)

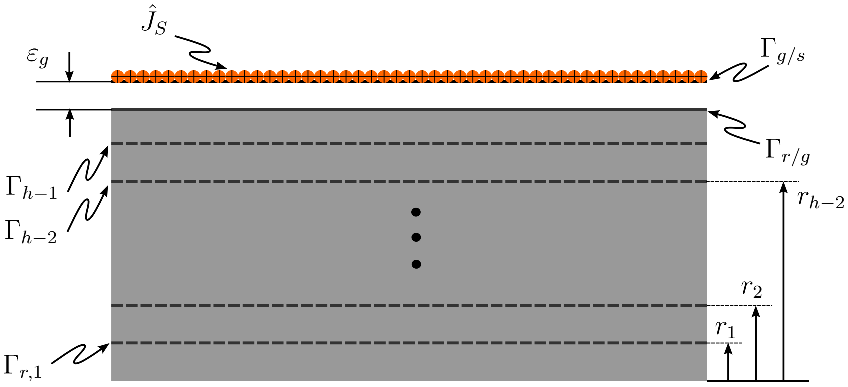

(b) Cartesian model (high order space harmonics)

Figure 2.7: Multi-layer model for time harmonic 2-D eddy current problem

Let's define $L \in \mathbb{N}$ as the total number of layers in which the rotor structure is divided. The computational domain results from the union of all the concentric sub-domains $\Omega_{A,r} = \bigcup_{h=1}^{L} \Omega_h$. The h^{th} sub-domain is defined as the region of the space $\Omega_{A,r}$ limited by means of Γ_h and Γ_{h+1} characterised by the radii r_h and r_{h+1}, respectively. The inner and outer rotor radii therefore results in $r_I = r_0$ and $r_R = r_{L+1}$, respectively. Each domain is characterised by its electromagnetic, thermal, and mechanical characteristics which are assumed to be constant. According to the previous considerations, (2.13b) can be defined as the governing equation for the h^{th} layer characterised by means of a relative magnetic permeability μ_h and conductivity σ_h. Defining ${}^{\nu\varsigma}\hat{A}'_h$ as the complex form of the (ν, ς) harmonic component of the magnetic vector potential, (2.15) is considered as the fundamental equation for the magnetic field distribution within the h^{th} layer.

$$\nabla^2 \; {}^{\nu\varsigma}\hat{A}'_h({}^m r) = \jmath \; {}^{\nu\varsigma}\omega \, \hat{\mu}_h \, \sigma_h \; {}^{\nu\varsigma}\hat{A}'_h({}^m r) \tag{2.15}$$

The different penetration depths ${}^{\nu\varsigma}\delta$ of the electromagnetic field for a set (ν, ς) of time-spatial harmonics lead to a non-accurate solution if ${}^{\nu\varsigma}\delta \ll {}^{(r_R - r_I)}/_L$. Adaptive discretization can be used to increase the solution for each harmonic order by defining the inner diameter of the computational domain as a function of the penetration depth for the time-space harmonic considered. Linear distribution of the nodes can also be considered. Alternatively, the *Legendre-Gauss-Lobatto* node distribution based on the zeros of the *Chebychev* polynomials is considered as the solution of the *Helmholtz* equation [114]. The radial position of the node distribution can be defined by the layer thickness. However, high resolution is required on the outer bore of the rotor whereas the field distribution in the center of the rotating element is not of interest.

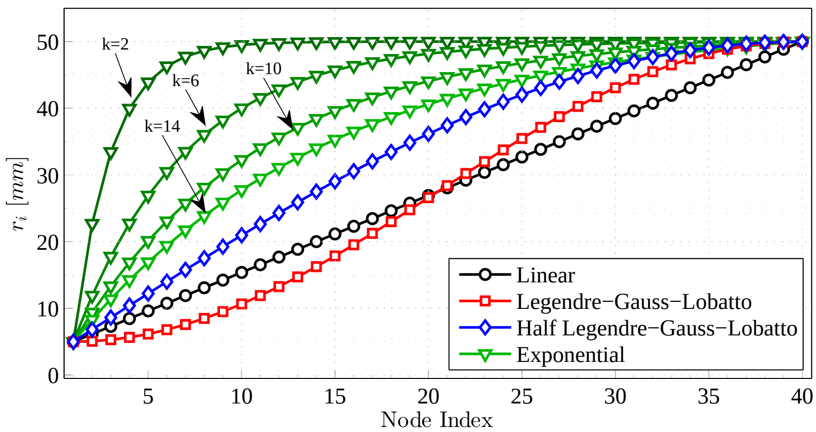

Figure 2.8: Legendre-Gauss-Lobatto and linear equispaced node distribution for $L = 40$, $r_c = 5\,[mm]$ and $r_R = 50\,[mm]$

The *Legendre-Gauss-Lobatto* can therefore be modified to enhance the resolution only in proximity of the outer rotor region. The exponential node distribution can also be considered and can be tuned to achieve the node distribution that minimises the computational error. The exponential distribution can be defined as function of a parameter k which enables the tuning of the curve. A comparison of the radial distribution against the node index is proposed in Figure 2.8. The calculations of the field distributions presented in the following sections are proposed for a continuous distribution and can be extended to the layered computational domain. The flexibility of the single mesh model proposed can be exploited to account for the material property variation such as the saturation or the dependency of the resistivity on the temperature. Extending the concept, the proposed modelling tool enables analysis of different rotor topologies (smooth solid rotor, coated solid rotor, composite solid rotor) as in general it is possible to account for inhomogeneous rotor structures. Moreover, focusing on the multi-physics approach to analyse the device, a unique mesh is adopted enabling the transfer of the computed quantities between the different physics models, therefore, increasing the accuracy and efficiency of the calculation.

2.1.5 Cylindrical coordinate system solution

The solution of (2.13a) and (2.15) considering a cylindrical reference system as presented in Figure 2.7a is required to account for the geometry of the structure. The layered model is considered as a general case, which includes the solution for a smooth solid rotor with constant rotor parameters. The source term is represented with a current sheet distribution over the inner stator radius r_S.

$$\vec{\mathbf{J}} = \Re\left\{\sum_{\varsigma\in\mathbb{Z}}\sum_{\nu\in\mathbb{Z}} {}^{\nu,\varsigma}\hat{J}_{S,z}(r_S)\, e^{\jmath\,{}^{\nu\varsigma}\omega\, t}\, e^{-\jmath\,\varsigma\, p\,{}^{s}\theta}\right\}\hat{\mathbf{e}}_{\mathbf{z}} \tag{2.16}$$

The (ν, ς) harmonic component of the current sheet distribution is defined to account for the slotting effect and conductor distributions by means of the harmonic winding factor ${}^{\varsigma}\kappa_W$ for the ${}^{\nu}I$ time harmonic component of the supplied current.

$${}^{\nu,\varsigma}\hat{J}_{S,z}(r_S) = {}^{\varsigma}\kappa_W\, \frac{3\, N_{ph}\, \sqrt{2}\; {}^{\nu}I}{\pi\, r_S} \tag{2.17}$$

having defined ${}^{\varsigma}\kappa_W = {}^{\varsigma}\kappa_C\;{}^{\varsigma}\kappa_P\;{}^{\varsigma}\kappa_S$ as the connection factor, short pitch connection factor and slotting factor [115], respectively. Let's define the separation constant ${}^{\nu\varsigma}\hat{\lambda}_h^2 = \jmath\;{}^{\nu\varsigma}\omega\,\hat{\mu}_r(\tilde{r}_h)\,\sigma_r(\tilde{r}_h)$ where $\tilde{r}_h$ is the mid-radius of the h^{th} layer ($\tilde{r}_h = {}^1\!/_2[r_h + r_{h+1}]$). (2.13a) and (2.15) can be therefore expressed as the following:

$$\frac{\partial^2\,{}^{\nu\varsigma}\hat{A}_{g,z}({}^s r)}{\partial\,r^2} + \frac{1}{r}\,\frac{\partial\,\hat{A}_{g,z}({}^s r)}{\partial\,r} - \frac{(\varsigma\,p)^2}{r^2}\,\hat{A}_{g,z}({}^s r) = 0 \tag{2.18}$$

$$\frac{\partial^2\,{}^{\nu\varsigma}\hat{A}'_h({}^m r)}{\partial\,r^2} + \frac{1}{r}\,\frac{\partial\,{}^{\nu\varsigma}\hat{A}'_h({}^m r)}{\partial\,r} - \left({}^{\nu\varsigma}\hat{\lambda}_h^2 + \frac{(\varsigma\,p)^2}{r^2}\right)\,{}^{\nu\varsigma}\hat{A}'_h({}^m r) = 0 \tag{2.19}$$

The general solution of the (ν, ς) time harmonic of the vector potential distribution in the rotor and air gap domain are (2.20) and (2.21), respectively.

$${}^{\nu\varsigma}\hat{A}_{g,z}(r) = \begin{cases} {}^{\nu\varsigma}\mathcal{A}_{1,g}\,r^{\varsigma\,p} + {}^{\nu\varsigma}\mathcal{A}_{2,g}\,r^{-\varsigma\,p} & \varsigma \neq 0 \\ \mathcal{A}_{1,g}\,ln(r) + \mathcal{A}_{2,g} & \varsigma = 0 \end{cases} \tag{2.20}$$

$${}^{\nu\varsigma}\hat{A}'_h(r) = {}^{\nu\varsigma}\mathcal{B}_{1,h}\,\mathcal{I}_{(\varsigma\,p)}\left(r\;{}^{\nu\varsigma}\hat{\lambda}_h\right) + {}^{\nu\varsigma}\mathcal{B}_{2,h}\,\mathcal{K}_{(\varsigma\,p)}\left(r\;{}^{\nu\varsigma}\hat{\lambda}_h\right) \tag{2.21}$$

where ${}^{\nu\varsigma}\mathcal{A}_{1,g}$ and ${}^{\nu\varsigma}\mathcal{A}_{2,g}$ are the air gap integration constants, ${}^{\nu\varsigma}\mathcal{B}_{1,h}$ and ${}^{\nu\varsigma}\mathcal{B}_{2,h}$ are the h^{th} layer integration constants. $\mathcal{I}_{(\varsigma\,p)}$ and $\mathcal{K}_{(\varsigma\,p)}$ are the *modified Bessel* functions of the first and second orders, respectively [116].

2.1.6 Cartesian coordinate system

Similarly to the cylindrical coordinate system case, the solution of Cartesian system is considered. The vector potential can be expressed in its harmonic decomposition form as (2.22a) for the main air gap, and (2.22b) for the rotor structure.

$$A_{g,z}({}^s x, {}^s y, t) = \Re\left\{\sum_{\nu\in\mathbb{Z}}\sum_{\varsigma\in\mathbb{Z}}\,{}^{\nu\varsigma}\hat{A}_{g,z}({}^s y)\,e^{\jmath\,\nu\,\omega_e\,t}\,e^{-\jmath\,\varsigma\,\xi\;{}^s x}\right\} \tag{2.22a}$$

$$A'_{r,z}({}^m x, {}^m y, t) = \Re\left\{\sum_{\nu\in\mathbb{Z}}\sum_{\varsigma\in\mathbb{Z}}\,{}^{\nu\varsigma}\hat{A}'_{r,z}({}^m y)\,e^{\jmath\,\nu\;{}^{\nu\varsigma}\omega\,t}\,e^{-\jmath\,\varsigma\,\xi\;{}^m x}\right\} \tag{2.22b}$$

where $\xi = {}^p\!/_{r_S}$ is the base wave-number [56]. The separation constant is defined as ${}^{\nu\varsigma}\hat{\gamma}_h^2 = {}^{\nu\varsigma}\hat{\lambda}_h^2 + (\varsigma\,\xi)^2$. The governing equations of the field distribution in the domains reported below are obtained combining (2.22a) and (2.22b) with (2.7) and (2.8), respectively.

$$\frac{\partial^2 \, {}^{\nu\varsigma}\hat{A}_{g,z}({}^{s}y)}{\partial \, y^2} - (\varsigma \, \xi)^2 \; {}^{\nu\varsigma}\hat{A}_{g,z}({}^{s}y) = 0 \tag{2.23}$$

$$\frac{\partial^2 \, {}^{\nu\varsigma}\hat{A}'_{h}({}^{m}y)}{\partial \, y^2} - \left[(\varsigma \, \xi)^2 + {}^{\nu\varsigma}\hat{\lambda}^2_h\right] \; {}^{\nu\varsigma}\hat{A}'_{h}({}^{m}y) = 0 \tag{2.24}$$

The general solution of the (ν, ς) time-space harmonics of the vector potential distribution in the rotor and air gap domain are (2.25) and (2.26), respectively.

$$ {}^{\nu\varsigma}\hat{A}_{g,z}(y) = \begin{cases} {}^{\nu\varsigma}\mathcal{A}_{1,g} \, e^{\varsigma \, \xi \, y} + {}^{\nu\varsigma}\mathcal{A}_{2,g} \, e^{-\varsigma \, \xi \, y} & \varsigma \neq 0 \\ {}^{\nu\varsigma}\mathcal{A}_{1,g} \, y + {}^{\nu\varsigma}\mathcal{A}_{2,g} & \varsigma = 0 \end{cases} \tag{2.25}$$

$$ {}^{\nu\varsigma}\hat{A}'_{h}(y) = {}^{\nu\varsigma}\mathcal{B}_{1,r} \, e^{{}^{\nu\varsigma}\hat{\gamma}_h \, y} + {}^{\nu\varsigma}\mathcal{B}_{2,r} \, e^{-\,{}^{\nu\varsigma}\hat{\gamma}_h \, y} \tag{2.26}$$

2.1.7 Boundary Conditions

The calculation of the solution for each single space-time harmonic of the vector potential requires a consistent set of boundary conditions to be imposed on the computational domain. The definition of the vector potential and the constitutive equation enables the evaluation of the flux density and field strength, respectively. Considering a model featuring $\tilde{L} : \tilde{L} > L$ sub-domains (including the main air gap), the boundary conditions are defined for all the interfaces between each layer and different sub-domains in order to achieve a consistent set of linear equations. The boundary conditions at the interface Γ_i with $i \in \{1 \div \tilde{L}\}$ are defined as (2.27)

$$\begin{cases} \vec{n} \, \cdot \, \left(\vec{\mathbf{B}}_i - \vec{\mathbf{B}}_{i+1}\right) = 0 \\ \vec{n} \, \times \, \left(\vec{\mathbf{H}}_i - \vec{\mathbf{H}}_{i+1}\right) = \vec{J} \end{cases} \tag{2.27}$$

The complex form of (2.27) imposes a consistent set of conditions that result in a system of linear equations. The matrix ${}^{\nu\varsigma}\hat{\mathbf{M}}$ can be generated by collecting all the coefficients of the linear system and the vector of the integration constant ${}^{\nu\varsigma}\hat{\vec{c}}$ is calculated according to (2.28)

$$ {}^{\nu\varsigma}\hat{\vec{c}} = {}^{\nu\varsigma}\hat{\mathbf{M}}^{-1} \; {}^{\nu\varsigma}\hat{\vec{f}} \tag{2.28}$$

where ${}^{\nu\varsigma}\hat{\hat{f}}$ is the vector of the known terms resulting from (2.27). The conditions in (2.27) can be expressed in a simplified form as presented in (2.29) $\forall i \in \mathbb{N} :\ 0 < i < \tilde{L}$, respectively considering their harmonic form as $\vec{n} \cdot \left({}^{\nu\varsigma}\vec{\mathbf{B}}_i - {}^{\nu\varsigma}\vec{\mathbf{B}}_{i+1}\right) = 0$ and $\vec{n} \times \left({}^{\nu\varsigma}\vec{\mathbf{H}}_h - {}^{\nu\varsigma}\vec{\mathbf{H}}_{h+1}\right) = {}^{\nu\varsigma}\vec{J}_{h,z}$.

$$ {}^{\nu\varsigma}\hat{A}_i(r)\Big|_{r_i} = {}^{\nu\varsigma}\hat{A}_{i+1}(r)\Big|_{r_i} \tag{2.29a}$$

$$\begin{cases} \dfrac{\partial\, {}^{\nu\varsigma}\hat{A}_i(r)}{\partial\, r}\Big|_{r_i} = \dfrac{\hat{\mu}_{r,i}}{\hat{\mu}_{r,i+1}}\, \dfrac{\partial\, {}^{\nu\varsigma}\hat{A}_{i+1}(r)}{\partial\, r}\Big|_{r_i} & \text{if } \nexists\, \hat{J}_{z,i} \in \Gamma_i \\ \dfrac{\partial\, {}^{\nu\varsigma}\hat{A}_i(r)}{\partial\, r}\Big|_{r_i} = \dfrac{\hat{\mu}_{r,i}}{\hat{\mu}_{r,i+1}}\, \dfrac{\partial\, {}^{\nu\varsigma}\hat{A}_{i+1}(r)}{\partial\, r}\Big|_{r_i} + \hat{\mu}_{r,i}\, {}^{\nu\varsigma}\hat{J}_{i,z} & \text{if } \exists\, \hat{J}_{z,i} \in \Gamma_i \end{cases} \tag{2.29b}$$

The resulting system of linear equations have to be solved $\forall\, \nu \in \mathbb{Z}$ and $\forall\, \varsigma \in \mathbb{Z}$. However, the matrix ${}^{\nu\varsigma}\hat{\mathbf{M}}$ is ill-conditioned for high harmonic order and therefore the accuracy of the calculation drastically decreases. Pre-conditioning and *ah hoc* techniques (e.g. pseudo-inverse) can be applied to increase the accuracy of the inverse matrix calculation [117].

The electromagnetic field in a fictitious stator structure [118] consisting of a solid ring of magnetically permeable material ($\mu_{r,s} \neq +\infty$) can be easily included in the calculation. The governing equation of the magnetic field distribution results as (2.7) thus featuring a generic solution as proposed in (2.20)-(2.25). The boundary condition at the outer stator bore is therefore required and results in (2.30)

$$\vec{n} \cdot {}^{\nu\varsigma}\vec{\mathbf{B}}_S(r_e) = \vec{0} \Rightarrow {}^{\nu\varsigma}\hat{A}_S(r)\Big|_{r_e} = 0 \tag{2.30}$$

where r_e is the external stator radius and the right subscript, S in the magnetic field and vector potential is referred to as the stator region. The rotor structure, featuring an inner bore defined by Γ_0 is characterised by $r_I = r_0 \neq 0$ requires a boundary condition identical to (2.30) to be imposed as the vector potential must vanish outside the computational domain. The analysis of the matrix ${}^{\nu\varsigma}\hat{\mathbf{M}}$ gives important information about the accuracy of the solution calculated. The condition number m_c as well as the determinant and the study of the eigenvalues of the matrix identify the peculiarities of the problem defined and the accuracy of the solution.

2.1.8 Power and Torque

Conservation of energy allows the power balance equation for the device to be determined. The generic power flow is represented in Figure 2.9. The power transformation that takes place in the electro-magneto-mechanical device can be quantitatively described considering the electrical and mechanical ports, n_E and n_M, respectively. The efficiency parameter [119] is commonly used to describe the capability of a device to transform electrical power into mechanical (or vice-versa) with respect to the other power generated during the process (referred as power losses).

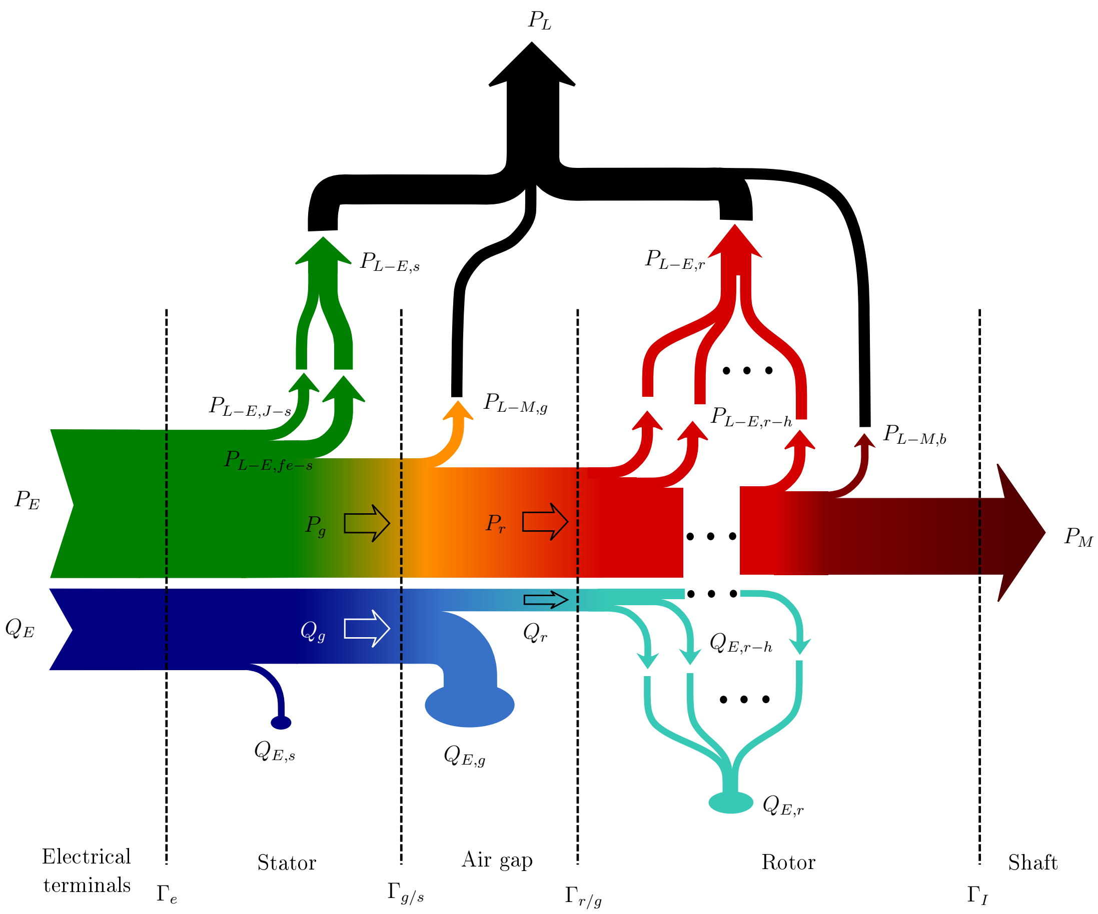

Figure 2.9: Power balance sankey diagram

The mechanical power as well as the loss components are important to be computed and correctly located within the structure of the device. This enables appropriate cooling techniques to be put in place and for the material properties and structure geometry to be chosen to maximise the efficiency. The consideration on the power flow and losses calculation relies on an additional assumption for the model

(E.11) the materials operate at their steady state temperature and the factor $\kappa_{T,*}(T_*)$ is defined to account for the temperature dependency.

The steady state temperature can be known or computed with thermal calculations. The subscript $*$ in **(E.11)** is defined and relates to the main temperature varying material of the device.

There are three main energy storage elements in the device. The electromagnetic energy is stored in the magnetic field, the mechanical energy is stored in the rotating inertia, and the thermal energy is stored in the heat capacity of the elements. The active and reactive electrical powers associated with the electrical ports are written as the sum of the product of the terminal voltages and the currents flowing in the stator winding of the machine. The apparent power under a balanced sinusoidal supply can be computed as

$$\hat{W}_E = \frac{n_E}{2} \left\{ \sum_{\nu \in \mathbb{Z}} {}^{\nu}\hat{V}_S \; {}^{\nu}\hat{I}_S^* \right\} = P_E + \jmath Q_E \tag{2.31}$$

The power flow from the phase winding terminals to the output shaft can be followed and the loss components identified as depicted in Figure 2.9. The currents flowing in the n_E phases generate an electromagnetic field within the structure of the machine. The power which flows in the main air gap from the stator structure results in $P_g = P_E - P_{L-E,s}$, where the electromagnetic losses of the stator are consistent of the two main components, namely the iron and conductors losses, $P_{L-E,fe-s}$ and $P_{L-E,J-s}$, respectively. The stator iron losses mainly consist of the eddy current and hysteresis losses. The computation of the iron losses in the soft ferromagnetic material is a non-trivial task [120]. Empirical formulas have been proposed as well as equivalent models for the electromagnetic characteristic of the material. Experimental curves are considered for different saturation levels and operational frequencies. However, the electromagnetic field polarisation in the stator core has to be accounted for as well as local saturation, which makes the computation of the total iron losses a very difficult task.

The resistive losses in the stator winding structure can be computed according to *Ohm's* Law.

$$P_{L-E,J-s} = n_E \, \kappa_{ac}(f_s) \, \kappa_{\tau,s}(T_{sw}) \, R_{ph} \, I_{rms}^2 \tag{2.32}$$

where R_{ph} is the DC phase resistance evaluated at the temperature $T_{sw,0}$, $\kappa_{\tau,s}(T_{sw}) = 1 + \alpha_s[T_{sw} - T_{sw,0}]$ is the temperature correction factor and I_{rms} is the *rms* current flowing in the electrical wires. In high speed applications, the high electrical frequency of the currents flowing in the conductors is a critical factor. The DC resistance R_{ph} of the single phase can be easily computed and measured, however, the skin and proximity effects are relevant when the frequency of the electrical quantities increase and then have to be accounted for [121]. Litz wires are the technological solution commonly adopted to minimise the AC resistance R_{ac} [122]. The skin effect and proximity effect correction factors $\kappa_{ac}(f_s)$ are defined as the AC to DC resistance ratio as a function of the electrical frequency f_s [121, 122].

The main parts of the flux lines of the electromagnetic field generated in the stator cross the main air gap to link with the rotor structure. Due to the geometry and the material properties, part of the flux lines, especially around the slot opening area, do not cross the air gap but they close around the stator structure itself. The electromagnetic energy associated with these flux tubes results in a leakage flux, which is required to be balanced with the total input reactive power, Q_E. The reactive power that crosses the main air gap can be computed as $Q_g = Q_E - Q_{E,s}$. According to Gauss's theorem it is possible to find the relation of the average apparent power $\hat{W} = P + \jmath Q$ flowing inwards or outwards in a given closed volume $\mathcal{V}$ as presented in (2.33). The *Poynting* theorem when applied to the computational domain computes the active and reactive power of the region and therefore determines the flow between the domains. The integration surface $\partial\mathcal{V}$ is considered to be the boundary that defines the volume $\mathcal{V}$. The computation of the total power crossing the computation surface can be calculated and using *Stokes* theorem [104] the *Poynting* theorem can be written as

$$\hat{W} = -\iiint\limits_{\mathcal{V}} \nabla \cdot \vec{\mathbf{S}}\, dv = -\oiint\limits_{\partial\mathcal{V}} \vec{\mathbf{S}} \cdot d\vec{A} \tag{2.33}$$

having $\vec{\mathbf{S}} = \vec{\mathbf{E}} \times \vec{\mathbf{H}}$ as the *Poynting* vector and $d\vec{A}$ is the unitary surface of integration. The bi-dimensional field approximation in combination with *Maxwell's* equations can simplify the power calculations. Levering on the harmonic decomposition, the complex number representative of the time averaged volumetric apparent power density associated to each couple of time-space harmonics can be computed as

$$^{\nu\varsigma}\hat{\vec{\mathbf{S}}} = \frac{1}{2}\left\{ {}^{\nu\varsigma}\hat{\vec{\mathbf{E}}} \times {}^{\nu\varsigma}\hat{\vec{\mathbf{H}}}^{*} \right\} \tag{2.34}$$

The total power which enters the main air gap can be computed by applying (2.33) to the layered model proposed in Figure 2.7. The equivalent current sheet is considered and applying the boundary condition (2.29) [123], the apparent power results as

$$\hat{W}_g = -\jmath\, \pi\, r_S\, \ell_A \left\{ \sum_{\nu\in\mathbb{Z}} \sum_{\varsigma\in\mathbb{Z}} \nu\, \omega_e\ {}^{\nu\varsigma}\hat{A}_{g,z}(r_S)\ {}^{\nu\varsigma}\hat{J}^{*}_{S,z} \right\} \tag{2.35}$$

The main air gap is defined as the physical clearance between the stator and the rotating structure, it is filled with a medium (generally air). The air gap region is the location of the device where most of the magnetic energy is stored. The reactive power balance is defined according to Figure 2.9 as $Q_r = Q_g - Q_{E,g}$ where $Q_{E,g}$ is related to the magnetising inductance conventionally defined in IMs. The active power balance for the air gap region results in $P_r = P_g - P_{L-M,g}$ where $P_{L-M,g}$ are the air gap power losses. The impact of the motion of the rotor on the fluid generates fluid flow in the region. The geometry and the rotational speed affect the type of fluid movement and consequently the power losses developed. Empiric and experimental formulation of the windage losses can be found in literature. However, the air gap region is immersed in the electromagnetic field and the flux tubes which cross find their closure path in the rotor region. The description of the phenomena which occurs in the air gap is important. The filtering effect of the clearance enables a reduction in the high space harmonic components entering the rotor structure and associated generated losses. The losses that are generated by air friction, bearing losses, and additional stray losses are not included in this section. The power calculation performed on the surface in the air gap is defined at the radius r_S^- close to the stator inner bore, which enables the computation of the input power in the air gap. If the surface in the main air gap defined by r_R^+ (infinitesimally bigger than the rotor outer bore radius) is considered, the filter effect of the air gap clearance is accounted for. The total complex power therefore results as

$$\hat{W}_r^+ = \jmath \frac{\pi\, r_R^+ \,\ell_A}{\mu_g} \omega_e \left\{ \sum_{\nu\in\mathbb{Z}} \sum_{\varsigma\in\mathbb{Z}} \nu \; {}^{\nu\varsigma}\hat{A}_{g,z}(r_R^+) \frac{\partial \, {}^{\nu\varsigma}\hat{A}^*_{g,z}(r)}{\partial\, r} \Big|_{r=r_R^+} \right\} \tag{2.36}$$

Including the tensor notation and according to Gauss's theorem, the volumetric force density results in $\vec{\mathbf{f}} = \nabla \cdot \underline{\underline{\mathbb{T}}}$ [100]. The total force $\vec{\mathbf{F}}$ is computed as the integral of the *Maxwell Stress Tensor* (MST) over the border of the volume that defines the moving body. According to Gauss's theorem, in combination with (2.38), the vector of the force $\vec{\mathbf{F}}$ is expressed as

$$\vec{\mathbf{F}} = \iiint_{\mathcal{V}} \vec{\mathbf{f}}\, dv = \iiint_{\mathcal{V}} \nabla \cdot \underline{\underline{\mathbb{T}}}\, dv = \oint\!\!\oint_{\partial\mathcal{V}} \underline{\underline{\mathbb{T}}} \cdot \hat{\mathbf{e}}_{\mathbf{n}}\, dS \tag{2.37}$$

where $\hat{\mathbf{e}}_{\mathbf{n}}$ is the unit vector normal to the surface $\partial\mathcal{V}$ of integration. The MST $\underline{\underline{\mathbb{T}}}$ is introduced and its components (independent from the coordinate system considered) are defined as (2.38) [100, 104]

$${}^{\nu\varsigma}\mathbb{T}_{g,(i,k)} = \mu_g \; {}^{\nu\varsigma}H_{g,i} \; {}^{\nu\varsigma}H_{g,k} - \frac{\mu_g}{2}\, \delta_{i,k} \sum_n {}^{\nu\varsigma}H^2_{g,n} \tag{2.38}$$

where $\delta_{i,k}$ is the *Kronecker delta* [1] with i, k spanning the coordinates considered. According to the definition of the *Moment* of the force $\vec{\mathbf{F}}$ on a generic

[1] $\delta_{i,k} = \begin{cases} 1 & \text{if } i = k \\ 0 & \text{if } i \neq k \end{cases}$

point defined by the position vector $\vec{\mathbf{r}}$, it is possible to write the torque acting on the rotor as $\vec{\mathbf{T}} = \vec{\mathbf{r}} \times \vec{\mathbf{F}}$. The mechanical output power is computed as $P_M = \vec{\boldsymbol{\Omega}} \cdot (\vec{\mathbf{r}} \times \vec{\mathbf{F}})$. It is important to note that the output torque calculations can be performed at different radii and a particular generic integration path in the main air gap (the mid-air gap surface defined by r_g is mostly adopted [124]) can be defined to improve the accuracy of the computation [125, 126]. According to (2.10) the rotor reference frame's angular speed can be written as $p\,\omega_m = \omega_e(1-s)$ and the time averaged mechanical power is written as (2.39) with the complex term being derived by (2.38).

$$P_M = -\frac{\pi\, r_R^+\, \ell_A}{\mu_g}\, \omega_e\, \Im \left\{ \sum_{\nu \in \mathbb{Z}} \sum_{\varsigma \in \mathbb{Z}} \varsigma\,(1-s)\ {}^{\nu\varsigma}\hat{A}_{g,z}(r_R^+)\, \frac{\partial\, {}^{\nu\varsigma}\hat{A}^*_{g,z}(r)}{\partial\, r}\bigg|_{r=r_R^+} \right\} \tag{2.39}$$

The power balance of the system computed at the air gap therefore defines the reactive power $Q_g = \Im\{\hat{W}_g\}$ and the electromagnetic losses $P_{E,L} = \Re\{\hat{W}_g\} - P_M$ which can be written in the compact form as

$$P_{E,L} = \frac{\pi\, r_R^+\, \ell_A}{\mu_g}\, \omega_e\, \Im \left\{ \sum_{\nu \in \mathbb{Z}} \sum_{\varsigma \in \mathbb{Z}} {}^{\nu\varsigma}s\ {}^{\nu\varsigma}\hat{A}_{g,z}(r_R^+)\, \frac{\partial\, {}^{\nu\varsigma}\hat{A}^*_{g,z}(r)}{\partial\, r}\bigg|_{r=r_R^+} \right\} \tag{2.40}$$

which includes the rotor iron hysteresis and eddy current loss components. The integration (2.33) can be performed considering the surface, $\partial\mathcal{V}_r$ entirely surrounding only the rotating element with a radius r_R^-. The total complex power can be therefore computed similarly to (2.36)

$$\hat{W}_r^- = \jmath\, \pi\, r_R^-\, \ell_A\, \omega_e \left\{ \sum_{\nu \in \mathbb{Z}} \sum_{\varsigma \in \mathbb{Z}} \frac{\nu}{\hat{\mu}_R^*}\ {}^{\nu\varsigma}\hat{A}'_{z,r}(r_R^-)\, \frac{\partial\, {}^{\nu\varsigma}\hat{A}'^*_{r,z}(r)}{\partial\, r}\bigg|_{r=r_R^-} \right\} \tag{2.41}$$

The rotor component as well as the integration surface move in a relative motion with respect to the stator and therefore it needs to be included in (2.33) when it is applied to the rotor domain [127]. The total power computed results are identical but the direct separation of the rotor loss components and the mechanical power is possible. The total volumetric rotor power density can be expressed as $\vec{\mathbf{J}} = \sigma\,(\vec{\mathbf{E}} + \vec{\mathbf{E}}_i)$ with $\vec{\mathbf{E}}_i = \vec{\mathbf{v}} \times \vec{\mathbf{B}}$. After some mathematical elaboration, the rotor volumetric power density results in

$$\nabla \cdot \vec{\mathbf{S}}_r = \hat{\mu}_r\, \vec{\mathbf{H}}_r \cdot \frac{\partial\, \vec{\mathbf{H}}_r}{\partial\, t} + \rho_R\, \vec{\mathbf{J}}_r \cdot \vec{\mathbf{J}}_r - \vec{\boldsymbol{\Omega}}_m \cdot (\vec{\mathbf{r}} \times \vec{\mathbf{f}}_r) \tag{2.42}$$

Poynting's theorem expressed as (2.42) distinguishes between the rotor losses and the mechanical output power whilst still featuring a total power equivalent to what is computed using $\partial\mathcal{V}_r$. The first element of the equation in (2.42) represents the energy stored in the magnetic field. The volumetric power losses in the rotor are accounted for in the second term. Combining (2.20) and (2.25) with *Maxwell's* equations and the equation for the material, the power loss density in the rotor layer h [90] is expressed as the volume integral form of (2.42), $P'_{L,J} = \iiint_{\mathcal{V}_r} \rho_R \, \vec{\mathbf{J}}_r \cdot \vec{\mathbf{J}}_r \, d\mathcal{V}$. According to the bi-dimensional approximation and harmonic decomposition, the total eddy current power losses result in

$$P_{L-E,J-r} = \pi \, \ell_A \, \Re \left\{ \sum_{\nu \in \mathbb{Z}} \sum_{\varsigma \in \mathbb{Z}} \frac{{}^{\nu\varsigma}\omega^2}{\rho_R} \int_{r_I}^{r_R} {}^{\nu\varsigma}\hat{A}'_{r,z}(r) \; {}^{\nu\varsigma}\hat{A}'^{*}_{r,z}(r) \, r \, dr \right\} \tag{2.43}$$

where ρ_R has to be considered as a function of the rotor's operative temperature. The temperature correction coefficient $\kappa_{\tau,R}(T_R) = 1 + \alpha_R \, [T_R - T_{R,0}]$ is defined and the rotor resistivity results as $\rho_R = \rho_{R,T_{R,0}} \, \kappa_{\tau,R}(T_R)$.

The latter term of (2.42) represents the mechanical output power (see (2.37)). The rotor iron losses can therefore be calculated with (2.42) as $P_{L-E,fe-r} = \Re\{\hat{W}_r\} - P_M - P_{L-E,J-r}$ thanks to the inclusion of the complex permeability. The MST can also be applied for the rotor integration surface and the results are identical to the those computed in the main air gap. Considering the DDM introduced in the above section, the power calculations (2.41), (2.43) and the MST (2.37)-(2.38) can be applied to each individual layer, which details the loss distribution and the impact on the output torque of each layer.

2.1.9 Air gap fluid-friction Losses

The fluid that fills the clearance between the rotor and stator structure is forced into motion while the rotating elements are revolving. This motion is a source of losses which become important in high speed applications. Different empirical formulae can model the fluid-friction losses. The model proposed in [59] shows good agreement between the measured and predicted fluid-friction losses and also accounts for the end region effects. The friction losses are analytically computed according to [59,128,129]. The impact of the the narrow air gap region on the total windage losses is estimated with (2.44a) while the end-region contributions are given by (2.44b).

$$
{}^{g}P_{M-g} = \frac{1}{2}\,\kappa_{surf}\,C_f\,\pi\,\rho_{d,g}\,\ell_a\,r_R^4\,\omega_m^3 \tag{2.44a}
$$

$$
{}^{er}P_{M-g} = \frac{1}{2}\,\kappa_{surf}\,C_{f,er}\,\rho_{d,g}\,\left(r_{er,o}^5 - r_{er,i}^5\right)\,\omega_m^3 \tag{2.44b}
$$

where κ_{surf} is the surface roughness coefficient ($\kappa_{surf} = 1$ for concentric cylindrical structure), $\omega_m\,[{}^{rad}/_{sec}]$ is the rotor angular speed, $\rho_{d,g}\,[{}^{kg}/_{m^3}]$ is the mass density of the fluid in the air gap, $\ell_a\,[m]$ is the active stack length of the machine, $r_R\,[m]$ is the rotor outer radius, $r_{er,i}\,[m]$, $r_{er,o}\,[m]$ are the inner and outer radius of the end region disk, respectively. The dependency of the air gap fluid density with respect to the temperature T_g can be included in the model $\rho_{d,g}(T_g)$. C_f and $C_{f,er}$ are the friction coefficients for the narrow air gap region and the end-region, respectively. The latter strongly depends on the fluid flow regime determined by the *Taylor* (Ta) [92] and *Raynold* numbers (Re_δ and Re_r for the narrow air gap and end region, respectively) [59] which are functions of the air gap thickness, end region axial length and rotor angular speed. Analytical-empirical expressions for the friction coefficient and Ta number can be found in [59, 92, 128, 130] and below.

$$
C_f = \begin{cases}
\left(\dfrac{\varepsilon_g}{r_R}\right)^{0.3} \dfrac{0.625}{Re_\delta} & \text{if } Re_\delta \leq 64 \\
\left(\dfrac{\varepsilon_g}{r_R}\right)^{0.3} \dfrac{0.125}{Re_\delta^{0.6}} & \text{if } 64 < Re_\delta < 500 \\
\left(\dfrac{\varepsilon_g}{r_R}\right)^{0.3} \dfrac{0.0644}{Re_\delta^{0.5}} & \text{if } 500 < Re_\delta < 10^4 \\
\left(\dfrac{\varepsilon_g}{r_R}\right)^{0.3} \dfrac{0.0041}{Re_\delta^{0.2}} & \text{if } Re_\delta > 10^4
\end{cases} \tag{2.45}
$$

$$
C_{f,er} = \begin{cases}
\left(\dfrac{\ell_{cr}}{r_{st}}\right)^{0.1} \dfrac{3.7}{Re_r^{0.5}} & \text{if } Re_r < 3\cdot 10^5 \\
\left(\dfrac{\ell_{cr}}{r_{st}}\right)^{0.1} \dfrac{0.0102}{Re_r^{0.2}} & \text{if } Re_r > 3\cdot 10^5
\end{cases} \tag{2.46}
$$

where ℓ_{cr} is the axial distance between the rotor end and the housing while r_{st} is the outer bore radius of the rotor shaft.

2.1.10 The Rotor End-Region Coefficient

The impact of the rotor over-length on the electromagnetic performance of SRIMs is an important topic of current research. Different approaches have been proposed to account for the rotor region that extends over the stator's axial length when approaching the analysis of SRIM in the bi-dimensional domain. In Table 2.1 a summary of the end-region coefficients that can be found in literature is reported. The correction factor is a function of the geometry of the end region and is independent on the magnetic load and other aspects such as temperature and operative slip [131]. However, in [132], a modified version of the *Russell-Norsworthy* coefficient is presented as a function of the operative fundamental slip of the machine $\kappa_{er}(s)$; in [133], the *Fu* end region factor is proposed as a function of the rotor field frequency. The end-region coefficient in complex form $\hat{\kappa}_{er} \in \mathbb{C}$ has been proposed [134] as a correction factor for the rotor conductivity in order to account for the effect of the rotor end region also on the reactive power of the machine. The correction factor are developed mainly focusing in a good agreement of the measured or computed with three-dimensional FEA machine performances and losses distributions.

The correction factor impacts on both the rotor power losses and power factor [134]. According to the power analysis previously presented, the rotor eddy current losses are computed as (2.43). FEA can be used to compute the end-region coefficient [97,131] in order to account for the end region's active power losses in the computation. However, the end region impacts not only the active power but also the reactive component [134] resulting in the complex correction factor $\hat{\kappa}_{er}'$ being defined. The latter has to be considered as a function of the operative slip, load current, temperature distribution but only some of these parameters are important for the calculation.

Table 2.1: Literature end-region factors κ_{er}

Name	Factor	Ref.
	Smooth Solid Rotor	
Russell-Norsworthy	$\kappa_{er} = 1 - \frac{2}{\ell_r} \left(\frac{\tau_p}{\pi}\right) \frac{\tanh\left[\left(\frac{\pi}{\tau_p}\right)\frac{\ell_r}{2}\right]}{1+\tanh\left[\left(\frac{\pi}{\tau_p}\right)\frac{\ell_r}{2}\right]}$	[135]
Gibbs	$\kappa_{er} = 1 + \frac{2}{\pi}\frac{\tau_p}{\ell_r}$	[136]
O'Kelly	$\kappa_{er} = 1 + \frac{\tau_p}{\ell_r}$	[108]
Yee	$\kappa_{er} = \frac{(\pi/\tau_p)\ \ell_r \left(1+\coth\left[\left(\frac{\pi}{\tau_p}\right)\frac{\ell_r}{2}\right]\right)}{(\pi/\tau_p)\ \ell_r \left(1+\coth\left[\left(\frac{\pi}{\tau_p}\right)\frac{\ell_r}{2}\right]\right) - 2}$	[137]
Fu	$\kappa_{er} = \left(1+\frac{\tau_p}{\ell_r}\right)\left[\frac{\varrho^2\,\varepsilon_g + \frac{1}{(\mu_r\,\Delta)}}{\lambda^2\,\varepsilon_g + \frac{1}{(\mu_r\,\Delta)}}\right]$	[133]
Aho	$\kappa_{er}(s) = \kappa_{er}\left(\frac{\omega_{asyn}}{\omega_{syn}}\right)^4$	[132]
	Coated Solid Rotor	
Gieras	$\kappa_{er}(f_t) : \ f_t = 1 + \frac{1.2\ (t_{ov} - d_{Cu})}{d_{Cu}}$	[26]

$\ell_r[m]$: axial length; $D_r[m]$: rotor outer diameter; $\tau_p[m] = D_r\,\pi/\mathcal{P}$: pole pitch; $\varrho = \pi/\tau_p$; $\lambda = \varrho\sqrt{1+(\tau_p/\ell_r)^2}$; $\Delta = \sqrt{2\,\rho_R/(s\,\omega_e\,\mu_R)}$; $d_{Cu}[m]$: thickness copper coating; $t_{ov}[m]$: thickness over-length coating; $\omega_{ov}[m]$: rotor axial over-length.

The correction factor has been proposed to modify the rotor impedance found in the steady-state single phase equivalent circuit. The rotor impedance [26, 56, 119] can be expressed as (2.47), and directly computed according to the electromagnetic field distribution considering the bi-dimensional harmonic approximation.

$$^{\nu\varsigma}\hat{Z}_r' = \left.\frac{^{\nu\varsigma}\hat{E}_{r,z}(r)}{^{\nu\varsigma}\hat{H}_{r,\theta}(r)}\right|_{r=r_R} \tag{2.47}$$

Considering the formulation of the vector field with respect the magnetic vector potential and than substituting (2.47) in (2.41), the rotor complex power $^{\nu\varsigma}\hat{W}_r$ can be evaluated. Combining (2.47) and (2.49) the rotor impedance accounting for the end region effects results in $^{\nu\varsigma}\hat{Z}_{r,3D}' = {}^{\nu\varsigma}\hat{\kappa}_{er}\ {}^{\nu\varsigma}\hat{Z}_r'$.

The general equation for the rotor electric conductivity correction is expressed as (2.48) where $\beta = 1$ is proposed in [97,108,131,135] while $\beta = 2$ is in [26,133].

$$\sigma_R^{'} = \kappa_{er}^{\beta}\,\sigma_R \tag{2.48}$$

Considering (2.12) and (2.41), the generalised harmonic end region coefficient $^{\nu\varsigma}\hat{\kappa}_{er}$ can be defined.

$$^{\nu\varsigma}\hat{\kappa}_{er} = \frac{^{\nu\varsigma}\hat{W}_{r,3D}}{^{\nu\varsigma}\hat{W}_r} \tag{2.49}$$

The end-region effects are not negligible in SRIMs. Introducing high conductivity end rings could increase the electromagnetic performance with the consequence of reduced rotor robustness and decreased reliability. The manufacturing and assembly of end rings for high speed applications requires specialised techniques which are often expensive and result in complicated procedures [33].

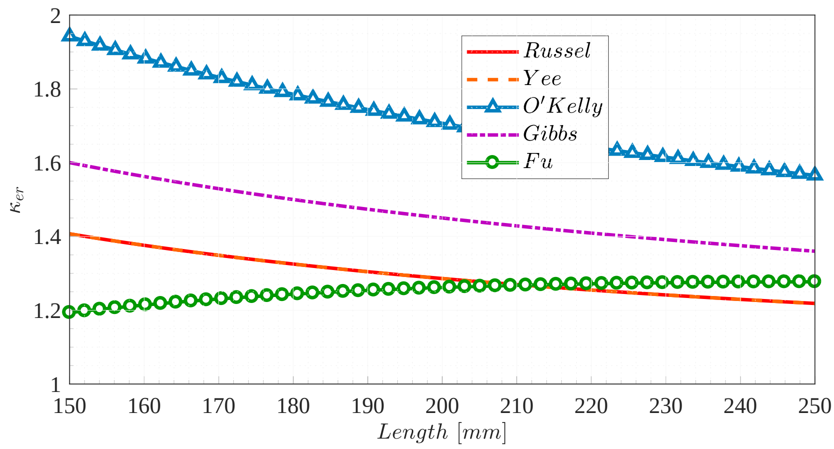

Figure 2.10: End-region effect comparison considering $r_R = 45\,[mm]$, $\varepsilon_g = 0.5\,[mm]$, $s = 1\,[\%]$, $\omega_m = 32\,[krpm]$, $\mu_{r,R} = 500$, $\rho_R = 40\,[\mu\Omega cm]$

The values of the end-region effects are quite different and feature a decreasing trend with respect to the rotor length. However, the *Fu* coefficient remains almost constant while varying the rotor end region length as presented in Figure 2.10. The loss minimisation and output torque maximisation are the main objectives in achieving high performance SRIM. The study of the end region effect as well as numerical analyses [138] have shown that the rotor axial length should be reduced to the minimum. As the field distribution in the bi-dimensional domain of analysis is strongly dependant on the resistivity correction factor, an accurate selection and characterisation of its dependency with respect the operative condition and rotor geometry are is required. Due to the high variation in the above mentioned parameters, full three-dimensional simulations are performed later in this work targeting the identification of the end region factor to be selected for the rotor topology considered and its variability with respect the rotor length and operative slip.

2.1.11 The Equivalent Circuit

The calculation of the electromagnetic field distribution in the rotor and main air gap enables the characterisation of the power losses and torque for different operative points. However, the behaviour of IMs and in particular SRIMs can be described with the single phase equivalent circuit approach presented in Figure 2.11. Since the presented circuit is valid only for steady state conditions, it is considered linear as the rotor lumped parameters are a function of the operative slip [26].

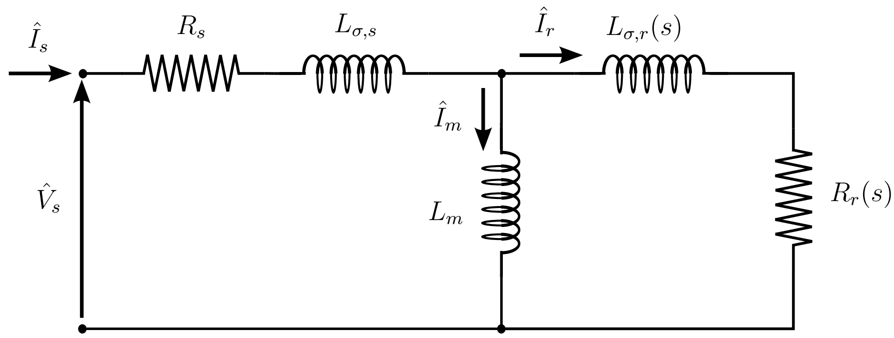

Figure 2.11: Linear single phase steady state equivalent circuit for smooth SRIM.

The lumped parameters of the equivalent circuit are required and can be estimated from the electromagnetic field distribution [26]. The power balance approach is proposed in [127] and [123] in order to evaluate the equivalent circuit parameters. The resistances are defined in order to account for the active power taking place while the inductance relate to the reactive power component. Moreover, due to the non-linearities, material properties and the field distribution, the equivalent circuit parameters have to be determined as a function of the operative conditions of the machine. The limitations of the analytical models become important when high saturation occurs in the ferromagnetic material. Furthermore, the non-linear dependency of the equivalent inductances and resistances against the load current have to be investigated by means of FEA. The prediction of the SRIM characteristic under the assumption of linear magnetic material is valid for high speed machines that are designed with reduced magnetic load in order to limit the iron losses.

In principle, it is possible to define an equivalent impedance for each layer that is in the model for the SRIM. According to [26,56], the impedance is computed as

$$^{\nu\varsigma}\hat{Z}_h' = \left.\frac{^{\nu\varsigma}\hat{E}_{h,z}(r)}{^{\nu\varsigma}\hat{H}_{h,\theta}(r)}\right|_{r=r_h} \tag{2.50}$$

However, since the input of the equivalent circuit is either a voltage, $^{\nu}\hat{V}_s$ or a current, $^{\nu}\hat{I}_s$ and related with the ν time harmonic component under investigation, the equivalent impedance $^{\nu}\hat{Z}_h'$ results in the combination of the space harmonic effect. The electromagnetic energy stored in the air gap is evaluated as the difference between the reactive component, which flows in the air gap and the components that enter the rotor structure. The above is directly related with the magnetising inductance of the machine that can be calculated. Furthermore, adopting the same principle, the impedance of a single layer is defined as the difference of the consecutive layer impedances.

2.2 Electromagnetic Model: Finite Element validation

The case study considered for the validation of the developed models consist of a SRIM featuring the stator structure presented in 1.7.1. The cage rotor is replaced with a solid rotor and the calculation of its performance is performed with different techniques while the stator structure is unchanged. The geometrical data and characteristics of the machine under investigation are listed in Table 1.2 and Table 2.2. The analytical-numerical model presented in Section 2.1 is compared with FEA.

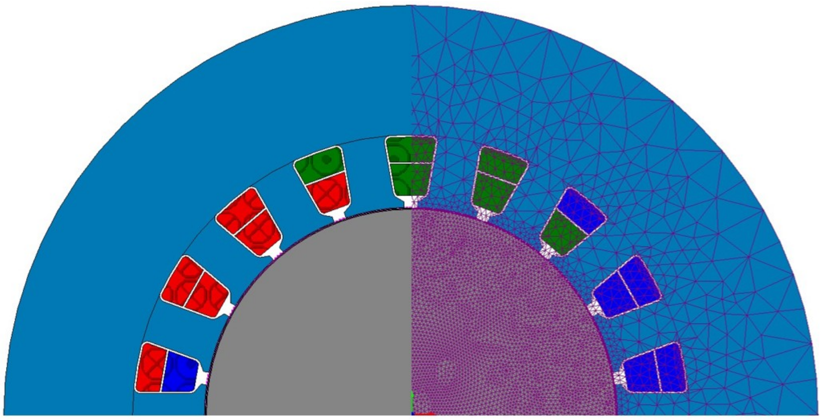

Figure 2.12: SRIM cross section FE

The SRIM is modelled in the FE environment and the cross section is presented in Figure 2.12 where the right side is the model solution mesh used, highlighting the required detailed mesh needed to achieve suitable accuracy in the field distribution calculation. The equivalent resistivity of the rotor structure is calculated according to (2.48) considering $\beta = 2$.

The analytical model is implemented in the Matlab® environment and run on a standard desktop PC, processor $i7 - 960$ @ 3.20GHz, 16GB RAM. The integration constants are computed for $\varsigma \in \{-43 \ldots 43\}$ assuming a sinusoidal current supply, $\nu = 1$. The robustness of the calculation is investigated [105]. Both the Cylindrical and Cartesian solution models are implemented and the matrix condition number is compared for different space harmonics and different slips.

Table 2.2: Machine Data

Parameter	**Symbol**	**Value**
Pole Pair	p	1
Rotor outer radius	$r_{r,o}$	$45[mm]$
Air gap thickness	ε_g	$0.6[mm]$
Stator outer radius	r_e	$85[mm]$
Slot opening width	$r_{s,o}$	$0.5[mm]$
Active (stator) axial length	ℓ_a	$150[mm]$
Rotor axial length	ℓ_r	$160[mm]$
Rotor Material Properties		
Electrical resistivity	ρ_R	$25[\mu\Omega cm]$
Relative magnetic permeability	$\mu_{R,r}$	500
Saturation flux density	$B_{R,s}$	$1.6[T]$
Rotor Temperature	T_R	$20[°C]$
Temperature coefficient	α_r	$6 \cdot 10^{-3}[1/°C]$

The results reported in Figure 2.13 present the condition number m_c of (2.28) computed for the entire slip range for the space harmonic order considered. The calculations highlight that the curvature effect for the harmonic $\varsigma = 1$ is negligible and both the Cylindrical and Cartesian model can accurately estimate the performances. However, the Cylindrical model accounts for the geometry curvature and is therefore preferred.

In Figure 2.14 the ratio of the condition matrix characteristic for the model is implemented with respect to the operative slip and the space harmonic order is detailed. Considering $\varsigma > 0$, the Cartesian model is characterised by a lower condition number and a more accurate field estimation is achieved by having $m_{c,CAR} < m_{c,CYL}$. The solution for $\varsigma < 0$ are more accurate for the Cylindrical model. Furthermore, the matrix condition number features a strong dependency upon the slip as it affects the values of the parameter ${}^{\nu\varsigma}\hat{\lambda}$ and consequently the values of the matrix ${}^{\nu\varsigma}\hat{\mathbf{M}}$. However, induction machines are designed to operate at low slip values and therefore the impact of the slip is limited. The model featuring the lowest m_c is used for the analysis presented.

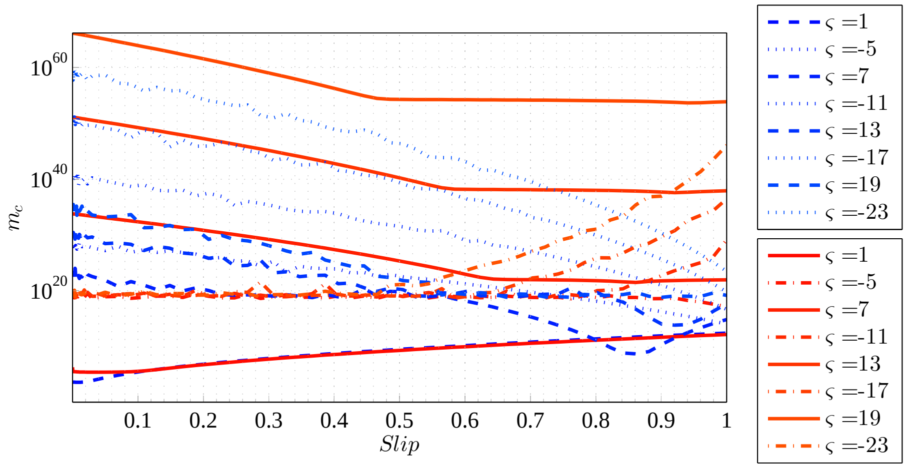

Figure 2.13: Condition number (m_c) against slip for the space harmonic index $\varsigma \in \{-25 \dots 25\}$ considering the Cylindrical (red) and Cartesian (blue) analytical models.

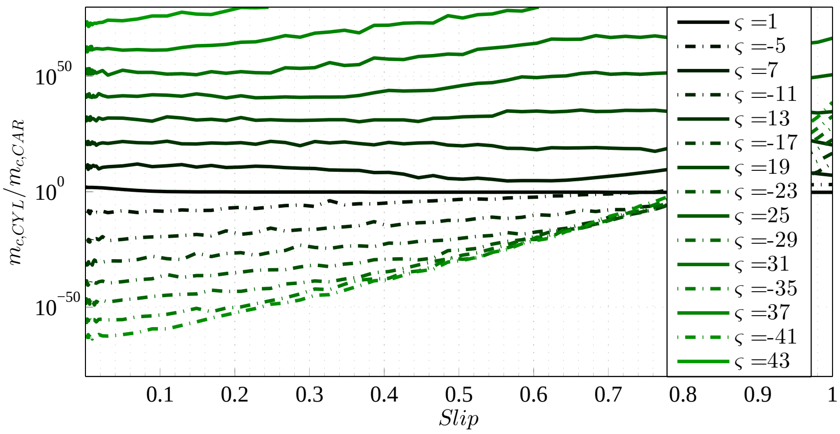

Figure 2.14: Condition number ratio between the Cylindrical $m_{c,CYL}$ and the Cartesian $m_{c,CAR}$ against slip for the space harmonic index $\varsigma \in \{-43 \dots 43\}$

The validation of the analytical-numerical predictions are performed by initially modelling a slot-less equivalent structure. Similarly to the analytical model, the air gap which surrounds the rotor structure is bounded by an equivalent current sheet.

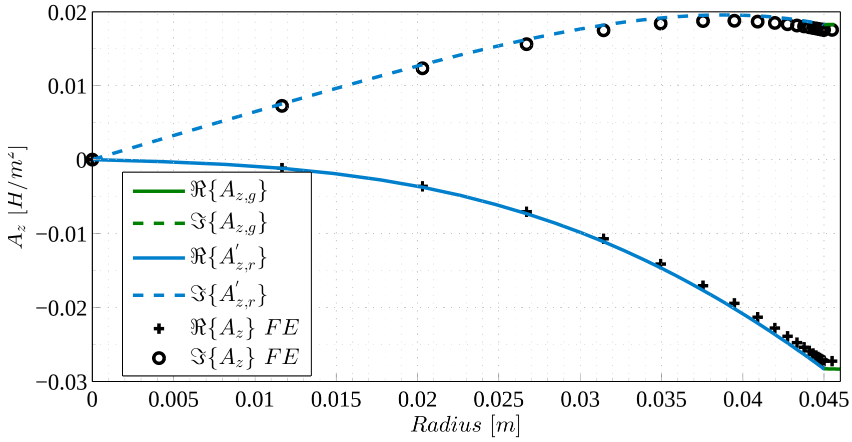

(a) Magnetic vector potential

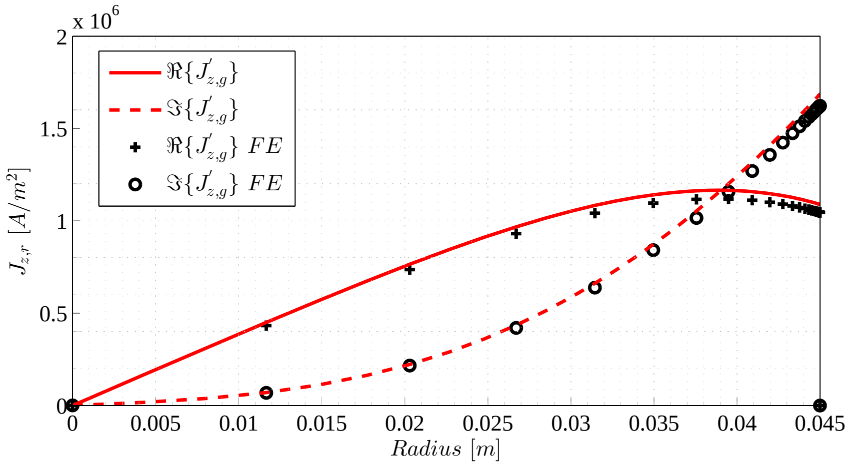

(b) Eddy current density

Figure 2.15: Comparison of analytical-numerical and FE computed real and imaginary part of electromagnetic field distribution. The solution is obtained considering $\nu = 1$, $\varsigma = 1$, $s = 0.8\,[\%]$, $I_s = 300\,[A]$, $\mu_{R,r} = 500$, $\sigma_R = 2.5\,[MS/m]$

The calculation of the machine performance is obtained by elaborating the magnetic vector potential distribution in the rotor and air gap. In Figure 2.15a, the field distribution solution of the analytical-numerical model is compared with the FE simulation results. The eddy current losses in the rotor are a critical aspect in SRIMs that lead to thermal management related issues and impacts the material properties. The rotor power losses are computed according to (2.43), which requires the eddy current density distribution in the rotating element.

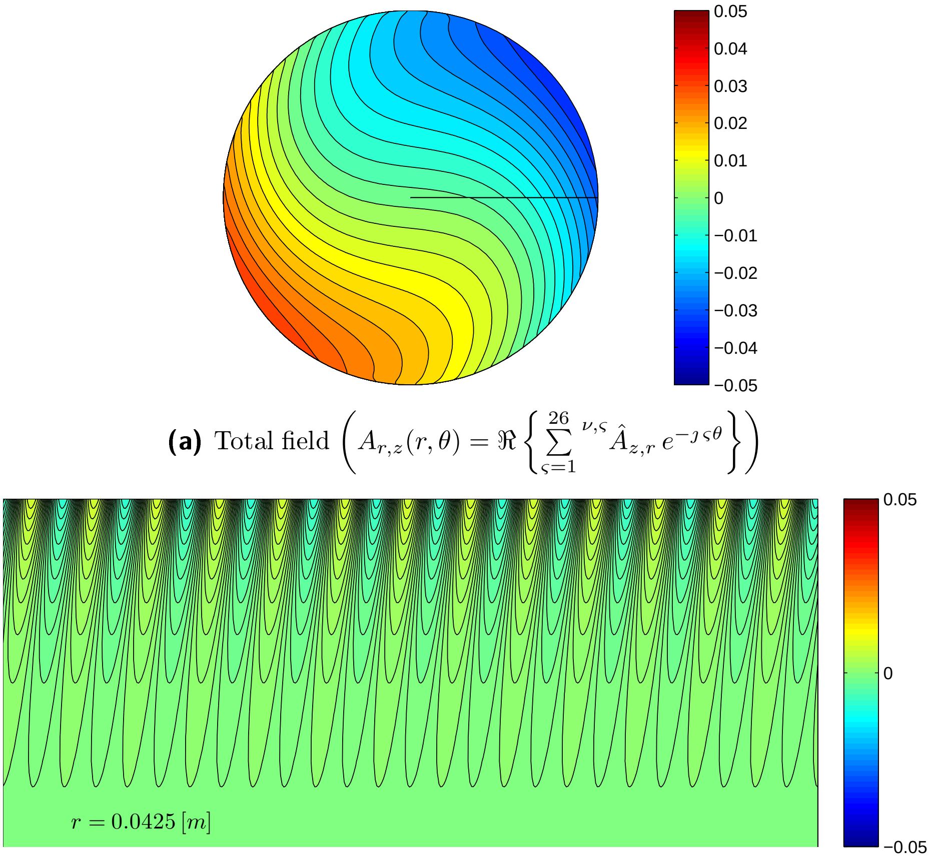

(a) Total field $\left(A_{r,z}(r,\theta) = \Re\left\{\sum_{\varsigma=1}^{26} {}^{\nu,\varsigma}\hat{A}_{z,r}\, e^{-\jmath\varsigma\theta}\right\}\right)$

(b) Harmonic field $\varsigma = 13$ $\left({}^{1,13}A_{r,z}(r,\theta)\right)$

Figure 2.16: Analytical calculation of magnetic vector potential field 2-D distribution. The solution is obtained considering $\nu = 1$, $s = 0.8\,[\%]$, $\omega_m = 32\,[krpm]$, $I_s = 300\,[A]$, $\mu_{R,r} = 500$, $\sigma_R = 2.5\,[MS/m]$

In order to validate the power losses calculation, the current density distributions are compared with the FE results in Figure 2.15b. According to the harmonic decomposition on which the analytical model is based, the effect of the space harmonics in the field distribution can be investigated separately.

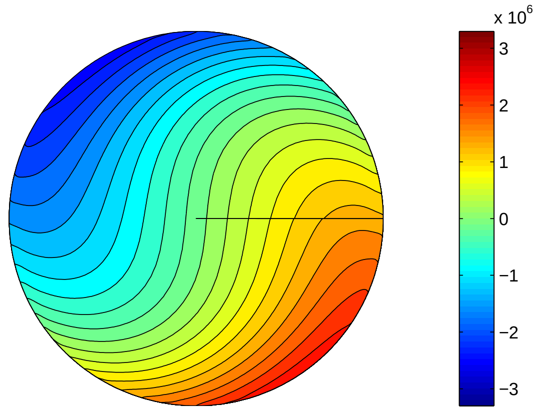

(a) Total field $\left(J_{r,z}(r,\theta) = \Re\left\{\sum_{\varsigma=1}^{43} {}^{\nu,\varsigma}\hat{A}_{r,z}\, e^{-\jmath\varsigma\theta}\right\}\right)$

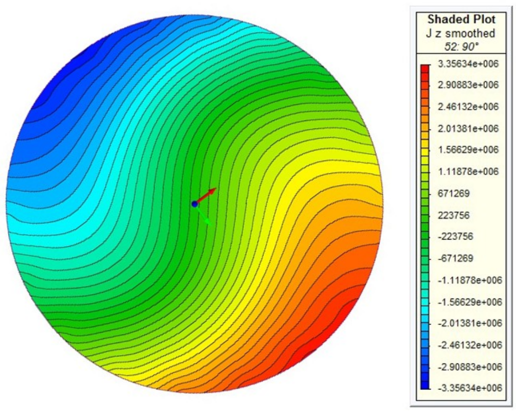

(b) Current density distribution calculated with Magnet® FEA software package

Figure 2.17: Current density field 2-D distribution. Comparison of analytical-numerical model and Magnet® FEA solution considering $s = 0.8\,[\%]$, $\omega_m = 32\,[krpm]$, $I_s = 300\,[A]$, $\mu_{R,r} = 500$, $\sigma_R = 2.5\,[MS/m]$

The high electrical frequency of the space harmonics leads the field distribution to focus in the outer part of the rotating element. In Figure 2.16a the total field distribution of the magnetic vector potential is presented and calculated as the sum of the harmonics up to $\varsigma = 43$; the single harmonic solution using the Cartesian model for $\varsigma = 13$ is proposed in Figure 2.16b in order to highlight the penetration depth effect. This effect leads to a significant current density distribution on the rotor surface which results in high power losses and a screening effect with respect to the magnetic field. The analytical idealised slot-less model results are compared with the FE analysis performed on a model which includes the stator structure. The current sheet is modelled to account for the harmonic effect that arises from the slot opening which characterises the stator's inner bore structure. In Figure 2.17 the total eddy current density distribution within the rotor calculated by means of the analytical model is compared with the FE solution. The good agreement in the field distribution validates the analytical prediction concerning the influence of the space harmonic.

The analytical model enables a quick assessment of the impact of the higher space-time harmonics on the overall performance. The resulting torque and losses can be separately computed. According to (2.38) and (2.43), the output torque and rotor power losses in the machine are computed for different operative slips. The effect of varying the frequency of the electromagnetic field in the rotating structure is calculated considering a span of operative slips. The discrepancies in the solutions presented in Figure 2.18 are a result of the poor matrix conditioning for the high space harmonic orders. Furthermore, the eddy current rotor losses computed with FE are compared with the analytical prediction. The air-friction losses $P_{L,W}$ and the stator winding joule losses $P_{L-J,S}$ are presented in Figure 2.19 together with the rotor losses.

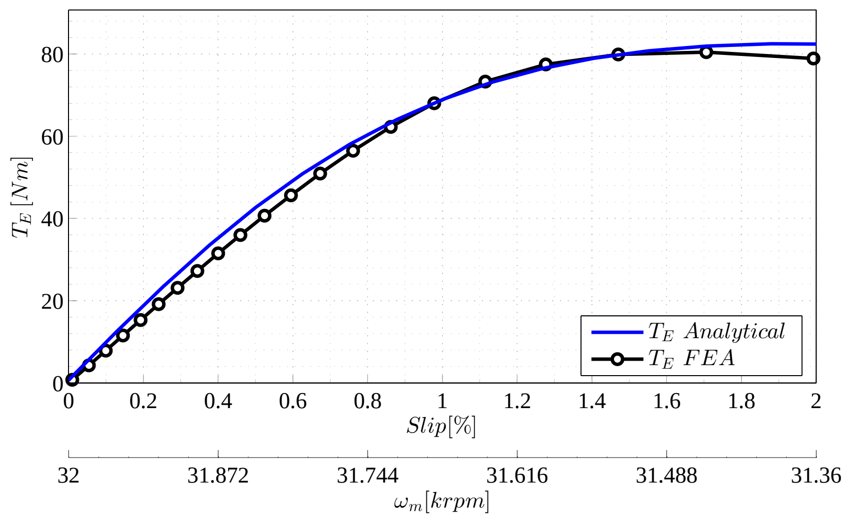

Figure 2.18: Comparison of linear analytical-numerical and linear FE computed torque against slip curve. The solution is obtained considering $\varsigma \in \{-43 \dots 43\}$, $I_s = 300\,[A]$, $\omega_m = 32\,[krpm]$, $\mu_{R,r} = 500$, $\sigma_r = 2.5\,[MS/m]$

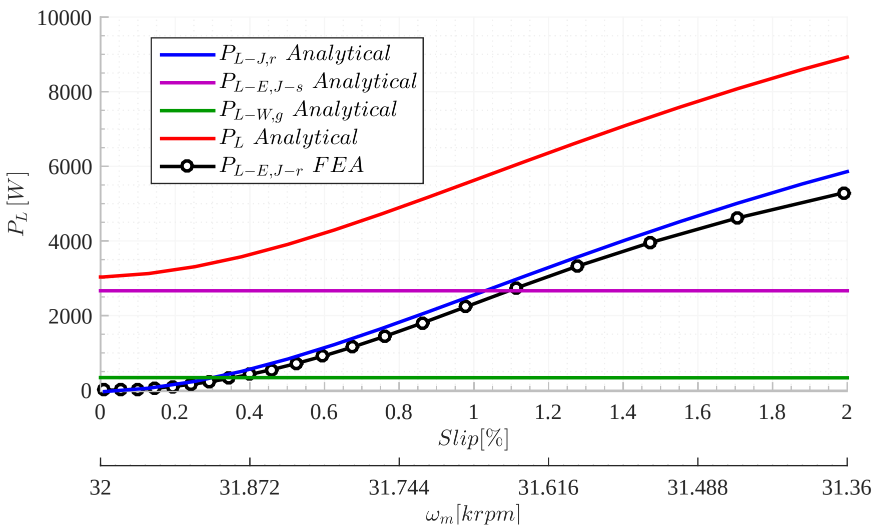

Figure 2.19: Comparison of linear analytical-numerical and linear FE computed power losses against slip. The solution is obtained considering $\varsigma \in \{-43 \dots 43\}$, $I_s = 300\,[A]$, $\omega_m = 32\,[krpm]$, $\mu_{R,r} = 500$, $\sigma_r = 2.5\,[MS/m]$

According to the considerations detailed in the previous sections concerning the three-dimensional field distribution, the electromagnetic torque considering the end-region effect coefficient is computed. The majority of the end region coefficients are independent with respect to the operative slip and therefore have a constant impact on the torque and loss characteristic of the machine.

2.3 Summary

The calculation of the field distribution in solid rotor induction machine is presented and the discrete domain model is proposed as a flexible and fast technique to account for variation in the rotor parameters and/or (shell-) composite structures. With respect to the bi/three dimensional FE methods, the analytical modelling has to be considered a fast method for performance calculation of SRIM. However, the accuracy of the predictions are strongly affected by the parameters selected for the rotor material relative permeability, including the complex part, and rotor resistivity. The end region correction factor amplifies the losses and scales the overall performance of the machine. Thus, the numerical-analytical model requires a fine tuning with FE and/or experimental results to be effective. The equivalent circuit is often used as an alternative technique for the computation of induction machine output power and losses. The equivalent circuit parameters, estimated by means of the numerical-analytical method presented, are affected by the same uncertainty of the direct power and losses calculation performed by means of the electromagnetic field distribution. However, the equivalent circuit parameters can be estimated by means of a sample of FE simulation and the non linear circuit can be solved to achieve the output performance of the device as further described later in the document.

CHAPTER

THREE

THE MULTI-PHYSICS MODEL

The multi-physics approach for solving engineering problems is gaining popularity in industrial and academic environments as a powerful tool that determines the interaction between phenomena that occur in systems. The issues related with increasing the rotational speed in electrical machines, as highlighted in Chapter 1, require the assessment of the impact that the temperature distributions have on the electromagnetic performance and mechanical integrity of the machine. The material properties are strongly affected by the condition (mechanical stress, temperature, magnetic field strength) that they are operated at, and directly impact on the field distribution as well on the resulting losses. Furthermore, the mechanical properties of the material limit the operative speed of the machine according to the stress distribution that occurs. Finally, the high rotational speed requires particular attention to the rotor dynamic attributes at the design stage to guarantee safe operative conditions and to account for the vibrations that the device has to withstand during operation.

Using multi-physics modelling in electrical machine design is becoming the state of the art procedure to enhance the performances and reduce the device weight/size. FEA targeting the multi-physics analysis of complex systems are commercially available. However, the computational effort required to implement the model and achieve solutions make this approach impractical at the design stage. A mid-complexity solution is presented as a trade-off between computational effort and accuracy, that makes it suitable for the design stage and analysis. The multi-physics modelling of SRIM proposed aims to provide a flexible and powerful tool to determine the electromagnetic, thermal, mechanical, and rotor dynamic parameters for design or analysis purposes.

The domain description and modelling is based on assumptions that enable accounting for the main phenomena. The governing equations for the vector potential, temperature, mechanical stress distribution and rotor dynamic response are defined and solved for an homogeneous structure. The computational domain is therefore discretised in order to consider variation of the material properties, provide detailed loss distributions, and to enable the modelling of multi-layer solid rotor structure (i.e. coated solid rotor or shell-type multilayer topology). The solutions of the partial differential equations, the *Helmholtz* equation, *Fourier* equation, *Hook's* law, and the dynamic equation are for the electromagnetic, thermal, mechanical and rotor dynamic phenomena, respectively are computed in the device domain. The calculations concerning each physics are independently introduced and presented considering a SRIM which is schematically represented in Figure 2.1.

3.1 Thermal Model

Thermal management in high power density and high speed machines is critical in order to achieve safe operation and enhance the performance. High speed machines are sometimes limited by the capabilities of the cooling system to extract the heat losses generated in a very small volume. The stator losses (iron stator lamination eddy currents and hysteresis losses) as well as the copper losses are extracted by different cooling techniques. A high thermal conductivity path is embedded in the stator slots in order to enhance the thermal conductivity towards the stator heat sink [139]. Liquid cooling in an external jacket is widely used to increase the heat dissipation capabilities at the stator's outer bore [140, 141]. In the high power range, the loss density is mainly located in the stator conductors, therefore justifying direct cooling as the preferred cooling method. Semi-flooded structures have been investigated [84] in order to achieve a high thermal convection coefficient across the whole stator structure while the rotating components operate in a dry environment.

In SRIMs the stator losses are an important factor but the rotor losses can not be neglected. The analysis of the loss distribution and resulting temperature distribution is a critical aspect in high speed machines. The materials are required to operate within their temperature limitations and therefore efficient heat extraction has to be implemented. The latter results in an additional challenge in high speed machines as the tendency towards higher rotational speeds leads to a significant reduction in size and consequently higher power loss densities. The size reduction impacts the thermal dissipation capabilities because the cooling surface available for heat transfer is reduced. In SRIMs, the eddy current and hysteresis losses that are developed in the rotating element are higher than conventional IMs for the same power rating. Thermal management for SRIMs requires that heat extraction from the rotor is accounted for. In [59] a double stage stator is proposed in order to enhance the flow of cooling fluid in the main air gap and to enhance the rotor heat dissipation efficiency.

In order to account for the aforementioned aspects, the aim of this section is to investigate the effect of the rotor temperature on the SRIM performance and to provide a flexible tool for the temperature distribution calculation. In literature, the design of SRIMs mainly focuses on the electromagnetic parameters. In the previous section, the challenges in the computation of the performance of SRIMs are highlighted. The electromagnetic model presented enables the estimation of the rotor eddy current losses as well as the other main losses components. The rotor resistivity impact on the overall machine performance is clear considering (2.43) and following Section 2.1.10, where the correction coefficient is introduced to account for the end-region effect. The electric resistivity of the ferromagnetic materials can be in general expressed as a function of the temperature $\rho \rightarrow \rho(T)$. The resistivity of the rotor in SRIMs is therefore strongly linked with the rotor's operative temperature. The computation of the electromagnetic performance can be directly coupled with the calculation of the temperature distribution within the structure achieving a more realistic representation of the environmental condition [142].

The schematic representation of the SRIM is presented in Figure 2.1 where the radial and axial cross section are presented in Figure 2.1a and Figure 2.1b, respectively.

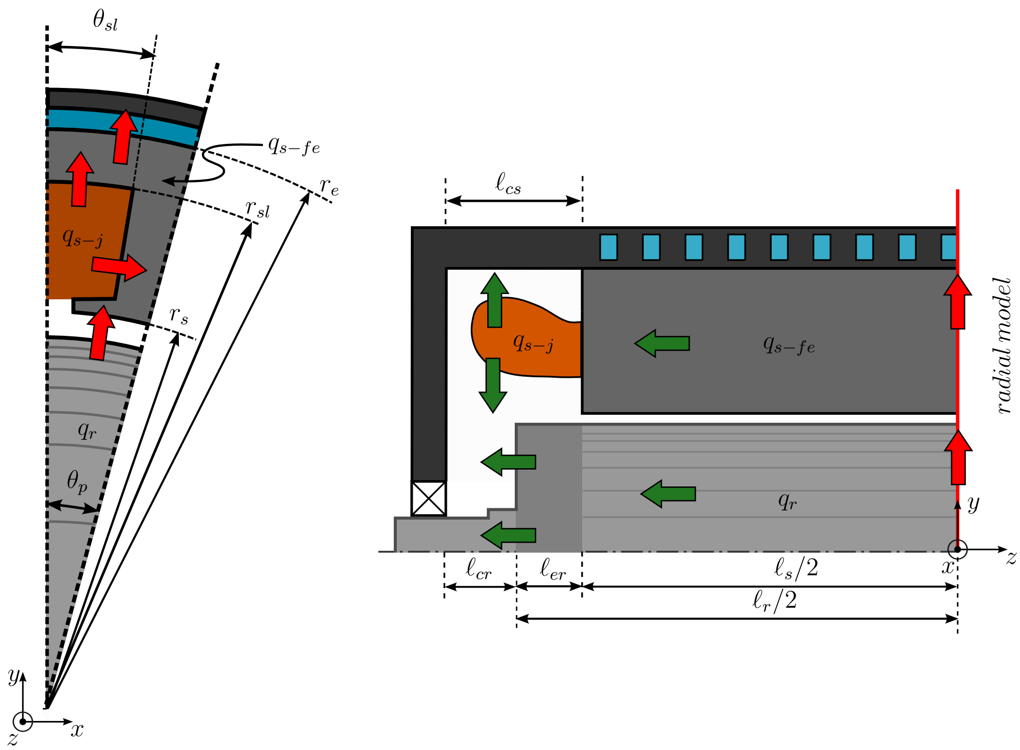

(a) $r - z$ axial model cross section

(b) $r - \theta$ half slot model cross section

Figure 3.1: SRIM schematic adopted for thermal modelling.

Taking advantage of the symmetries of the geometrical structure of the machine and the loss distribution, the thermal problem can be reduced. The symmetries in the tangential direction considering a generic radial cross section enable the machine model to be reduced to half a slot pitch, Figure 3.1a and the main radial heat flow are represented with red arrows; the axial development of the device identifies the drive end (DE) and non-drive end (NDE) which are identical and therefore half the structure length can be modelled, Figure 3.1b. The radial thermal model is located at the mid point of the axial length of the machine and a lumped parameter resistance network is designed to account for the axial heat flow highlighted by the green arrows. The rotor of a high-speed machine is usually cooled by the air gap flow. Furthermore, the winding and core losses in the stator are removed through the end windings and the external water jacket. In [59] the thermal network for high speed SRIMs is described in detail. The axial model used is based on the considerations found in [59, 143, 144]. In the following section, an alternative solution for the calculation of the temperature distribution in the cross section orthogonal to the axial development of the machine is proposed and coupled with the axial lumped network to achieve a full thermal model of the machine.

3.1.1 Rotor Thermal Model

The modelling of the heat transfer and temperature distribution phenomena in an isotropic media requires the consideration of *Fourier's* law (3.1).

$$\nabla^2\Theta({}^s\bar{p},t) + \frac{\dot{q}_G({}^s\bar{p},t)}{\kappa_{th}} = \frac{C_p}{\kappa_{th}}\frac{\partial\,\Theta({}^s\bar{p},t)}{\partial\, t} \tag{3.1}$$

where $\Theta({}^s\bar{p},t)$ is the temperature distribution function, κ_{th} is the *thermal conductivity* expressed in $[{}^{W}/_{(m\,K)}]$ and C_p is the *specific heat capacity* of the material expressed in $[{}^{J}/_{(kg\,K)}]$. The function $\dot{q}_G({}^s\bar{p},t)\,[{}^{W}/_{(m^3)}]$ defines the heat source's volumetric density in the media. The thermal properties of the media are considered to be constant in all the computational domains and independent of the temperature. The bi-dimensional approximation simplifies the problem without losing accuracy [96, 145]. Moreover, the symmetrical nature of the geometrical structure of SRIMs enables only the dependency of the temperature function Θ with respect to the radius ${}^sr$ and the time t to be considered. The PDE (3.1) can be further simplified considering the separation of the variable as $\Theta({}^sr,t) = T({}^sr)\,G(t)$. The space component of the steady-state temperature distribution function is therefore only the function of the radial coordinate and can be expressed as (3.2).

$$\frac{\partial^2 T(r)}{\partial r^2} + \frac{1}{r}\frac{\partial T(r)}{\partial r} + \frac{\dot{q}_G(r)}{\kappa_{th}} = 0 \tag{3.2}$$

The volumetric heat loss density $\dot{q}_G(r)$ results in the power losses computed as (2.43). The analytical solution of (3.2) for a generic loss distribution function is reported below.

$$T(r) = A + B\,ln(r) + \frac{1}{\kappa_{th}}\left[\int r\,ln(r)\,\dot{q}_j(r)\,dr - ln(r)\int r\,\dot{q}_G(r)\,dr\right] \tag{3.3}$$

The problem with the temperature distribution calculations considering a generic $\dot{q}_G(r)$ is usually solved via numerical methods such as Computation Fluid Dynamic simulations [146, 147], FEA [147] or Finite Difference Method (FDM) [148, 149]. The latter is selected as a compromise between accuracy, computational effort, and flexibility as it accounts for the stator structure. A consistent set of boundary conditions is required in order to compute the problem solution.

The FDM involves a discretisation of the computational domain in a series of disjointed sub-domain featuring a common boundary. The computational domain is divided into a discrete number of elements. Considering a node numbering system, the governing equation can be expressed as a linear combination of terms, relating the temperature of the neighbouring nodes to the temperature of the node of interest [143,148]. Considering the generic internal node defined by the pair (i, j), thermal resistances are defined to connect with the neighbouring nodes. Applying the principle of energy conservation, (3.2) can be expressed as

$$\frac{T_{i+1,j}}{{}^{\theta,j}\mathcal{R}_{i,i+1}} + \frac{T_{i-1,j}}{{}^{\theta,j}\mathcal{R}_{i-1,i}} + \frac{T_{i,j+1}}{{}^{r,i}\mathcal{R}_{j,j+1}} + \frac{T_{i,j-1}}{{}^{r,i}\mathcal{R}_{j-1,j}} - \frac{T_{i,j}}{\tilde{\mathcal{R}}_{i,j}} = -\dot{q}_{G,(i,j)} \tag{3.4}$$

The equivalent resistance related to the (i, j) node results as

$$\frac{1}{\tilde{\mathcal{R}}_{i,j}} = \frac{1}{{}^{\theta,j}\mathcal{R}_{i,i+1}} + \frac{1}{{}^{\theta,j}\mathcal{R}_{i-1,i}} + \frac{1}{{}^{r,i}\mathcal{R}_{j,j+1}} + \frac{1}{{}^{r,i}\mathcal{R}_{j-1,j}}$$

The thermal resistances for the conduction and convection heat flow are defined according to the discretisation defined for the computational domain and the thermal properties of the constitutive material [89, 148]. Defining the angular and radial increments between adjacent nodes according to the generic node scheme presented in Figure 3.2, the radial and tangential thermal resistances that define the conduction phenomena are calculated.

$$^{r,i}\mathcal{R}_{j,j+1} = \frac{ln\left(^{\tilde{r}_{j+1}}/_{\tilde{r}_j}\right)}{\kappa_j\,\delta z\,\delta\theta_i} \tag{3.5a}$$

$$^{\theta,j}\mathcal{R}_{i,i+1} = \tilde{r}_j\frac{\delta\theta_{i+1}}{\kappa_i\,\delta z\,\delta\,r_j} \tag{3.5b}$$

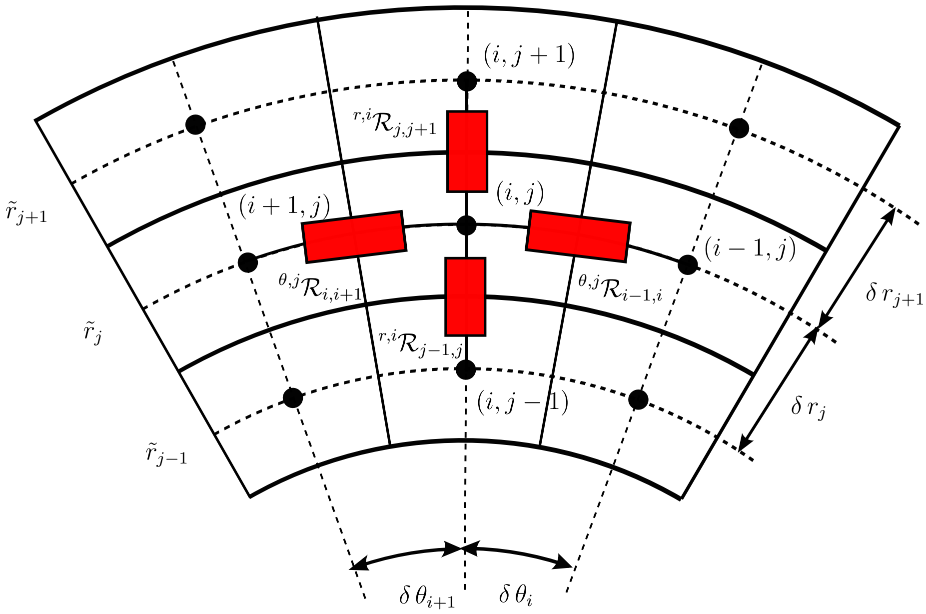

Figure 3.2: Schematic representation of adjacent node geometrical distribution.

A finite subset of nodes lay on the boundary of the computational domain. A consistent set of boundary conditions are applied in order to model the heat flow phenomena in a realistic form. Applying the *Neumann* boundary condition (constant heat flux) at the surface where the edge node (i, j) is located and considering the energy conservation principle, the boundary condition coefficient $D_{i,j}$ can be defined. The case of null heat flux imposed on the surface identified by the angular position θ_B define an adiabatic boundary condition.

$$\frac{\partial T}{\partial \theta}\Big|_{\theta_B} = 0 \Rightarrow D_{i,j} = 0 \tag{3.6}$$

Furthermore, the *Robin* boundary condition leads to the definition of the convection boundary condition coefficient $D_{i,j}$ for the edge node identified by r_B.

$$\frac{\partial T(r)}{\partial r}\Big|_{r_B} = h_B\Big(T(r_R) - T_\infty\Big) \Rightarrow D_{i,j} = -\left[\frac{T_\infty}{{}^{r,i}\mathcal{R}_{B,B+1}} + \dot{q}_{g,B}\right] \tag{3.7}$$

The heat in the rotor is mainly transmitted to the fluid in the air gap region by means of convection. According to Figure 2.7, the *Robin* boundary condition is applied on on the surface $\Gamma_{r/g}$ where ${}^{r/g}h_c$ is the air gap to rotor heat transfer coefficient and $T_{\infty,g}$ is the temperature of the air gap fluid. The temperature of the air gap fluid $T_{\infty,g}$ can be estimated and considered as a problem input or the effects of the physical clearance between rotor and stator are required to be modelled. However, part of the rotor heat is dissipated in the end region, transmitted through conduction in the shaft and the housing by means of the mechanical bearing. Axial thermal networks are often used to model the aforementioned aspects [59, 96, 143] and can be coupled with the presented cross section thermal model.

3.1.2 The Full Thermal Model

Thermal management in high speed electrical machines requires consideration of the rotor structure and its interaction with the stator and the dedicated cooling path designed. The air gap region and the stator structure can be discretised using a grid analogous to the one introduced for the rotor structure. The finite difference formulation defined in the generic node (i, j) of the rotor structure is valid for every node in the computational domain that does not belong to the structure's boundary. The coupling between the rotor and stator model is achieved by the main air gap. The convection heat transfer between the two structures is considered at the boundary surfaces of the rotor's outer bore and the stator's inner bore, where (3.7) is the $T_{\infty,g}$ becomes the unknown temperature of the adjacent air gap node. The adiabatic boundary condition

(3.6) is imposed at the nodes on the tangential edges of the sector, which defines the limits of the computational domain. The *Robin* boundary conditions (3.7) are imposed at the node on the outer bore of the stator structure considering the bulk temperature of the cooling fluid, T_w. Heat convection occurs between the stator's back iron and the water jacket in order to enhance the loss dissipation of the machine [30, 150].

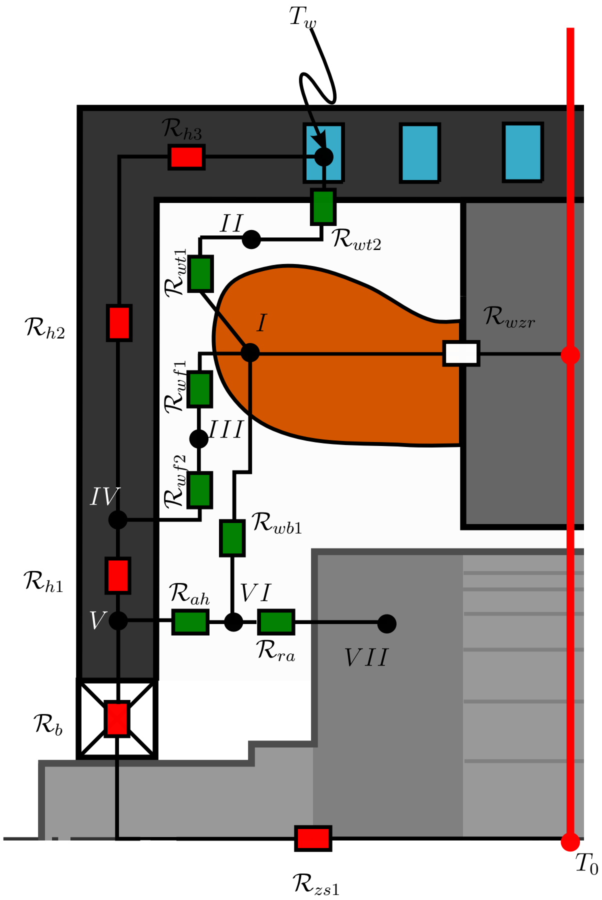

Figure 3.3: Axial thermal resistance network. The convection and convection thermal resistances are highlighted in red and green, respectively.

To account for the phenomena that occurs in the end regions of the machine, a simplified 7 node thermal resistance network is designed and presented in Figure 3.3. This figure is based on the geometrical arrangement in the end region depicted in Figure 1.19. The conduction through the rotor shaft and housing are modelled considering the geometry of the structure and assuming a homogeneous material. The convection thermal resistances connect air nodes, II, III, and VI to the structure. Empirical relations compute the heat transfer coefficients between the end winding, the middle and the top-end region (air). The heat transfer coefficient for the bottom end region air are strongly affected by the angular speed of the rotor [151]. The thermal resistance due to conduction for a volume in the end region where axial heat flow occurs is defined as

$$^{z}\mathcal{R} = \frac{\ell_n}{\kappa_n\, \delta\theta_n\, (r_{n,o}^2 - r_{n,i}^2)} \tag{3.8}$$

where ℓ_n is the axial development of the element, $\delta\theta_n$ is the tangential increment of the cross section, $r_{n,o}$ and $r_{n,i}$ are the outer and inner radius of the cross section, respectively. The resistance that defines the heat transfer due to convection is

$$^{z}\mathcal{R} = \frac{1}{^{n}h\, \delta\theta_n\, (r_{n,o}^2 - r_{n,i}^2)} \tag{3.9}$$

The coupling between the radial and axial thermal models are described in [143,144] where $\mathcal{R}_{wzr}$ is introduced to connect each node n of the winding stator structure to the node I representative of the end-winding connections [144].

Defining a single index node numbering system, a system of algebraic equations are achieved that can be represented in a matrix form by defining the matrix thermal conductances, $\mathbf{G}$ and the vector of the boundary conditions, $\bar{d}$. The temperature distribution in the nodes of the discretised domain can be computed with

$$\bar{T} = \mathbf{G}^{-1}\, \bar{d} \tag{3.10}$$

The volumetric power losses component $\dot{q}_{G,n}$ for a generic node, n have to be defined in order to determine $\bar{d}$. The stator winding losses, windage losses, and rotor losses are computed using the relations presented in Section 2.1.8. Constant loss volumetric density distributions, $^{sl}\dot{q}_{G,n}$ are considered in the winding structure and defined according to the discretised geometry considered

$$^{sl}\dot{q}_{G,n} = \frac{P_{E-J,s}}{n_E\, Q_s\, p\, \kappa_{fill}\, \mathcal{V}_{sl}} \tag{3.11}$$

where $\mathcal{V}_{sl}$ is the slot volume, n_E is the number of electrical phases, Q_s is the number of slot-pole-phases, κ_{fill} is the slot fill factor, and $P_{E-J,s}$ are the total *rms* copper losses in the stator copper windings. The windage losses are applied to the nodes in the air gap region and considered to be uniformly distributed.

$$ {}^{w}\dot{q}_{G,n} = \frac{P_{M,g}}{n_E\, Q_s\, p\, \mathcal{V}_g} \tag{3.12} $$

The volumetric loss density in the rotor structure is directly computed from the eddy current density distribution.

$$ {}^{r}\dot{q}_{G,n} = \sum_{\nu \mathbb{Z}} \sum_{\varsigma \mathbb{Z}} \rho'_{R,n} \frac{|{}^{\nu\varsigma}\hat{J}_{r,n}|^2}{2} \tag{3.13} $$

3.1.3 Heat Transfer Coefficient

The assessment of the thermal management capabilities of the system are very sensible considering the heat transfer coefficients in the analysis. The conduction heat transfer coefficient for the stator and rotor core, and air is selected according to the material properties [152]. Due to the non-homogeneous nature of the material in the slot, the equivalent conduction heat transfer in the stator winding region is computed according to [153].

$$ \kappa_{eq,Cu} = \frac{\kappa_{fill}\, \kappa_{Cu}}{\kappa_{fill}\, \kappa_{res} + \kappa_{Cu}\,(1 - \kappa_{fill})} \tag{3.14} $$

where κ_{fill} is the slot fill factor, κ_{Cu} is the thermal conductivity of the bare copper, and κ_{res} is the thermal conductivity of the resin. The conductivity heat transfer coefficients are considered temperature invariant and the values that characterise the case study machine are reported in Table 3.1.

Table 3.1: Convection Heat Transfer Coefficient

Region	**Symbol**	$\kappa\,[W/(m \cdot K)]$
Stator Core	κ_s	45
Rotor Core	κ_r	45
Resin	κ_{res}	0.2
Copper Winding	κ_{cu}	400
Aluminium (housing)	κ_{al}	200
Equivalent Copper Winding	$\kappa_{e,cu}$	0.65

The heat transfer convection coefficient implemented in the in the end region model results from the relations presented in [59, 96, 143, 151]. The calculation of the convection heat transfer coefficient for both the air gap region and water jacket are detailed in the following sections.

Water Jacket Heat Transfer Coefficient

The water jacket on the external periphery of the stator structure is considered to be the main heat extraction technique in use. In order to model the effect of the fluid flowing in the dedicated channels, the heat convection coefficient ${}^{w}h_c\,[W/(m\,K)]$ is required [151,154]. The *Reynolds* number for a channel with a hydraulic diameter of ${}^{w}D_h$ is defined as

$$Re_w = \frac{{}^{w}D_h\, v_w}{{}^{w}\mu} \tag{3.15}$$

where $v_w\,[{}^{m}/_{sec}]$ is the water velocity in the channel, and ${}^{w}\mu\,[{}^{m^2}/_{sec}]$ its kinematic viscosity. The hydraulic diameter of the rectangular channel where H_w and W_w are it's height and width, respectively, is defined as

$${}^{w}D_h = \frac{2\,W_w\,H_w}{W_w + H_w} \tag{3.16}$$

The convection heat transfer coefficient ${}^{w}h$ can therefore be described by (3.17) where ${}^{w}\kappa$ is the thermal conductivity of water and the *Nusselt* number is calculated according to (3.18) where $\gamma_w = 2\,(W_w + H_w)$ is the peripheral length of the channel where the cooling fluid flows.

$$ {}^{w}h_c = \frac{{}^{w}Nu \; {}^{w}\kappa}{{}^{w}D_h} \tag{3.17} $$

$$ {}^{w}Nu = 0.012 \, \left(Re_w^{0.87} - 280 \right) \, {}^{w}Pr^{0.4} \left[1 + \left(\frac{{}^{w}D_h}{\gamma_w} \right)^{\frac{2}{3}} \right] \tag{3.18} $$

The properties of water have to be considered as a function of the temperature. The *Prundtl* number, the kinematic viscosity, and the thermal conductivity represented as ${}^{w}Pr(T_w)$, ${}^{w}\mu(T_w)$, and ${}^{w}\kappa(T_w)$, respectively are expressed with polynomials obtained through curve fitting of the fluid characteristic.

Air gap Heat Transfer Coefficient

The estimation of the air gap heat convection coefficient has been the subject of many studies [91, 92]. The high rotational speed with respect to the fixed stator structure in electrical machines generates air flow in the main air gap. Taylor [92] showed that an a-dimensional number, Ta (Taylor number) can be defined to distinguish between the different flow regimes that can occur. Courette flow, turbulent, and turbulent flow with vortices regimes have been considered and subsequent studies proposed analytical models to calculate the heat transfer coefficient. The rotor radius, r_R and air gap thickness, ε_g impact the regime of the fluid in the clearance between the rotating and static machine components. Defining the geometrical factor, F_g [91] and the mean air gap radius, $r_m = r_R + \varepsilon_g/2$, Taylor [92] identified thresholds for the possible flow regimes. The correlation between the flow regime and the heat convection coefficient has been the topic of experiments and calculations for almost a century and various empirical relations have been found [155]. Considering a narrow gap and a stationary outer cylinder, the critical Taylor number that defines the limit of the Courette flow model in a small annuli is found to be $Ta_{m,cr} = 41.19 \, F_g$. With this the critical rotor radius can be evaluated using (3.19).

$$ r_{g,cr} = \left(\frac{Ta_{m,cr} \; {}^{g}\mu \, F_g}{\omega_m \, \varepsilon_g^{1.5}} \right)^2 - \frac{\varepsilon_g}{2} \tag{3.19} $$

According to *Taylor's* number theory, the heat convection coefficient can be estimated through the *Nusselt* number ${}^{g}Nu$ [91]. The thermal dissipation of the rotor losses depends on the convection thermal resistance of the air gap requiring the evaluation of the heat transfer coefficient, ${}^{r/g}h_c$, which is dependent on the Nu number. Various empirical relations between the ${}^{g}Nu$ number and the flow regime parameter, $\Lambda = Ta^2/F_g^2$ have been defined according to calculations and experimental data [155–157]. Having ${}^{g}\gamma = \varepsilon_g/r_m$, the thermal resistance of the air gap can be expressed as (3.20)

$$
{}^{r/g}h_c = \frac{{}^{g}\kappa\ {}^{g}Nu}{{}^{g}D_h} = \begin{cases} \dfrac{2\ {}^{g}\kappa\ {}^{g}\gamma}{{}^{g}D_h\, ln(1+{}^{g}\gamma)} & \text{if } \Lambda < 1700 \\[2ex] 0.064\, \dfrac{{}^{g}\kappa\, \Lambda^{0.367}}{{}^{g}D_h} & \text{if } 1700 < \Lambda < 10^4 \\[2ex] 0.2045\, \dfrac{{}^{g}\kappa\, \Lambda^{0.241}}{{}^{g}D_h} & \text{if } 10^4 < \Lambda < 10^7 \end{cases} \tag{3.20}
$$

where ${}^{g}D_h = 2\,\varepsilon_g$ is the hydraulic equivalent diameter, ${}^{g}\mu$ is the kinematic viscosity of the fluid [92], and ${}^{g}\kappa$ is the thermal conductivity. The properties of the air gap fluid have to be considered as a function of the temperature. The kinematic viscosity and the thermal conductivity, ${}^{g}\mu(T_g)$ and ${}^{g}\kappa(T_g)$, respectively, are expressed by polynomials obtained through curve fitting of the fluid characteristic.

3.1.4 Model Validation

The half slot discretised domain of the case study SRIM is calculated considering an exponential node distribution in the rotor characterised by ${}^{r}N_r = 100$ nodes. The number of radial nodes in the air gap, winding and back iron is selected as ${}^{r}N_g = 2$, ${}^{r}N_g = 12$ and ${}^{r}N_{bi} = 6$, respectively. The grid computed is presented in Figure 3.4.

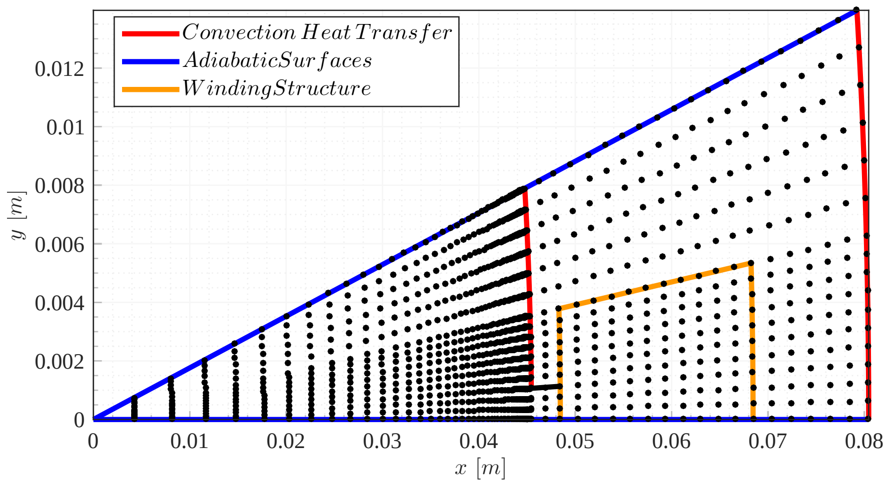

Figure 3.4: FDM node distribution selected for the analysis of SRIM. The adiabatic surfaces are highlighted in blue while the surfaces where heat transfer convective phenomena take place are presented in red.

The FE software FEMM is used to validate the model. Since it does not allow the implementation of additional resistance networks to account for the axial thermal effects, the radial FDM is validated considering a structure where the fixed temperature boundary condition is imposed at the rotor's inner bore $r_I \neq 0$. Moreover, the linear rotor node distribution is used for the FE package to reduce the time for the mesh generation without which would result in an high computational task. The heat transfer coefficient adopted in the radial model and in the end region are listed in Table 3.2 resulting from the relations presented in the previous section.

A constant heat source in both the rotor and stator winding elements is imposed $P_{L-E,J-r} = 1.4\,[kW]$ and $P_{L-E,J-s} = 2\,[kW]$, respectively. The inner node temperature is defined as $T_I = 80\,[^{\circ}C]$ and the bulk jacket fluid coolant (water) temperature is $T_w = 120\,[^{\circ}C]$. The FDM temperature distribution is compared with the FE solution in Figure 3.5 and good agreement is demonstrated [96].

Table 3.2: Convection Heat Transfer Coefficient

Region	Symbol	$h\,[W/(m^2 \cdot K)]$
Radial Model		
Water Jacket	${}^{w}h$	2180
Main air gap	${}^{g}h$	210
End Region Model		
Bottom Winding	${}^{wb1}h$	75
Rotor	${}^{ra}h$	140
Bottom Housing	${}^{ah}h$	67
Front Winding	${}^{wf}h$	35
Top Winding	${}^{wt}h$	10.5

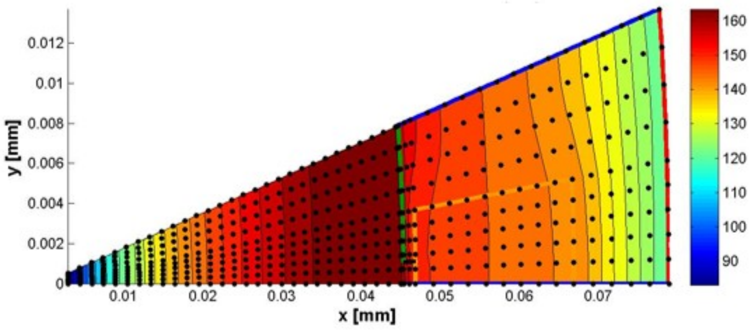

(a) FDM solution

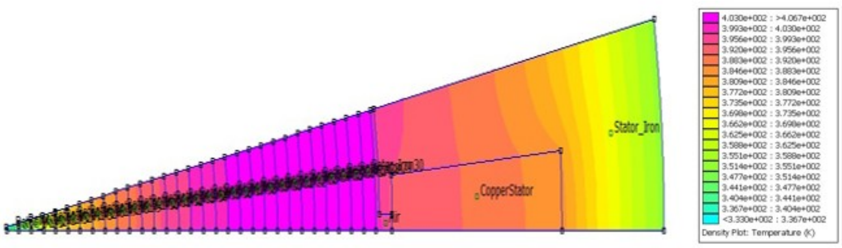

(b) FE solution computed with FEMM software package

Figure 3.5: Temperature distribution comparison for the 2−d radial temperature distribution.

The fixed temperature boundary condition effectively becomes a drain for the rotor heat which does not need to significantly force heat flux through the main air gap. The water jacket cooling results are very effective at extracting the heat from the stator structure, and maintaining the operative temperature below the critical values.

The FDM has been proven reliable in the prediction of temperature in high speed machines [96,143,148]. The axial resistance network is coupled with the radial thermal model and the rotor is considered to be a full cylinder ($r_I = 0$). The temperature distribution within the structure is computed assuming an identical input with respect to the previous case. The equilibrium of the inner node is affected by both the radial and axial heat flow. The rotor losses density distribution is computed according to the electromagnetic field distribution. The total rotor losses are assumed to be uniformly distributed in the rotor structure or the actual radial losses distribution can be considered directly as an input for the thermal model. Comparison of the temperature distribution computed assuming uniform rotor loss density is shown in Figure 3.5a and Figure 3.6a, where the result are presented for a fixed inner rotor temperature and a fully coupled model with the axial thermal network, respectively. The variation in the peak values and distribution achieved is mainly related to the reduced heat extraction capabilities from the rotor center when the axial phenomena are considered. The temperature tends to become uniform across the rotor as can be seen by imposing zero heat flux in the rotor singularity and fixed air temperature as computed by the FDM in (3.3).

The high power loss density in proximity of the air gap reduces the effectiveness of the rotor's heat dissipation phenomena that occurs in the end region; furthermore, the heat components which are transferred from rotor to stator are less affected by the cooling provided by the water jacket. This leads to an increased peak rotor temperature which will impact on the rotor's resistivity and consequently the performance.

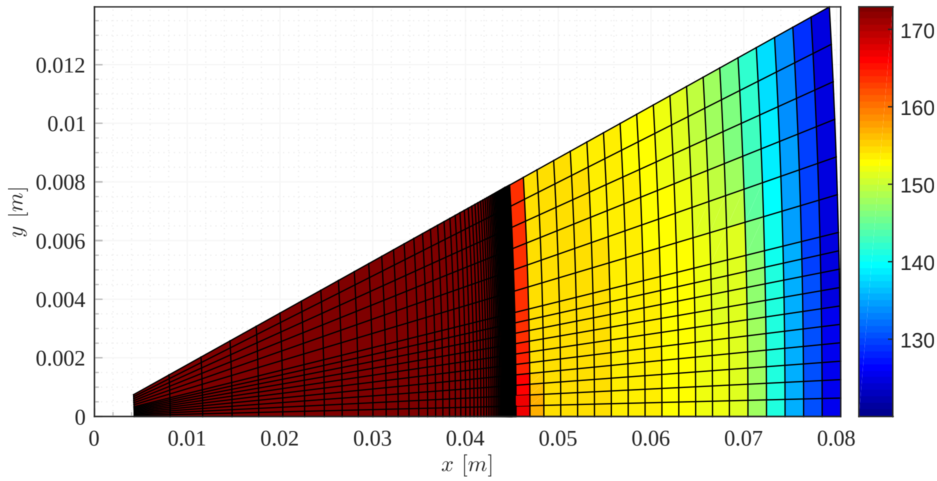

(a) FDM solution for radially uniform rotor power losses distribution

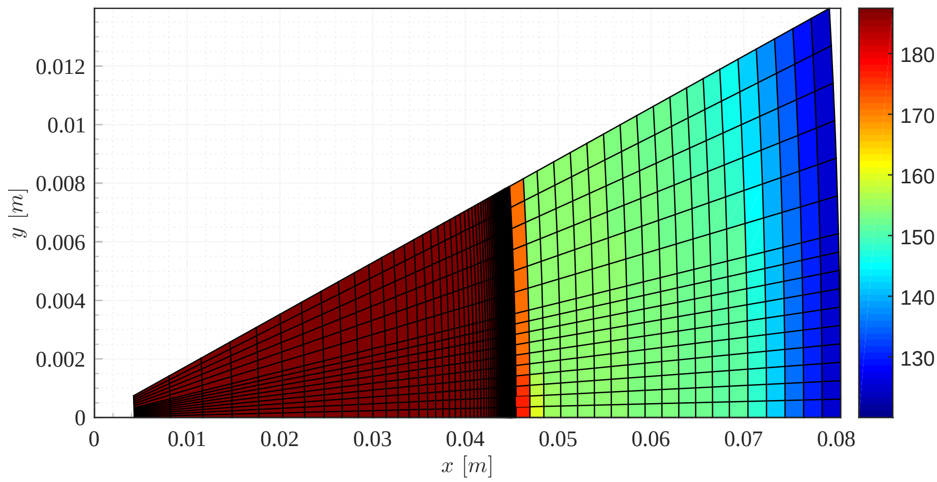

(b) FDM solution for radial rotor power losses distribution determined by means of DDM

Figure 3.6: Temperature distribution comparison for the 2−d radial temperature distribution.

The rotor losses computed by the analytical model presented in the previous section and depicted in Figure 2.19 are used as the input of the thermal model. The thermal management technique considered enables the stator winding peak temperature to be maintained within safe operative limits. However, in Figure 3.7 the dependency of the rotor temperature on the rotor slip is presented. The radial distribution of the losses is considered.

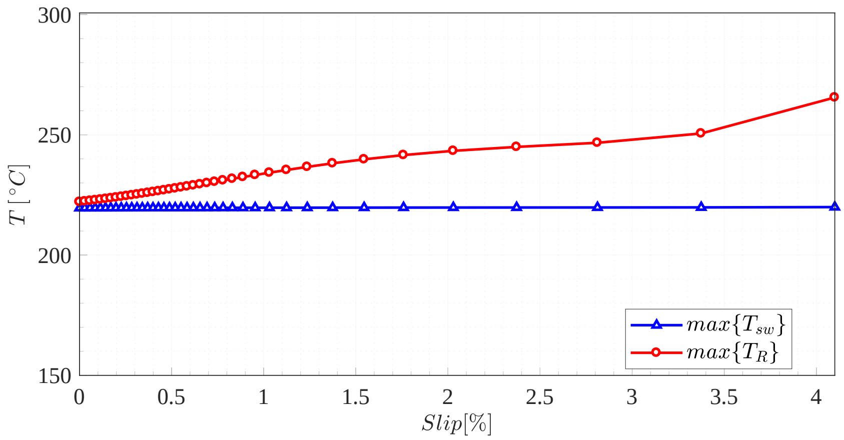

Figure 3.7: Rotor temperature T_R and winding temperature T_{sw} against slip. The current amplitude, therefore the related stator winding losses, are constant while the rotor losses are strongly dependant on the operative slip.

The resistivity of the rotor material can therefore be computed for each node of the rotor grid and for each operative condition. The temperature distribution is here considered as the parameter which links the electromagnetic and thermal models.

3.2 The Mechanical Stress Model

The mechanical stress applied to the rotor due to centrifugal forces, temperature distribution, and pressure need to be accounted for at the design stage to guarantee the mechanical integrity of the rotating element. In order to obtain the fundamental physical behaviour, the stress distribution within the solid rotor structure is required. The rotor structure is modelled as a full or hollow cylinder rotating along it's axis of rotation. Considering a cylindrical coordinate system, the main stress components result in a solution of the stress equation that is derived using the *congruence* equations, and *equilibrium* equations [72, 158, 159]. The bi-dimensional approximation of the problem is justified by means of the external load acting on the rotor, resulting mainly in the radial and tangential direction. In the *plane theory of elasticity*, two general types of problems are defined, the *plane stress* and *plane stain*. The axisymmetric nature of the geometry and the definition of the coordinate system in correspondence with the principal axis enables only the principal stress to be considered. Assuming an infinitesimal element of the structure as depicted in Figure 3.8, the equilibrium equation for the structure in rotation along its principal axes of inertia results in a PDE function of the radial and tangential stresses, $\sigma_r(r)$ and $\sigma_\theta(r)$, respectively.

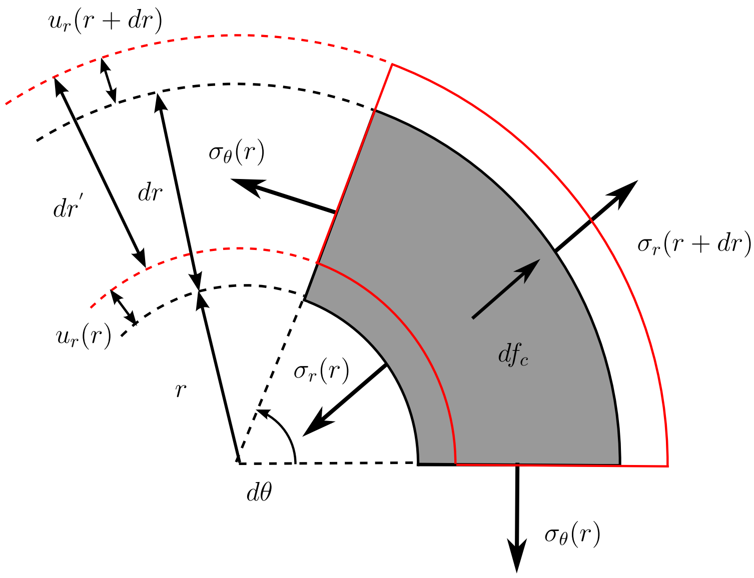

Figure 3.8: Infinitesimal rotor volume

By neglecting the high order terms, the equilibrium equation can be expressed as

$$r\,\frac{\partial\,\sigma_r(r)}{\partial\,r} + \sigma_r(r) - \sigma_\theta(r) = -\rho\,\omega_m^2\,r^2 \tag{3.21}$$

where $\rho\,[{}^{kg}/_{m^3}]$ is the mass density of the rotor material and $\omega_m\,[{}^{rad}/_{sec}]$ is the rotational angular speed.

The *plane stress* problem is defined as the the state of stress when the stress normal to the bi-dimensional computational domain is assumed to be zero ($\sigma_z = 0$). The state of stress where the strain normal to the computational domain is assumed to be zero ($\varepsilon_z = 0$) is defined as *plane strain*. The solution for the *plane stress* is discussed here as it is suitable for the length-to-diameter ratio of the structure considered. The generalised *Hook's law* in cylindrical coordinates for the *plane stress* problems can be expressed as

$$\begin{cases} \varepsilon_r(r) = \dfrac{\partial\, u_r(r)}{\partial\, r} = \dfrac{1}{E}\Big[\sigma_r(r) - \nu\, \sigma_\theta(r)\Big] + \alpha_r\, \Delta T(r) \\ \varepsilon_\theta(r) = \dfrac{u_r(r)}{r} = \dfrac{1}{E}\Big[\sigma_\theta(r) - \nu\, \sigma_r(r)\Big] + \alpha_\theta\, \Delta T(r) \\ \varepsilon_z(r) = -\dfrac{\nu}{E}\Big[\sigma_r(r) + \sigma_\theta(r)\Big] + \alpha_z\, \Delta T(r) \end{cases} \tag{3.22}$$

where $u_r(r)$ and $\Delta T(r)$ are the functions that define the radial displacement and temperature distribution, respectively. α_r, α_θ, and α_z are the expansion coefficients in the radial, tangential and axial directions, respectively. Combining (3.21) and (3.22), the PDE that defines the mechanical stress problem results in (3.23) where the *Young's* modulus $E\,[MPa]$ and *Poisson's* ratio $\nu\,[pu]$ are material constants [159–161].

$$r\,\frac{\partial^2\, \sigma_r(r)}{\partial\, r^2} + 3\frac{\partial\, \sigma_r(r)}{\partial\, r} + (3+\nu)\,\rho\, r\, \omega_m^2 + \alpha\, E\, \frac{d}{dr}\Delta T(r) = 0 \tag{3.23}$$

The radial stress function is split into its components directly related with the temperature distribution ${}^{\tau}\sigma_r$, angular rotational speed ${}^{\omega}\sigma_r$, and contact pressure ${}^{p}\sigma_r$ [73]

$$\sigma_r(r) = {}^{\tau}\sigma_r(r) + {}^{\omega}\sigma_r(r) + {}^{p}\sigma_r(r) \tag{3.24}$$

Each component is computed considering the effect of a single excitation quantity. The general solution for each of the radial stresses is reported in (3.25a),(3.25b), and (3.25c).

$${}^{\omega}\sigma_r(r) = \sigma_r(r)\Big|_{p=0,\Delta T=0} = A + \frac{B}{r^2} - \frac{\rho}{8}\,(3+\nu)\, r^2\, \omega_m^2 \tag{3.25a}$$

$${}^{\tau}\sigma_r(r) = \sigma_r(r)\Big|_{p=0,\omega_m=0} = A + \frac{B}{r^2} - \alpha\, E\, r\, \tau(r) \tag{3.25b}$$

$${}^{p}\sigma_r(r) = \sigma_r(r)\Big|_{\omega_m=0,\Delta T=0} = A + \frac{B}{r^2} \tag{3.25c}$$

The tangential component of the stress results in $\sigma_\theta(r) = {}^{\tau}\sigma_\theta(r) + {}^{\omega}\sigma_\theta(r) + {}^{p}\sigma_\theta(r)$ after substituting (3.25a),(3.25b) and (3.25c) into (3.21). The solution of the plain *strain* problem enables the computation of the radial deformation of the structure as presented in (3.26) [73].

$$u_r(r) = A\,r + \frac{B}{r} - \frac{(1-\nu^2)}{8\,E}\,\rho\,r^3\,\omega_m^2 + (1+\nu)\,\frac{\alpha}{r}\int \Delta T(r)\,r\,dr \tag{3.26}$$

According to (3.22), the radial displacement function is split into the temperature, rotational speed, and pressure components, ${}^{\tau}u_r$, ${}^{\omega}u$ and ${}^{p}u$, respectively. A consistent set of boundary conditions have to be defined in order to compute the solution of the stress distribution. In [158] the radial and tangential stress distribution solutions are determined for a hollow cylinder, full cylinder and for a layered structure. Considering the general solution (3.25a), the integration constant, B is zero for the case of a full solid cylinder because the stress at the center of the structure has to be finite or in other terms, the radial displacement imposed has to be null. The boundary conditions for the smooth solid cylinder are presented in (3.27).

$$\begin{cases} {}^{\omega}u_r(r)\Big|_{r=0} \neq \infty \\ {}^{\omega}\sigma_r(r)|_{r=r_R} = 0 \end{cases} \tag{3.27}$$

The integration constant for the hollow cylinder case are computed imposing null radial stress at the inner (r_I) and outer bore (r_R) of the cylinder as expressed in (3.28).

$$\begin{cases} {}^{\omega}\sigma_r(r)|_{r=r_I} = 0 \\ {}^{\omega}\sigma_r(r)|_{r=r_R} = 0 \end{cases} \tag{3.28}$$

Analogous considerations lead to the boundary conditions for (3.25b) and (3.25c). The function $\tau(r)$ introduced in (3.25b) is obtained by substituting the function $\Delta T(r)$ into (3.23) and computing the solution [161]. In [160] the problem is solved for a linear temperature distribution. The boundary conditions required for (3.25c) are of particular interest if a layered structure is considered, e.g. shaft-to-laminations interference calculation [162], rotor sleeve dimensioning [73,160], and a multi-layer structure interference fit calculation [158].

The theories of material failures (*Von Mises* [163], *Tresca* [73]) defines the reference stresses to guarantee safe operation of the rotor before elastic failures occur. The equivalent stress has to be kept lower than the yield strength, σ_Y of the constitutive rotor material. Considering *Von Mises* yield criterion, (3.29) is defined

$$\sigma_{eq}(r) = \sqrt{\sigma_r^2(r) + \sigma_\theta^2(r) - \sigma_r(r)\,\sigma_\theta(r)} \tag{3.29}$$

The safety factor κ_σ is introduced to account for a margin of error in the calculations resulting in

$$max\Big\{\sigma_{eq}(r)\Big\} = \tilde{\sigma}_{eq} < \frac{\sigma_Y}{\kappa_\sigma} \tag{3.30}$$

In Figure 3.9 the radial and tangential stresses for a smooth solid rotor with characteristics according to Table 2.2 are presented.

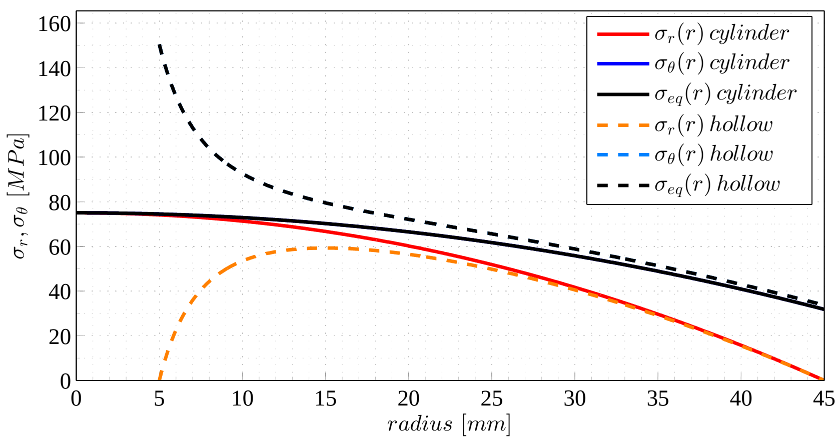

Figure 3.9: Radial $\sigma_r(r)$, tangential $\sigma_\theta(r)$ and equivalent $\sigma_{eq}(r)$ stress distribution for a rotor structure featuring $r_R = 45\,[mm]$ considering $\rho = 8000\,[{}^{kg}/{}_{m^3}]$, $\nu = 0.3$, $\omega_m = 32\,[krpm]$

The hollow and full cylinder cases are considered. According to (3.25a), the maximum stress component occurs at the inner radius bore r_I for what concerns both radial and tangential stress in a full cylinder. Hollow cylinders are instead characterised by a maximum tangential component at the inner bore while the radial stress feature its maximum value at $\tilde{r} = \sqrt{r_I\, r_R}$ [158]. The maximum equivalent stress occurs in the inner bore region and in the center of the structure for the hollow and full cylinder, respectively. The results presented in Figure 3.9 suggests that the shaft in a SRIM is preferably manufactured from the rotor material itself in order to simplify the manufacturing process and to reduce the stresses on the material. In this case, the equivalent stress equals the tangential stress component. The maximum value of the equivalent stress is therefore the tangential stress component computed at the inner radius of the structure.

$$^{f}\tilde{\sigma}_{eq} = {}^{f}\sigma_{eq}(r=0) = \frac{(3+\nu)}{8}\,\rho\, r_R^2\,\omega_m^2 \tag{3.31}$$

$$^{h}\tilde{\sigma}_{eq} = {}^{h}\sigma_{eq}(r=r_I) = \frac{\rho\,\omega_m^2}{4}\left[(1-\nu)\,r_I^2 + (3+\nu)\,r_R^2\right] \tag{3.32}$$

where $^{f}\tilde{\sigma}_{eq}$ and $^{h}\tilde{\sigma}_{eq}$ are referred to the full cylinder and hollow cylinder case, respectively.

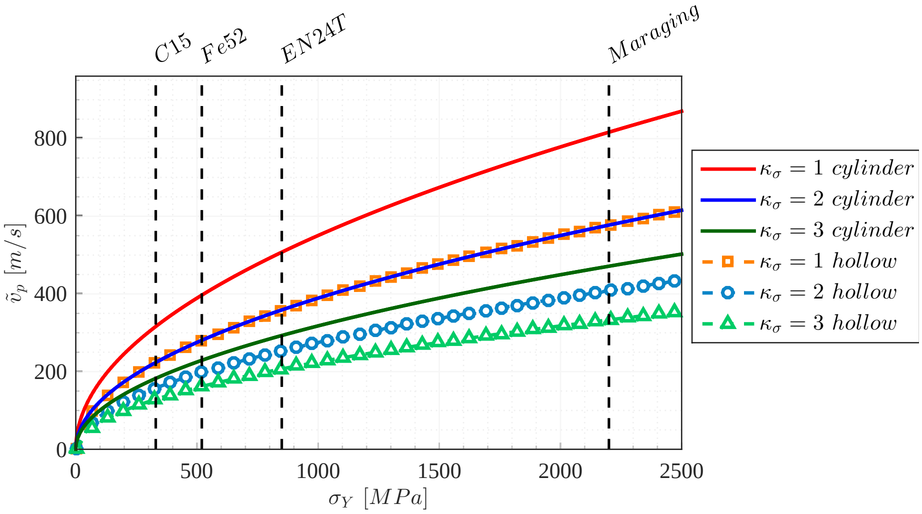

Figure 3.10: Maximum peripheral speed against the yield strength of rotor material for a smooth solid rotor structure for both full and hollow cylindrical cases. The yield strength of commercially available materials are highlighted.

Combining (3.30) with (3.31) and (3.32) after having defined the peripheral speed as $v_p = r_R\,\omega_m$, the maximum peripheral speed for both full and hollow cylinder is estimated as

$$ {}^{f}\tilde{v}_p < \sqrt{\frac{8\,\sigma_Y}{\kappa_\sigma\,\rho\,(3+\nu)}} \tag{3.33} $$

$$ {}^{h}\tilde{v}_p < \sqrt{\frac{4\,\sigma_Y}{\kappa_\sigma\,\rho\,(3+\nu)} - \frac{(1-\nu)}{(3+\nu)}\,r_I^2\,\omega_m^2} \tag{3.34} $$

According to the previous relations, it is possible to conclude that ${}^{f}\tilde{v}_p \approx \sqrt{2}\;{}^{h}\tilde{v}_p$ as presented in Figure 3.10.

However, the discretised approach adopted for the electromagnetic calculation (DDM) and the temperature distribution (FDM) can be extended for the mechanical stresses calculations and is presented in the following section.

3.2.1 The Multi-Layer Structure Stress Calculation

According to the selected node distributions for the DDM and FDM of the rotor structure as presented in Figure 2.7a, for each layer, identical considerations have to be made regarding displacement, equilibrium, stress, and strain as presented above. (3.23) and (3.26) are defined in each layer and their solution depends on the boundary conditions defined at the interfaces between adjacent layers. Currently, additive manufacturing and iron powder technology enables solid bulk of material featuring graded electromagnetic, mechanical and thermal properties to be produced requiring more accurate models to be needed. Furthermore, SRIMs that feature copper coating and layered composite structures are preferred for high speed applications due to their superior performances compared to smooth SR structures. The manufacturing of layered structures for high speed applications requires the study of the assembly procedure. Shrink-fit, positive gradient shrinkage, adhesive connection, hot isostatic pressing, explosion technique, dedicated geometry design, and electro-deposition are just some of the technologies available to assemble multi-layer structures. The impact of the rotational speed ω_m, temperature distribution, ΔT, and assembly pressure p on the stress and radial displacement of each layer is a critical aspect to be accounted for.

The integrity of the structures in static conditions relies on the static pressure applied during the assembly procedure. Let's define $r'_{o,h}$ and $r'_{i,h}$ the outer and inner radius of the pre-assembled generic layer, respectively, as presented in Figure 3.11a. A static stress condition on the structure is imposed by the layers deformation after the assembly. The assembled rotor layers feature a common interface, Γ_h at the radius, r_h as presented in Figure 3.11b. Let's define the static interference fit as [162, 164]

$$^{p}\delta_h = {}^{p}u_{r,h} - {}^{p}u_{r,h+1} = r'_{i,h} - r'_{o,h+1} \tag{3.35}$$

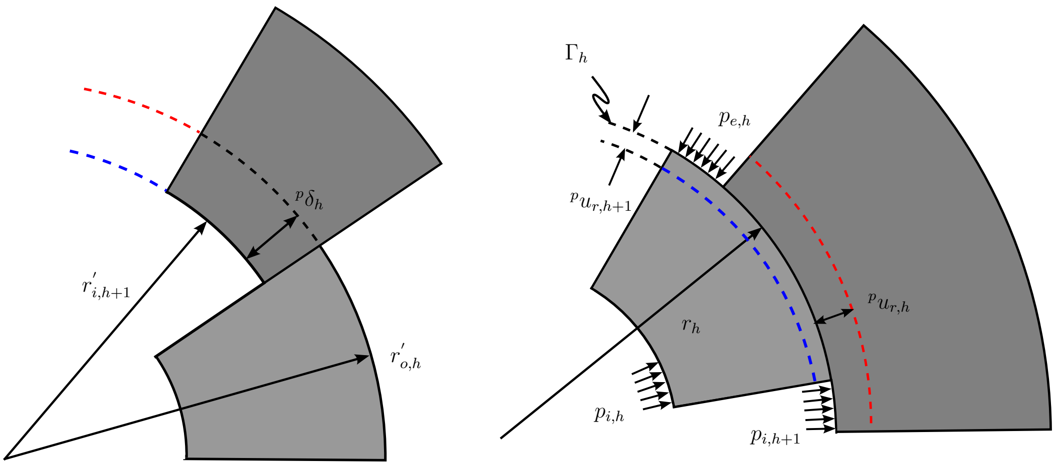

(a) Pre-assembly layer structures **(b)** Assembled layer structures

Figure 3.11: Pre-stressed multi-layer structure: detail of the pre-stress interference fit and resulting assembled structure.

The resulting radial $^{p}\sigma_r$ and tangential $^{p}\sigma_\theta$ stresses can be calculated according to (3.25c) [161, 162] by imposing consistent boundary conditions. Furthermore, the radial and tangential stress resulting from the angular speed and temperature distribution on the layer are computed according to (3.25a) and (3.25b). The validity of the proposed formulation lies under the assumption that the radial stress is transmitted between consecutive layers. The continuity of the radial stress at the interface, in combination with the boundary conditions defined describes the radial displacement of the layer bore that has to be imposed at each interface Γ_h of the inner layers of the structure.

$$\begin{cases} \sigma_{r,h}(r_h) = \sigma_{r,h+1}(r_h) \\ r^{'}_{i,h+1} + u_{r,h}(r^{'}_{i,h+1}) = r^{'}_{o,h} + u_{r,h}(r^{'}_{o,h}) \end{cases} \forall\, h \in \{2 \div L-1\} \tag{3.36}$$

The boundary condition for the inner bore of the structure can be written as (3.27) and (3.28) for a full and hollow cylinder, respectively. The radial stress must vanish at the rotor outer bore and therefore, $\sigma_{r,L}(r_R) = 0$ is the boundary condition of the outer interface. Similarly to the discretised domain solution of the electromagnetic and thermal problem, the set of conditions previously presented defines $2\,L$ linear equations. Let's define $\mathbf{S}$ as the matrix of the boundary conditions coefficient and $\bar{p}$ as the vector of the known terms. The integration constant vector $\bar{b}$ is computed by means solving the algebraic linear system defined and therefore leading to

$$\bar{b} = \mathbf{S}^{-1}\,\bar{p} \tag{3.37}$$

The *loss of contact* is considered a mechanical failure condition for the rotor structure and therefore a negative radial stress has to be guaranteed for all rotational speeds and temperature distributions in which the machine is required to operate. Furthermore, the condition (3.30) from the material failure theory has to be considered and directly translates to safe operative conditions which needs to be verified and are computed as below

$$\begin{cases} \sigma_r(r_h) < 0 \\ max\{\sigma_{eq,h}(r)\} < \dfrac{\sigma_{Y,h}}{\kappa_\sigma} \end{cases} \tag{3.38}$$

3.3 Rotor-dynamics Analysis

The rotor-dynamic analysis of the high speed machine consists of the evaluation of the critical frequencies, dynamic response, vibrations and stresses on the bearing. The overall shaft needs to be take into account as the dynamic response is affected by all the element of which the drive-train consists. The drive-train of high speed IM integrated with compressors and turbines presents the rotor of the electrical machine directly coupled with the high performance stages of the compressor/turbine supported by bearings. The effect of the additional vibrations introduced are required to be accounted for in order to define the safe operative condition of the drive-train. The calculation of the rotation speed at which the natural frequency of the system coincides with the frequency of the excitation forces is an important aspect to be accounted for in the design of a rotor for high speed applications. The operation in proximity of the critical speed may induce excessive vibrations level and in the worst case, failures. The variation of the natural frequencies with respect to the rotation speed is generally presented in the *Campbell* diagram [72]. The critical speeds are evaluated intersecting the forcing forces with the natural frequency of the structure. The vibration modes of rotating shaft are distinguished in rigid, flexural and mixed [72]. The rigid body modes are characterised by negligible deformation of the rotating element with respect to the bearing one. The design of the rotor for high speed machines focuses on the flexural critical speed as the vibration levels and stresses on the structure are more severe. The rotor structure deformation and its internal damping plays an important role in the flexible rotor modes. The rotor structure of high speed machines are generally designed considering a margin between the first flexural critical speed ${}^{cr}\omega_{f,1}$ and the maximum operative speed of the machines $\tilde{\omega}_m$ in order to avoid excessive vibrations and the crossing of critical speed. However, in certain applications, electrical machines are operated in the super-critical range. The critical speed safety factor for sub-critical operative condition is introduced and (3.39) summarise the rotor dynamic requirement for safe operation.

$$\tilde{\omega}_m < \frac{{}^{cr}\omega_{fw,1}}{\kappa_{cr}} \tag{3.39}$$

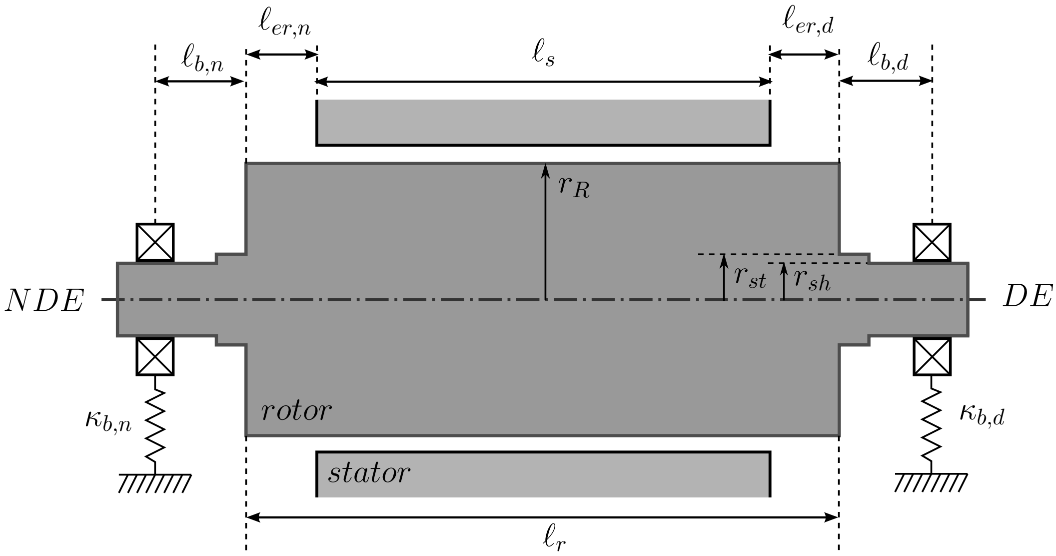

Figure 3.12: The solid rotor on flexible bearing support

The solid rotor structure is considered supported by means of radial bearing both at the drive end (DE) and non drive end (NDE) as presented in Figure 3.12. The isotropic bearing system is modelled as springs support located at the bearing seat axial length and characterised by their stiffness $\kappa_{b,n}$ and κ_b.

Various methods have been proposed to evaluate the critical frequency of rotor structure and evaluate the frequency response of drive-shaft in their operative conditions adopting different theoretical and computational approaches [165, 166]. The eigenvalue problem of free un-damped rotor model is adopted to compute the natural frequencies of the structure. Historically, the *Euler-Bernoulli* theory (1773) have been the first proposed method to study the deflection of beams under various load conditions. The assumptions of plane section perpendicular to the the bending line limits the validity of the proposed theory. Defining a curvilinear variable ξ, the time-dependant mono-dimensional bending line equation of an axisymmetric beam $\phi(\xi, t)$ results expressed as

$$\frac{\partial^2}{\partial \xi^2}\left(E(\xi)I(\xi)\frac{\partial^2 \phi(\xi,t)}{\partial \xi^2}\right) + m(\xi)\frac{\partial^2 \phi(\xi,t)}{\partial t^2} = 0 \tag{3.40}$$

where $E(\xi)$ is the *Young* modulus, $I(\xi)$ is the area moment of inertia, $m(\xi)$ is the mass per unit length. In 1877, Lord Rayleigh proposed a formulation for elastic beams based on the *Euler-Bernoulli* model including the effect of the rotary inertia [166, 167].

$$\frac{\partial^2}{\partial \xi^2}\left(E(\xi)I(\xi)\frac{\partial^2 \phi(\xi,t)}{\partial \xi^2}\right) + m(\xi)\frac{\partial^2 \phi(\xi,t)}{\partial t^2} - J(\xi)\,\frac{\partial^4 \phi(\xi,t)}{\partial \xi^2\,\partial t^2} = 0 \tag{3.41}$$

Both *Euler-Bernoulli* and *Rayleigh* theory neglect the shear deformation of the beam and leads to overestimated natural frequencies of the structures and works better for slender beams. In [168], both *Rayleigh-Ritz* and *Dunkerley* equations are implemented for axially discretised rotor structure. The *Euler-Bernoulli* beam theory is applied [169] to determine the vibration modes and frequency response of stepped structures. The *shear* model [166] accounts for the shear deformation effect in the *Euler-Bernoulli* theory and leads to improvements in the natural frequencies prediction.

$$\begin{cases} \dfrac{\partial^2}{\partial \xi^2}\left(E(\xi)I(\xi)\dfrac{\partial^2 \phi(\xi,t)}{\partial \xi^2}\right) + m(\xi)\dfrac{\partial^2 \phi(\xi,t)}{\partial t^2} - G(\xi)\,\dfrac{\partial^4 \phi(\xi,t)}{\partial \xi^2\,\partial t^2} = 0 \\ \dfrac{\partial^2}{\partial \xi^2}\left(E(\xi)I(\xi)\dfrac{\partial^2 \vartheta(\xi,t)}{\partial \xi^2}\right) + m(\xi)\dfrac{\partial^2 \vartheta(\xi,t)}{\partial t^2} - G(\xi)\,\dfrac{\partial^4 \vartheta(\xi,t)}{\partial \xi^2\,\partial t^2} = 0 \end{cases} \tag{3.42}$$

In $1921-1922$ *Timoshenko* proposed a beam theory which includes both shear and rotary inertia effect in the *Euler-Bernoulli* model [72,166]. Remarkable improvement in the calculation of natural frequencies considering also non-slender beams and in the analysis of high frequency responses have been achieved. Analytical simplified models achieved imposing the boundary conditions to the different beam theories enables rapid prediction which results not accurate in case of complex rotor structures [73]. The FE formulation of the above models is nowadays widely adopted to predict the rotor dynamic behaviour of complex rotating structures under various load conditions [72].

Adopting the *Lagrangian* mechanics approach, the dynamic of rotor structures is modelled as (3.43) considering $\bar{q}$ the vector of the *Lagrangian* variables [72].

$$\mathbf{M}\,\ddot{\bar{q}} + (\omega_m\,\mathbf{G} + \mathbf{C})\,\dot{\bar{q}} + \mathbf{K}\,\bar{q} = \mathbf{F}\,\bar{u} \tag{3.43}$$

where $\mathbf{M}$ is the matrix of the mass, $\mathbf{K}$ the matrix of the stiffness, $\mathbf{G}$ is the skew-symmetric matrix of the gyroscopic effect, $\mathbf{C}$ is the matrix of the damping coefficients, $\mathbf{F}$ the matrix of the input coefficient and $\bar{u}$ is the vector of the excitations forces. The nature of the forces in high speed electrical machines can be found in the rotor weight distribution ${}^{w}P$ [72, 169], rotor unbalance ${}^{u}P$ [72], fluid flow induced forces in the main air gap ${}^{g}P$ [170], electromagnetic forces ${}^{e}P$ [72]. The FE formulation of (3.43) is adopted to study the dynamic of complex rotor structures [72]. The natural frequencies of the model are calculated as the solution of the free un-damped eigenvalue problem (3.44)

$$\mathbf{M}\,\ddot{\bar{q}} + \omega_m\,\mathbf{G}\,\dot{\bar{q}} + \mathbf{K}\,\bar{q} = 0 \tag{3.44}$$

3.3.1 Natural Frequencies Calculation

The solution of the beam equation for all the model presented is decomposed in its time and spatial component $\phi(\xi, t) = \zeta(\xi)\,\tau(t)$. Considering a time harmonic solution, the decoupling between the time and spatial equation can be performed. The governing equation of the rotor structure displacement function $\zeta(\xi)$ is therefore deduced. The rotor structure is assumed mechanically supported by mechanical ball-bearing which are modelled as linear spring. The isotropic bearing support system is considered where the front-end $\kappa_{b,n}$ and back-end $\kappa_{b,d}$ bearings are characterised by their stiffness $\kappa_{b,n} = \kappa_{b,d} = \kappa_b$. Furthermore, the rotor structure can be assumed at first instance featuring a constant cross section. Considering the *Euler-Bernoulli* beam model, the differential equation (3.40) results as

$$E\,I\,\frac{\partial^4\,\zeta(\xi)}{\partial\,\xi^4} - \beta^4\,\zeta(\xi) = 0 \tag{3.45}$$

where $\beta^4 = {}^{(\omega^2\,m)}/_{(E\,I)}$. The generic solution of (3.45) consist in a linear combination of hyperbolic terms

$$\zeta(\xi) = A\,sin(\beta\,\xi) + B\,cos(\beta\,\xi) + C\,sinh(\beta\,\xi) + D\,cosh(\beta\,\xi) \tag{3.46}$$

A consistent set of boundary conditions are required to define the problem and compute the integration constants. The boundary condition formulation for a beam on isotropic flexible supports results expressed as [171]

$$\xi = 0 \Rightarrow \begin{cases} E\,I\, \dfrac{\partial^2 \zeta(\xi)}{\partial \xi^2}\Big|_{\xi=0} = 0 \\ E\,I\, \dfrac{\partial^3 \zeta(\xi)}{\partial \xi^3}\Big|_{\xi=0} = -\kappa_b\, \zeta(\xi)\Big|_{\xi=0} \end{cases} \tag{3.47a}$$

$$\xi = \ell_a \Rightarrow \begin{cases} E\,I\, \dfrac{\partial^2 \zeta(\xi)}{\partial \xi^2}\Big|_{\xi=\ell_a} = 0 \\ E\,I\, \dfrac{\partial^3 \zeta(\xi)}{\partial \xi^3}\Big|_{\xi=\ell_a} = \kappa_b\, \zeta(\xi)\Big|_{\xi=\ell_a} \end{cases} \tag{3.47b}$$

Substituting (3.46) in (3.47), the eigenvalue problem can be formulated as

$$\mathbf{J}(\beta)\, \bar{k} = \bar{0} \tag{3.48}$$

where $\bar{N} = [A\ B\ C\ D]^T$ and $\mathbf{J}(\beta)$ is the matrix of the boundary condition coefficients. The computation of the natural frequencies and the mode shapes of the system is achieved determining the zeros of the characteristic equation of the beam $g(\beta) = det[\mathbf{J}(\beta)] = 0$. The characteristic equation is function of the β parameter only and consequently of ω. The zeros of the determinant are analytically solved for basic structure, whereas numerical computations are required for more complex cases [171].

Analogous consideration can be performed for the other model presented in the previous section. In particular, the elastic line governing equation considering the *Rayleigh* beam model under the assumptions considered for the *Euler-Bernoulli* beam results as

$$E\,I\, \frac{\partial^4 \zeta(\xi)}{\partial \xi^4} - \beta^4\, \zeta(\xi) + \beta^4\, \frac{I}{S} \frac{\partial^2 \zeta(\xi)}{\partial \xi^2} = 0 \tag{3.49}$$

where S is the beam cross section. The generic solution of (3.49) again take the form of a linear combination of hyperbolic terms

$$\zeta(\xi) = A\, sin(\alpha\, \xi) + B\, cos(\alpha\, \xi) + C\, sinh(\gamma\, \xi) + D\, cosh(\gamma\, \xi) \tag{3.50}$$

The calculation of the natural frequencies is achieved performing an identical procedure as the one detailed for the *Euler-Bernoulli* model previously detailed [166].

3.3.2 Discretised Rotor Model

The analysis of beam and rotor structures featuring discontinuities in the cross section has been subject of many studies in the last decades. The FEA approach to study non-uniform beam is the most accurate however resulting in high computational effort. A mid-complex system can be found defining an interface node for each rotor beam discontinuity (in general nodes can be place also where there are no discontinuities). In Figure 3.13, the discretised version of the rotor model presented in Figure 3.12 is depicted.

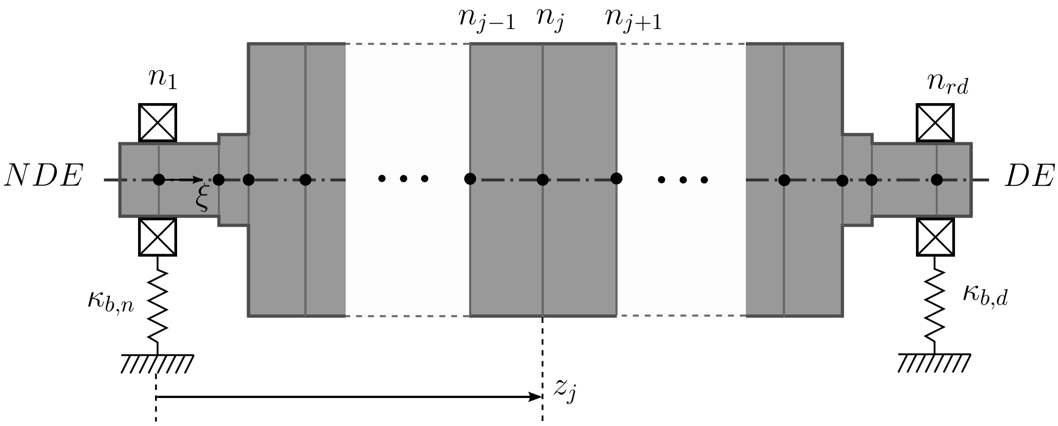

Figure 3.13: The discretised solid rotor rotor dynamic model with flexible bearing support.

The rotor discretisation is aiming to account account for the rotor material properties and cross section discontinuities. The spatial component of the beam model previously presented results as the governing equation defined in each rotor discrete element. Considering the *Euler-Bernoulli* equation and assuming that n_{rd} sectors are defined, (3.45) defined the transversal displacement function ζ_j with the curvilinear coordinate ξ for the continous j^{th} element [169].

$$(E_j I_j)\,\frac{\partial^4 \zeta_j(\xi)}{\partial\,\xi^4} - \beta_j^4\,\zeta_j(\xi) = 0 \qquad \forall\, j \in \{1 : n_{rd}\} \tag{3.51}$$

where $\beta_j = \beta_1\,\lambda_j$ and

$$\lambda_j = \sqrt[4]{\frac{m_j}{E_j\,I_j}\,\frac{E_1\,I_1}{m_1}} \tag{3.52}$$

The generic expression of the solution for the flexural mode shape function results expressed as

$$\zeta_j(\xi) = A_j\, sin(\beta_j\, \xi) + B_j\, cos(\beta_j\, \xi) + C_j\, sinh(\beta_j\, \xi) + D_j\, cosh(\beta_j\, \xi) \tag{3.53}$$

and A_j, B_j, C_j and D_j are the integration constant determined by means a consistent set of boundary/interface conditions.

The relations for the nodes located on the bearing axial position remains identical to the (3.47) identified for the continuous beam model. The interface condition at the generic node n_j located at distance z_j from the origin are defined in order to impose the continuity of the elastic fibre function and its derivative of the first, second and third order.

$$\zeta_j(z_j) = \zeta_{j+1}(z_j) \tag{3.54a}$$

$$\frac{\partial\, \zeta_j(\xi)}{\partial\, \xi}\Big|_{\xi=z_j} = \frac{\partial\, \zeta_{j+1}(\xi)}{\partial\, \xi}\Big|_{\xi=z_j} \tag{3.54b}$$

$$(E_j I_j)\, \frac{\partial^2\, \zeta_j(\xi)}{\partial\, \xi^2}\Big|_{\xi=z_j} = (E_{j+1} I_{j+1})\, \frac{\partial^2\, \zeta_{j+1}(\xi)}{\partial\, \xi^2}\Big|_{\xi=z_j} \tag{3.54c}$$

$$(E_j I_j)\, \frac{\partial^3\, \zeta_j(\xi)}{\partial\, \xi^3}\Big|_{\xi=z_j} = (E_{j+1} I_{j+1})\, \frac{\partial^3\, \zeta_{j+1}(\xi)}{\partial\, \xi^3}\Big|_{\xi=z_j} \tag{3.54d}$$

If (3.53) is substituted in the previous set of boundary conditions, a set of four equation. The overall system of boundary/interface conditions defines an linear system of equations which can be represented in its matrix form by means of the matrix of coefficients $\mathbf{J}$ and the vector of the known terms $\bar{k}$. Considering (3.52), the matrix of the boundary condition coefficients is function of β_1 only and the eigenvalue problem is therefore defined as

$$\mathbf{J}(\beta_1)\, \bar{k} = 0 \tag{3.55}$$

Identical elaborations can be performed considering the other model presented. The calculation of the natural frequencies of the system is always reduced to the form expressed in (3.55). The zeros of the characteristic function for the eigenvalue problem defines the critical frequency of the system.

3.3.3 Model Validation

The prediction of the critical frequencies achieved by means of the *Euler-Bernoulli* and *Rayleigh* models are compared with FE results. In Table 3.3 are listed the rotor dynamic model parameters considered.

Table 3.3: Rotor dynamic model parameters

Symbol	**Value**
$\ell_{b,n} = \ell_{b,d}$	$20\,[mm]$
$\ell_{st,n} = \ell_{st,d}$	$7.5\,[mm]$
ℓ_s	$150\,[mm]$
ℓ_r	$160\,[mm]$
r_{sh}	$15\,[mm]$
r_{st}	$17.5\,[mm]$

The discretised model is defined by means of $n_{rd} = 13$. The rotor is considered made of homogeneous material featuring $\rho_{d,r} = 8000\,[{}^{kg}/_{m^3}]$ and $E = 210\,[GPa]$. Both discretised and continuous models are implemented and the results are compared in Table 3.4. The over-prediction and error of +8% at high frequency confirm the expected limitations of the *Euler-Bernoulli* and *Rayleigh* models.

Table 3.4: Analytical and FE comparison of natural frequency calculations.

Mode	**FEA**	**Analytical**
Mode 1 (rigid)	$40850\,[rpm]$	$42993\,[rpm]$ (+5%)
Mode 2 (rigid)	$75780\,[rpm]$	$72750\,[rpm]$(−4%)
Mode 3 (flexural)	$444540\,[rpm]$	$480105\,[rpm]$ (+8%)

The variation of the critical frequencies with respect to the bearing stiffness is considered in order to correctly select the bearing topology and the results are presented in Figure 3.14. The bearing stiffness is selected aiming to operate the machine within a safety limit with respect to the critical frequencies of the system. $\kappa_b = 150\,[{}^{MN}/_{m}]$ is selected to guarantee a safety margin $\kappa_{cr} = 1.5$.

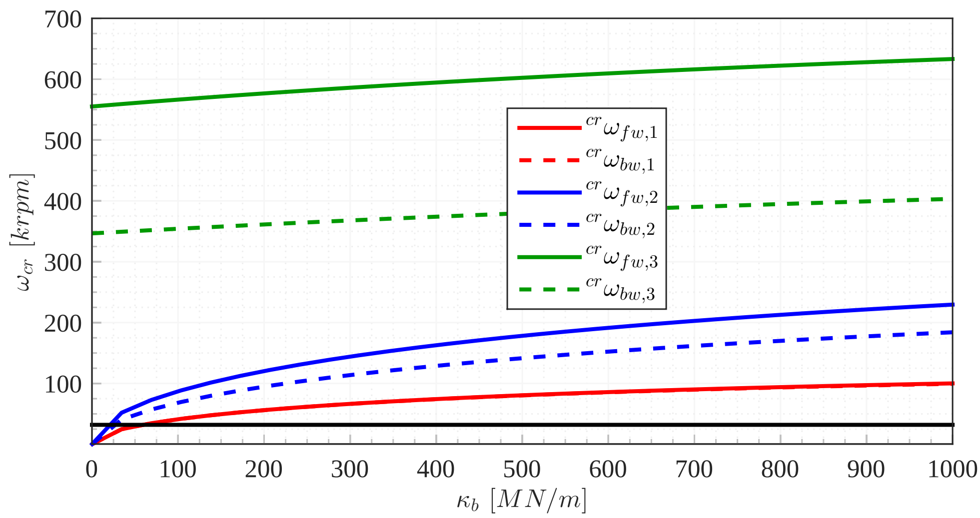

Figure 3.14: Critical frequency (${}^{cr}\omega$) against bearing stiffness (κ_b). The black solid line represent the maximum rotor operative speed.

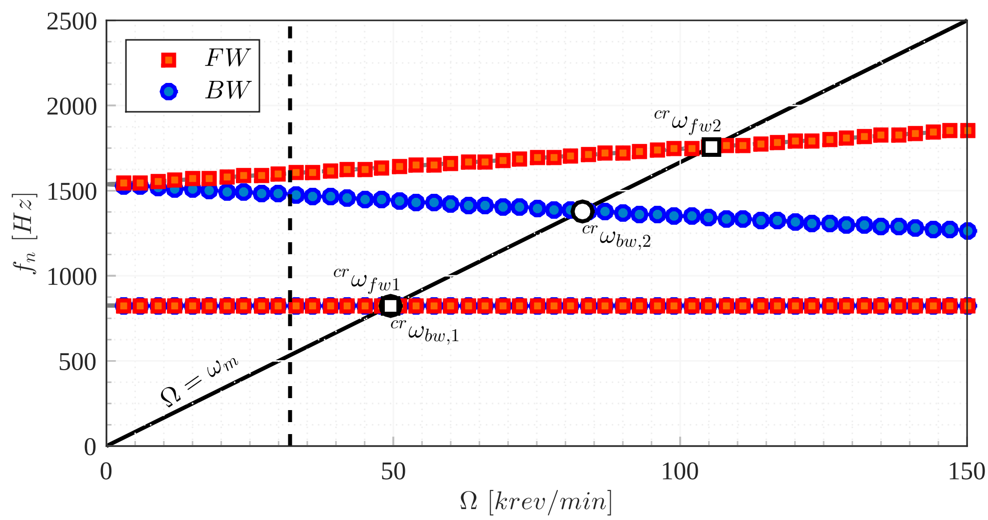

Figure 3.15: Campbell diagram of SRIM considering $\kappa_b = 150\,[{}^{MN}/_{m}]$. The vertical dashed line represent the maximum rotor operative speed.

The *Campbell* diagram computed by means of FE is presented in Figure 3.15. The intersection between the synchronous excitation line ($\Omega = \omega_m$) and forward and backward whirl natural frequency of the system defines the critical speed of the system. The mode shape related with the first, second, and third forward whirl critical speed are presented in Figure 3.16. Mixed modes characterise the rotor dynamic of the system. The first and second mode shapes are mainly of rigid nature. The first flexural mode is the most important to be accounted in the design of high speed machine as featuring rotor bending. The machine is safe to operate in the speed range below the threshold defined by the first critical bending mode [162]. The first forward whirl critical frequency related with bending mode occurs at ${}^{cr}\omega_{fw,3} = 575\,[krpm]$ and therefore the rotor is operated in the sub-critical with a good safety margin.

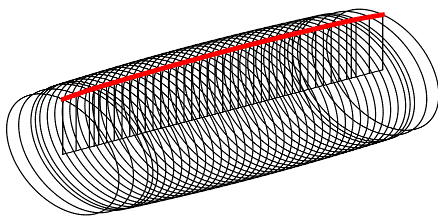

(a) 1^{st} Mode shape

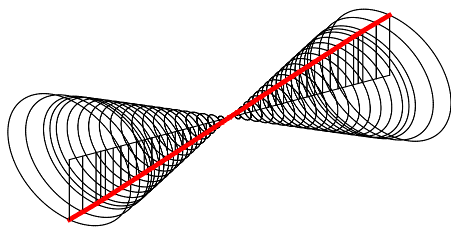

(b) 2^{nd} Mode shape

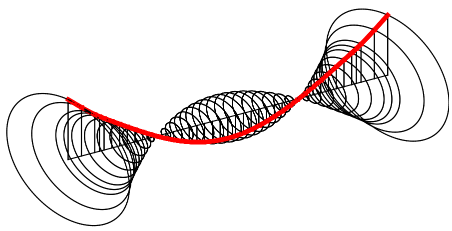

(c) 3^{rd} Mode shape

Figure 3.16: Mode shape for the first three forward whirl critical frequencies

3.4 Multi-physics Analysis

The fundamental aspects which have been described in the previous sections consider each phenomena being independent with respect to the others. The multi-physic approach in the analysis of SRIM is proposed aiming to account for the interaction between the different disciplines. The temperature distribution within the structures strongly impact on the electromagnetic, thermal and mechanical material properties of the SRIM and the coupling between the effect is a critical aspect to take into account [88]. However, the smooth SR structure considered as the case study in this document is modelled assuming that the magnetisation curve of the material remains constant for different operative conditions.

The robustness of the homogeneous rotor structure enables us to neglect the effect of the temperature distribution in the structural and rotor dynamic aspects. The thermal model links with the electromagnetic calculation by means of the correction parameters $\kappa_{T,r}$ and $\kappa_{T,sw}$ which define the temperature dependency characteristic of the rotor and stator winding resistivity. The density, kinematic viscosity and Prandlt number of the fluid in the main air gap is also considered temperature dependent.

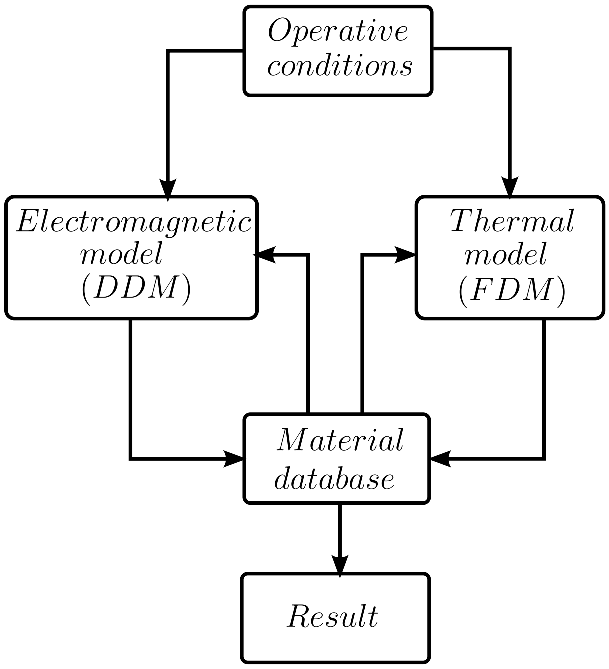

Figure 3.17: Flowchart of the coupled electro-magneto-thermal analysis of SRIM.

The thermal FDM is demonstrated a quick and accurate technique to calculate the temperature distribution in SRIM. An iterative loop has been designed in order to account for the multi-physics aspect of the machine. The calculation flow chart is presented in Figure 3.17.

The convergence criterion is defined on the temperature distribution. Considering a single operative condition, the final result is achieved when the variation between the temperature in each node of two consecutive step c and $c+1$ is lower than a threshold value Υ.

$$^{c+1}T(r,\theta) - {}^{c}T(r,\theta) < \Upsilon \qquad \forall\,(r,\theta) \in \Sigma \tag{3.56}$$

The result presented in Figure 3.7 can be therefore considered the step $c = 1$ of the multi-physics loop presented. The convergence is achieved in few iteration steps. According to the predicted temperature, the material database block updates the material properties according to the thermal status of the device. Neglecting the temperature variation of the fluid in the air gap, the steady state temperature trend for the simulated solid rotor induction machine is presented in Figure 3.18. The temperature dependency of both stator and rotor conductive elements lead to an increase in rotor and stator winding losses and, consequently their temperature.

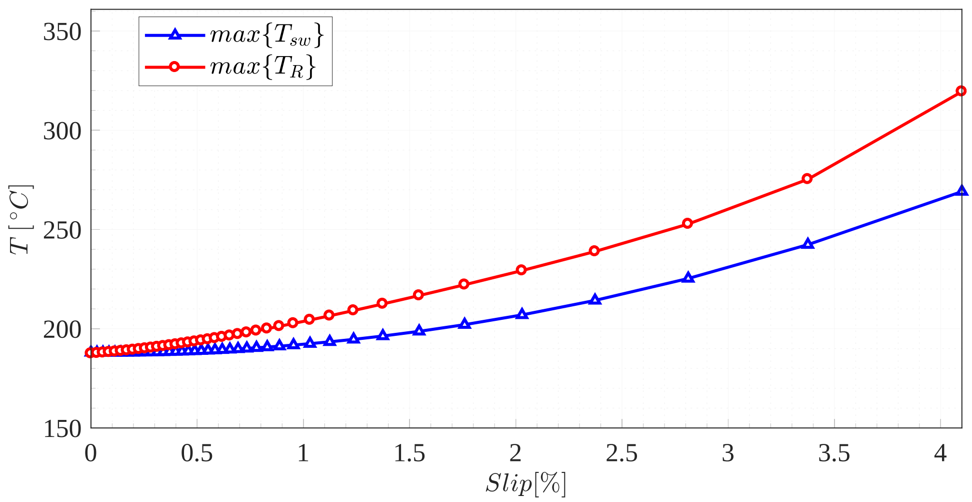

Figure 3.18: Steady state temperature trend against slip.

3.5 Summary

In this chapter, the building blocks for the analytical analysis of smooth and composite solid rotor induction machine have been presented. The discretised computational domain is proposed for the calculation of the multi-physics aspects that are necessary to achieve high performance machines. The models are very general and can be applied to different machine topologies. The coupling with the thermal and mechanical models presented, in combination with the rotor dynamic analysis, leads to the definition of a multi-physics environment suitable for a wide range of machine topologies. SRIM featuring copper coated structures can be analysed adopting the proposed modelling technique to account for the mechanical integrity of the rotor operating at high temperatures. The criterion to determine the maximum operative speed admissible for a selected power-speed node can be computed accounting for the rotor dynamic aspect. However, further improvements have to be made in the detailed aspects of the calculation. In particular, significant efforts have to be put in place in order to account for the three dimensional field and losses distribution in the rotor end region and stator end winding. Furthermore, the presented models require further elaborations, generalisation and improvements in every aspect, e.g. the accuracy of the field distribution with slotting can be improved by implementing the model proposed in [53]. The intrinsic three dimensional structure of the machine has to be properly modelled to achieve a more accurate temperature distribution prediction and investigate alternative cooling solutions. The stress and rotor dynamic model requires the implementation or approximated form of the non linearities of the material which could lead to further exploitation of the material yield.

CHAPTER

FOUR

SOLID ROTOR MATERIALS

The selection of the solid ferromagnetic material for SRIM is a critical aspect at the design stage. The electromagnetic characteristics of solid materials, in combination with their mechanical properties, are the main factor responsible for the output performance of SRIM. The required characteristic of rotor material for SR machines differs from the ones of cage rotor IMs. The rotor iron core in caged IMs features high conductivity material placed in dedicated slots. The aforementioned arrangement enables us to concentrate the effect of the electrical field in the rotor bars. While the currents are circulating in the high conductivity material, the magnetic field penetrates the ferromagnetic rotor core. In order to maximize the efficiency, the electrical steel adopted for a cage rotor IM is required to feature low losses at the rated operative conditions. The adoption of laminated steel is often considered in order to limit the eddy currents. The rotor losses are mainly generated by hysteresis effect on the rotor core and by joule loss in the rotor bars.

The materials adopted for SR machines require a good balance between the magnetic and electrical characteristics. The magnetic field penetration in the rotor core is affected by the relative permeability and the saturation flux density level. The eddy currents circulating in the rotor structure are strongly dependent on the electrical resistivity of the material. In contrast with the IMs, the electromagnetic fields in SRIM share the same media. The material selection is based on the balance between the above mentioned characteristics together with the mechanical capabilities, in order to guarantee the integrity of the rotating structure.

The single phase equivalent circuit model is widely adopted for the design and the analysis of IMs [52, 172] and SRIMs [26, 173]. The accuracy of the prediction is strongly related with the accuracy estimation of the lumped parameters that characterize the circuit. FE simulations have been used to calculate the parameters of IMs and good accuracy with respect the experimental results are demonstrated [52]. The combination of FEA and equivalent circuit results in a powerful tool which can account for the non-linearities of the material in the equivalent circuit parameters.

Aiming to assess the impact of the electromagnetic characteristic of the materials on the equivalent circuit parameters, non linear time-harmonic FE simulations are performed for different operative conditions. A fictitious parametric material is defined, enabling the investigation of the performance of SRIM considering different material characteristics. The calculation of the equivalent circuit parameters is performed also for the case study machine equipped with a cage rotor structure. The values of the equivalent circuit parameters of the HSIM are presented together with the SRIM results. Direct comparison of the performances can be performed considering the discrepancies in the results which are discussed in the following chapter.

4.1 The non-linear equivalent circuit

In Figure 4.1 the equivalent circuit model considered for the smooth SRIM is presented. The magnetising inductance L_m, rotor leakage inductance $L_{\sigma,r}$ and rotor resistance R_r are considered functions of the operative condition of the machine. FE simulations are adopted to compute the equivalent circuit parameters in order to account for the material non linearities. The simulation of no load conditions ($s = 0$) enables the characterisation of the magnetising inductance L_m.

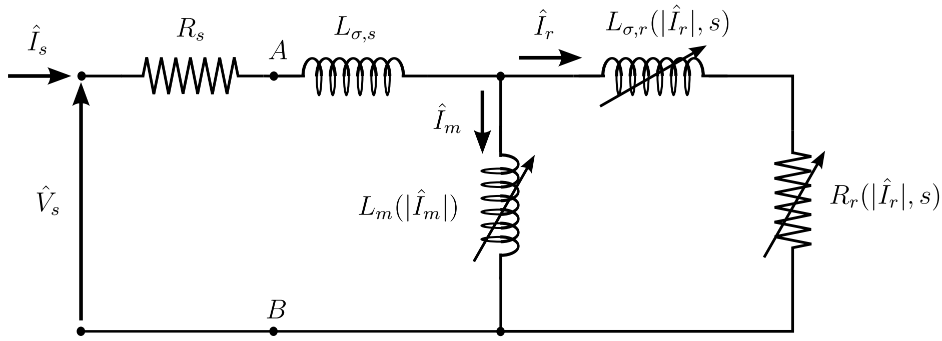

Figure 4.1: Non-linear single phase steady state equivalent circuit for smooth SRIM.

According to the *IEEE standard* [174], the locked rotor test ($s = 1$) is adopted to experimentally determine the rotor parameters. The computation of the rotor leakage inductance $L_{\sigma,r}$ and rotor resistance R_r is performed by means of emulating the locked rotor test in the FE environment. The locked rotor test performed at different supply frequencies and current levels has been demonstrated as a more accurate technique to be applied for induction machines featuring rotor structures with closed slots [97]. The impact of the electromagnetic properties of solid ferromagnetic materials has been investigated in [1, 56, 119] and the effect on the output torque and power factor of SRIM are presented.

4.2 Parametric Material

The modelling of the electromagnetic properties of the solid rotor material are considered in this section. A fictitious material is introduced in order to model the electromagnetic properties of solid material and investigate their impact on the machine performances. The relative initial permeability $\mu_{r,r}\,[pu]$, the saturation flux density $B_s\,[T]$ and the resistivity $\rho_r\,[\Omega m]$ are considered as variable parameters [1].

4.2.1 Magnetization Curve

The parametric material is implemented in the FE environment having defined (4.1) as the magnetization curve [175].

$$B(H) = \mu_0 \, H + 2 \, \frac{B_s}{\pi} \, atan \left(\pi \, H \, \frac{\mu_0 \, (\mu_r - 1)}{2 \, B_s} \right) \tag{4.1}$$

where $\mu_0 = 4 \, \pi \, 10^{-7} \, [{}^{H}\!/\!{}_{m}]$. The assumption of fundamental time harmonic component of the excitation current is considered when performing FE analysis adopting the time harmonic solver. The determination of the fundamental magnetization curve is therefore required to achieve reliable solutions. The DC magnetization curve is defined by means of a non-linear relation $B(H) = \mu(H) \, H$. The fundamental magnetization curve can be derived considering an ideal sinusoidal excitation featuring only the fundamental component expressed as ${}^1H(t) = H_M \, s(\omega \, t)$. The fundamental component of the flux density $B({}^1H(t))$ can be computed by means of *Fourier* transformation leading to the definition of the *Fundamental Magnetization Curve*

$${}^1\mu({}^1H) = \frac{{}^1B({}^1H)}{{}^1H} \tag{4.2}$$

The *rms* value of the fundamental component must be considered to achieve the *rms Fundamental Magnetization Curve.*

The computation of the fundamental component of the flux density according to the DC magnetization curve is performed through numerical calculation for different real material *B-H* characteristic [175].

4.2.2 Resistivity

The rotor material resistivity is modelled as a linear function of the operative temperature as expressed in (4.3).

$$\rho_R(T_R) = \rho_{R,T_{R,0}} \left(\kappa_{\tau,R}(T_R) \, \kappa_{er} \right) = \kappa_{er} \, \rho_{R,T_{R,0}} \left(1 + \alpha_R [T_R - T_{R,0}] \right) \tag{4.3}$$

having defined $\rho_{R,T_{R,0}} \, [\Omega m]$ the resistivity at the temperature $T_{R,0}$, $\alpha_R \, [{}^1\!/\!{}_{\circ C}]$ the resistivity temperature coefficient and $T_R \, [{}^\circ C]$ the operative temperature of the material. The correction factor κ_{er} has been introduced in *section* 2.1.10 in order to account for the three dimensional aspects of the field distribution.

The parametrization of the resistivity proposed in (4.3) enables to draw interesting considerations from the FE results. The operative temperature T_R and the end region factor κ_{er} can be deduced considering the inverse form of (4.3)

$$T_R = \frac{\rho_R}{\kappa_{er}\,\rho_{R,T_{R,0}}\,\alpha_R} - \frac{1-\alpha_R\,T_{R,0}}{\alpha_R} \tag{4.4}$$

$$\kappa_{er} = \frac{\rho_R}{\rho_{R,T_{R,0}}\left[1+\alpha_R\left(T_R - T_{R,0}\right)\right]} \tag{4.5}$$

The results achieved with the rotor resistivity parametrization can be therefore adopted to predict the SRIM performance under different rotor operative temperatures or considering different end region factors.

4.3 Sensitivity Analysis - No Load Condition

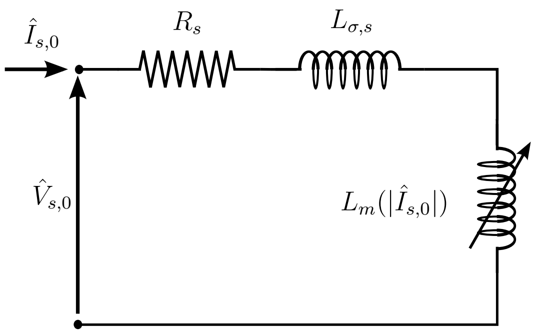

Figure 4.2: Non-linear single phase steady state equivalent circuit for smooth SRIM in no load operative conditions.

At no load operative condition, no current is induced in the rotor bars. The equivalent circuit is therefore simplified as presented in Figure 4.2. The no load characterization of SRIM performed for different excitation current amplitudes enables the calculation of the magnetising inductance $L_m(\hat{I}_{s,0})\,[H]$.

A balanced set of currents in the three-phase winding structure featuring peak amplitude $|\hat{I}_{s,0}|$ and non linear static solver are considered in the FE environment. The evaluation of L_m from the results can be achieved considering the voltage-current characteristic [172]. Alternatively, the flux linkage with the three-phase stator winding system [52, 176] is considered and the magnetising inductance result expressed as (4.6) where the flux linkages are averaged out [52] to account for the material non-linearities effect [176].

$$L_m(|\hat{I}_{s,0}|) = \frac{\sqrt{2}}{3}\left[\frac{\hat{\varphi}_a - {}^1\!/_2(\hat{\varphi}_b + \hat{\varphi}_c)}{|\hat{I}_{s,0}|}\right] \tag{4.6}$$

The stator leakage inductance is however considered embedded in the parameter L_m. This results in an approximation which only marginally affect the final calculations of the performances through the equivalent circuit as the value of the leakage inductance is generally negligible with respect to the magnetising $L_{S,\sigma} \ll L_m$ [172, 177].

The parameters' range and number of values considered are reported in Table 4.1.

Table 4.1: No Load sensitivity analysis parameters

Parameter	**Min**	**Max**	**# Values**
$\lvert\hat{I}_{s,0}\rvert\,[A]$	25	300	8
$B_S\,[T]$	0.5	2.5	9
$\mu_{r,r}$	20	5000	12

In the following plots, the lines in black correspond to the caged rotor IM parameter value. The lumped parameter of the high speed caged rotor induction machine (HSIM) are computed considering the design material [97] and therefore results constant with respect to the solid rotor material parameters are considered. However, the trend of the lumped parameters of the HSIM with respect the current and slip are accounted for in the calculations. The trend of L_m for different relative permeability values is presented in Figure 4.3 and Figure 4.4 for various excitation current amplitudes [98]. Assuming a monotonous trend of the inductance with respect to the parameters, the value above which the magnetising inductance is not subject to important variation is identified as the critical relative permeability μ_r^*.

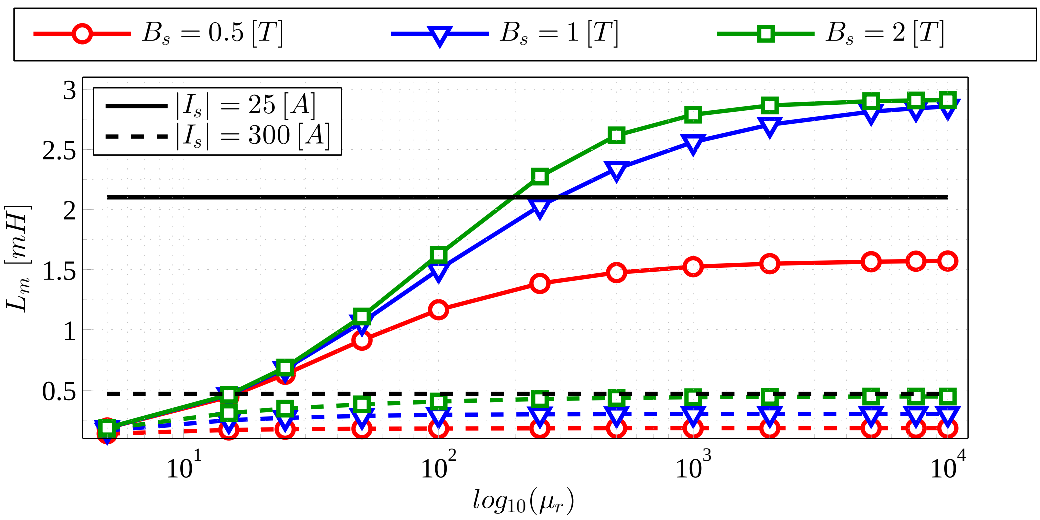

Figure 4.3: Magnetising inductance $L_m(\mu_r)$ for excitation amplitude $|\hat{I}_{s,0}| = 300\,[A]$ (dashed line) and $|\hat{I}_{s,0}| = 25\,[A]$ (solid line) considering different B_s values. The lines in black correspond to the HSIM parameter value.

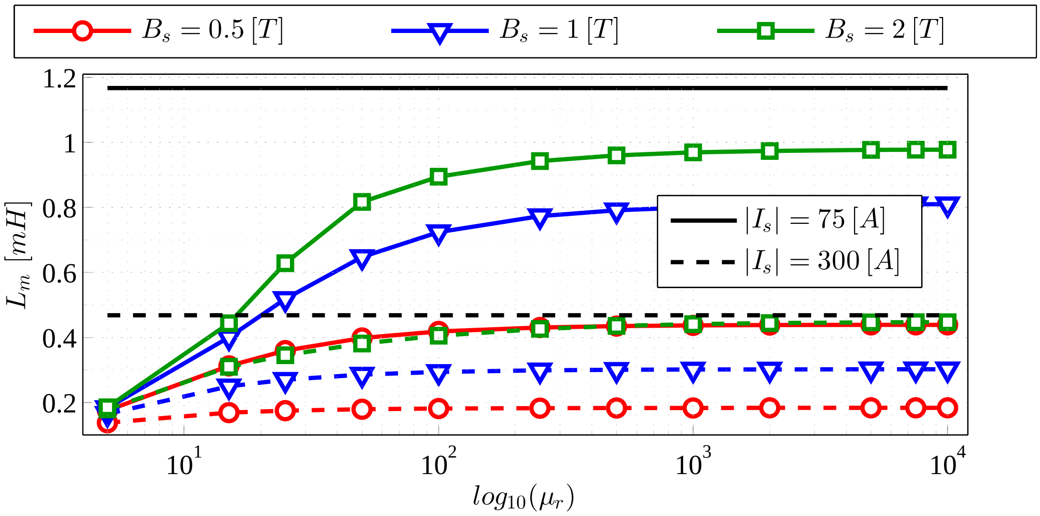

Figure 4.4: Magnetising inductance $L_m(\mu_r)$ for excitation amplitude $|\hat{I}_{s,0}| = 300\,[A]$ (dashed line) and $|\hat{I}_{s,0}| = 75\,[A]$ (solid line) considering different B_s values. The lines in black correspond to the HSIM parameter value.

The identification of the critical relative permeability value is performed considering the maximum of the magnetising inductance $max(L_m)$ and defining the threshold $\eta \cdot max(L_m)$ as reported in (4.7).

$$\mu_r^* = \left\{ \mu : L_m(\mu) = \eta \cdot max(L_m)\, \forall\, |I_{s,0}|, B_s, \varepsilon_{ag} \right\} \tag{4.7}$$

The variation of the critical permeability with respect to the *rms* value of the excitation current is proposed in Figure 4.5 considering $\eta = 0.9$ as the threshold value. The analysis of the results permits to identify in $\mu_r^* = 250$ for $|\hat{I}_{s,0}| > 75\,[A]$ the threshold value of relative permeability above which the variation of magnetization inductance L_m is negligible. Therefore we have that

$$L_m(B_s, \mu_r, |I_{s,0}|)\Big|_{\mu_r > \tilde{\mu}_r} \cong L_m(B_s, |I_{S,0}|) \quad \text{for } |\hat{I}_{s,0}| > 75\,[A] \tag{4.8}$$

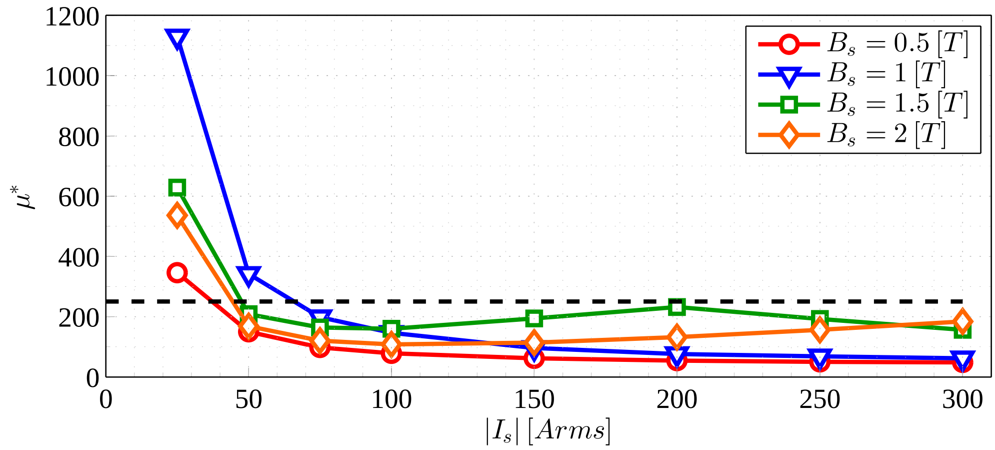

Figure 4.5: Critical relative magnetic permeability μ_r^* against current amplitude. The values of the limit for the critical relative permeability $\tilde{\mu}_r = 250$ is highlighted (- - -).

The value of the magnetising inductance for $\mu_{r,r} = \mu_r^*$ is presented in Figure 4.6 for different current amplitudes highlighting the strong dependency of the parameter on the excitation.

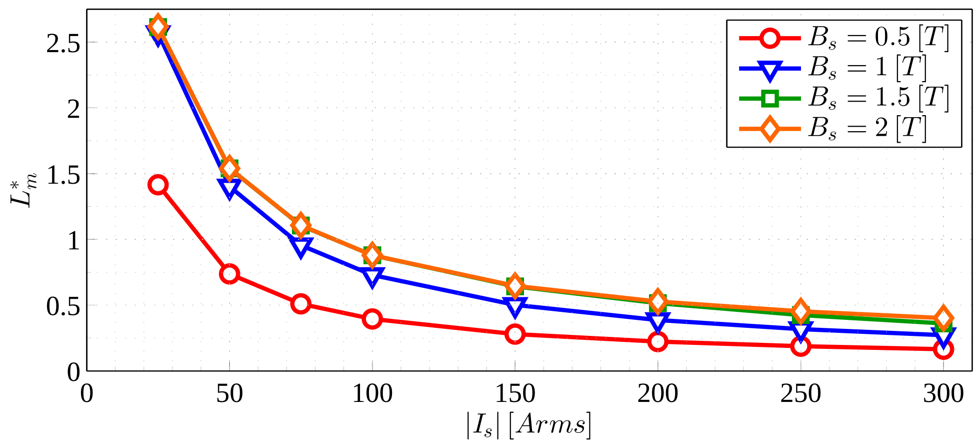

Figure 4.6: Magnetising Inductance $L_m(B_s, |I_{S,0}|)$ against supply current amplitudes for $\mu_{r,r} > \mu_r^*$ and considering various level of saturation flux density

The dependency of the magnetising inductance with respect to the saturation flux density B_s is worthy of investigation as suggested by the previous analysis and summarised in Figure 4.6. The magnetising inductance is proposed in Figure 4.7 and Figure 4.8 against different saturation level amplitudes.

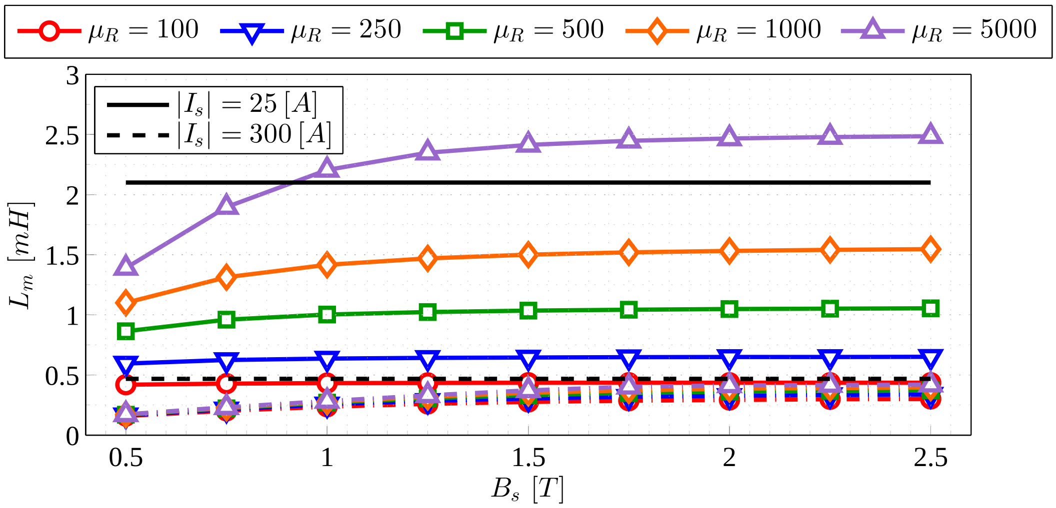

Figure 4.7: Magnetising inductance $L_m(B_s)$ for excitation amplitude $|\hat{I}_{s,0}| = 300\,[A]$ (dashed line) and $|\hat{I}_{s,0}| = 25\,[A]$ (solid line) considering different $\mu_{r,r}$ values. The lines in black correspond to the HSIM parameter value.

The trend of the computed parameters enables consideration of the critical saturation flux density B_s^* as a characteristic index of the no load parameters as introduced above for what concerns the relative permeability dependency. The critical saturation flux density B_s^* is determined by means of (4.9) and establishes the saturation level above which the magnetising inductance is not subject to significant variation.

$$B_s^* = \left\{ B_s : L_m(B_s) = \eta \cdot max(L_m)\, \forall\, |I_{s,0}|, \mu_r, \varepsilon_{ag} \right\} \tag{4.9}$$

The threshold parameter is considered as $\eta = 0.9$ and the critical saturation flux density parameter is presented in Figure 4.9. The result suggests that the trend of the magnetising inductance for $B_s > \tilde{B}_s$ considering $\tilde{B}_s \approx 1.15$ do not feature high variations with respect the relative permeability if $\mu_r > \mu_r^*$.

However, the magnetising inductance features a strong dependency upon the current amplitude as suggested by Figure 4.6. In Figure 4.10 the variation

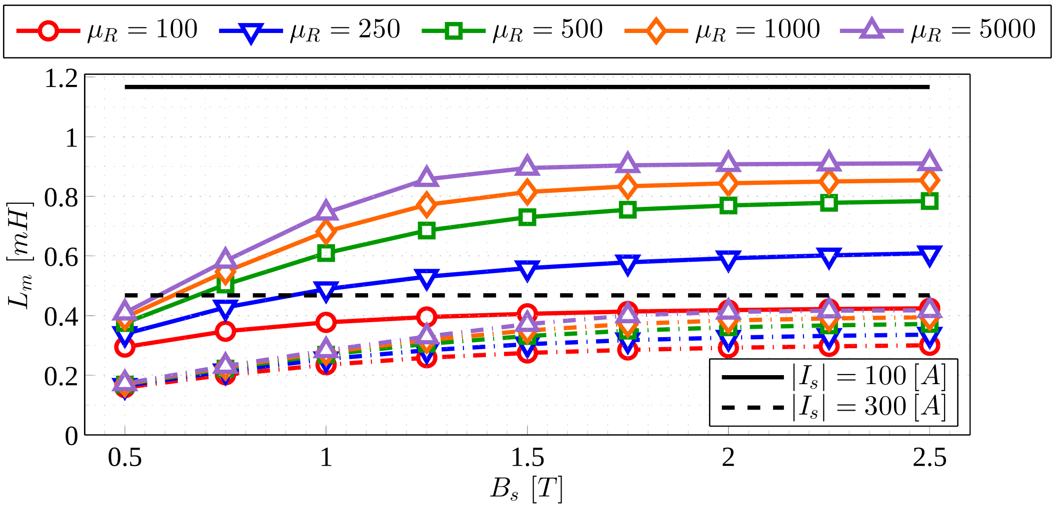

Figure 4.8: Magnetising inductance $L_m(B_s)$ for excitation amplitude $|\hat{I}_{s,0}| = 300\,[A]$ (dashed line) and $|\hat{I}_{s,0}| = 100\,[A]$ (solid line) considering different $\mu_{r,r}$ values. The lines in black correspond to the HSIM parameter value.

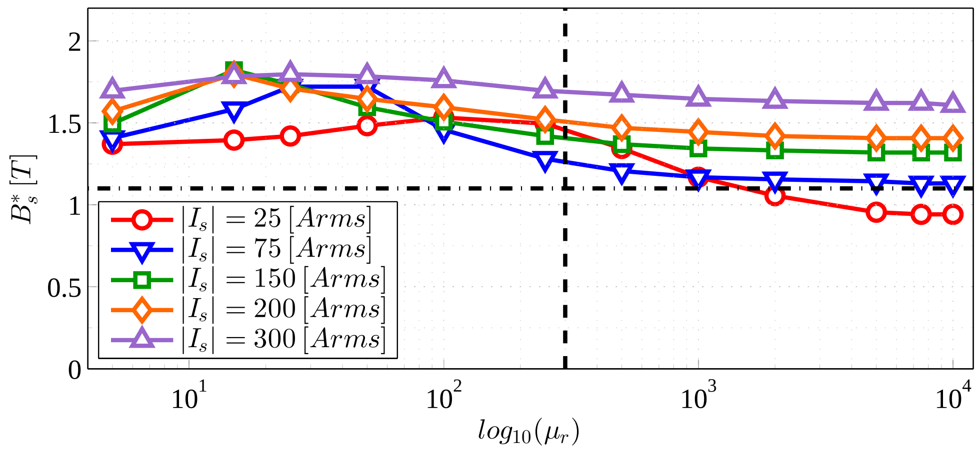

Figure 4.9: Critical saturation flux density B_s^* against relative magnetic permeability. The values of the limit for the critical relative permeability $\mu_r^* = 250$ (- - -) and critical limit saturation flux density $\tilde{B}_s = 1.15\,[T]$ (-·-·) are highlighted.

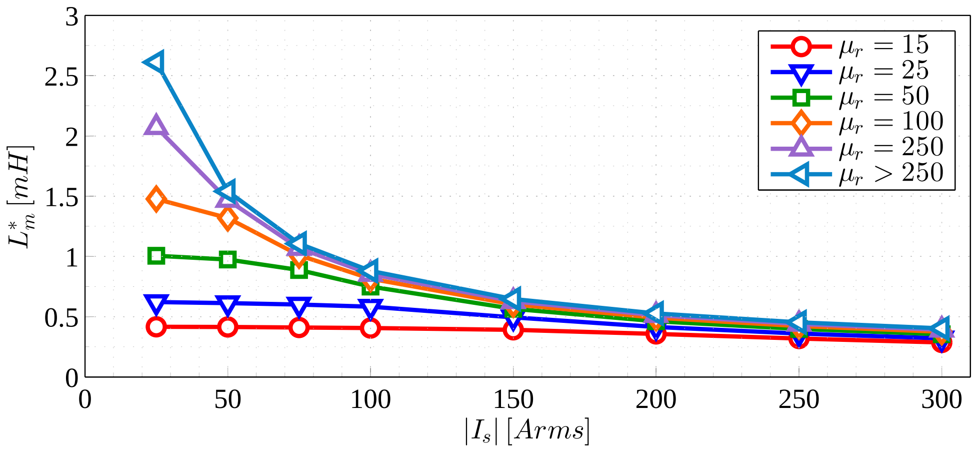

Figure 4.10: Magnetising inductance dependency with respect excitation current

of the magnetising inductance against the no load current is proposed for $B_s = B_s^*$. The results confirm the previous consideration as for $\mu_r > 250$ we have very small variation in the trend of $L_m(|I_{s,0}|)$. In general, we have that the curve which represent the magnetising inductance for $\mu_r > 250$ and $B_s > 1.15\,[T]$ can be approximated as (4.10) and is adopted in the calculation of the equivalent circuit solution and the computation of the rotor parameters.

$$ {}^{a}L_m(|\hat{I}_{s,0}|) \cong A\, e^{\alpha\,|\hat{I}_{s,0}|} + B\, e^{\beta\,|\hat{I}_{s,0}|} \tag{4.10} $$

4.3.1 Sensitivity Analysis - Load Condition

The rotor parameters are not considered when the representative simulations of the no load condition are performed. The locked rotor test is conventionally adopted to determine and quantify the parameters representative of the rotor in the equivalent circuit. The FE-TH simulations are a powerful tool that can be adopted to investigate the performances of IMs. The characterization of the parameters of the equivalent circuit can be achieved by performing a set of FE-TH to account for the main operative condition point of the device, such as slip and input current. The analysis focus on the range of slip in which the machine features a linear torque characteristic [99]. Applying the *Thevenin* theorem to the nodes A-B of the circuit presented in Figure 4.1, the total equivalent inductance L_{eq} and total equivalent resistance R_{eq} are defined. The parameters of the *Thevenin* equivalent circuit presented in Figure 4.11 are a function of the input current and operative slip.

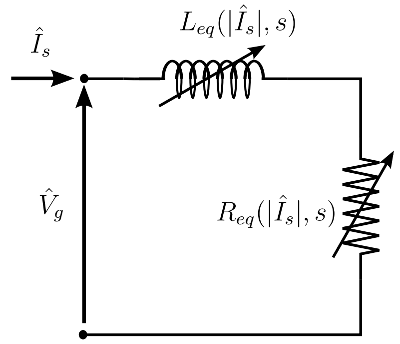

Figure 4.11: *Thevenin* equivalent non-linear single phase steady state circuit for smooth SRIM.

The rotor resistance and rotor leakage inductance are directly linked to the rotor losses and the electromagnetic energy stored in the device, respectively [52]. The equivalence between the impedances of the equivalent circuit and the *Thevenin* equivalent circuit leads to the definition of the rotor resistance and rotor leakage inductance as presented in (4.11) [52, 99]

$$L_{\sigma,R}(|\hat{I}_r, s|) = L_m \frac{\left(L_{eq}\left[L_m - L_{eq}\right] - \left[\dfrac{R_{eq}}{\omega_s\, s}\right]^2\right)}{\left[\dfrac{R_{eq}}{\omega_s\, s}\right]^2 + \left[L_m - L_{eq}\right]^2} \tag{4.11a}$$

$$R_r(|\hat{I}_r, s|) = \frac{L_m^2\, R_{eq}}{\left[\dfrac{R_{eq}}{\omega_s\, s}\right]^2 + \left[L_m - L_{eq}\right]^2} \tag{4.11b}$$

Table 4.2 lists the FE simulation parameters and their range that have been implemented in the rotor parameters sensitivity analysis. Based on the conclusions drawn in the magnetising inductance sensitivity analysis and according to [1], initial relative permeability values $\mu_{r,r} < 250$ are not considered.

Table 4.2: Load sensitivity analysis parameters

Parameter	Min	Max	# Values
$\lvert\hat{I}_s\rvert$ $[A]$	75	300	3
B_S $[T]$	0.5	2	4
$\mu_{r,r}$ $[pu]$	250	2000	7
ρ_R $[\mu\Omega cm]$	20	80	4
$s\,(slip)$ $[\%]$	0.01	$3\% \div 4\%$	25

The rotor resistance against the operative slip for various rotor resistivity values at the operative input current $|\hat{I}_s| = 300\,[A]$ is presented in Figure 4.12 and Figure 4.13, considering flux density saturation level of $B_s = 1\,[T]$ and $B_s = 2\,[T]$, respectively [99] and where the black line present the cage rotor IM rotor resistance.

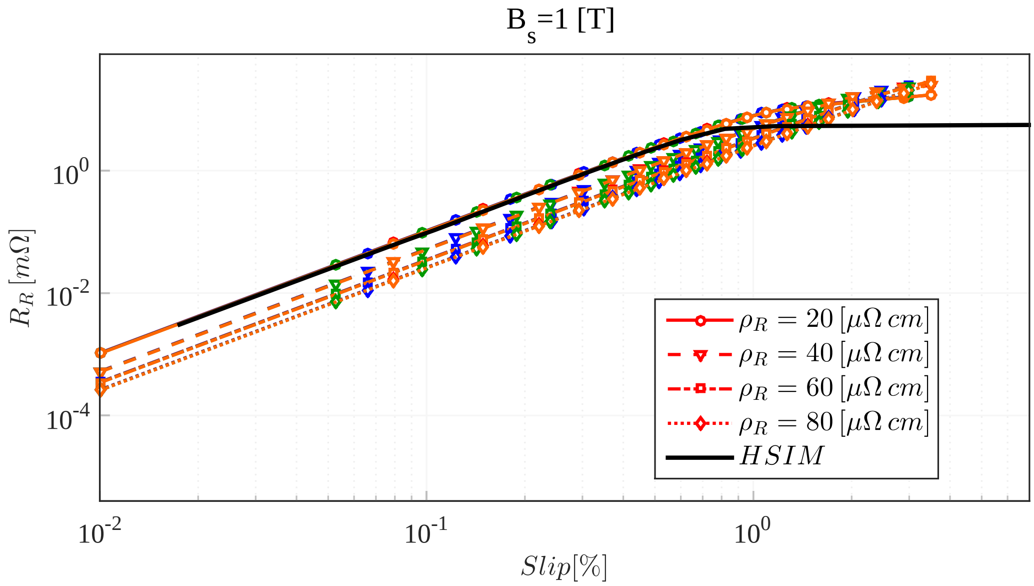

Figure 4.12: Rotor resistance against slip at $\hat{I}_s = 300\,[A]$ and $B_s = 1\,[T]$. The markers are used to distinguish between the different rotor resistivity. Different colours are considered to identify different rotor relative permeability.

The different colours are defined in order to distinguish the various rotor relative permeability considered. However, it is possible to note that the $\mu_{r,r}$ parameter has negligible impact on the rotor resistance which is mainly dominated by the resistivity of the solid rotor material. Increasing saturation flux density have to be related with increasing rotor resistance values. Furthermore, the trend of the rotor resistance for slip values $s \lesssim 1\,\%$ feature a characteristic which can be expressed as ${}^{t}R_R = A\,log(s) + R_0$ where R_0 is the extrapolated value of the resistance at $s = 0$ and A is the slope constant. The parameter A does not features significant variations while R_0 results strongly dependant on the resistivity, saturation flux density and excitation current as presented in Figure 4.14.

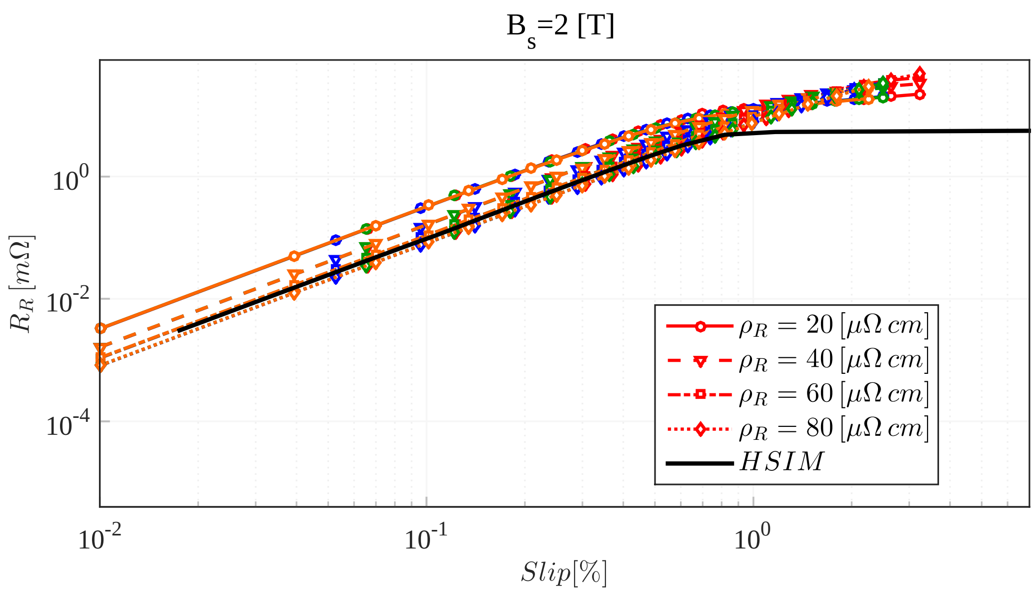

Figure 4.13: Rotor resistance against slip at $\hat{I}_s = 300\,[A]$ and $B_s = 2\,[T]$. The markers are used to distinguish between the different rotor resistivity. Different colours are considered to identify different rotor relative permeability.

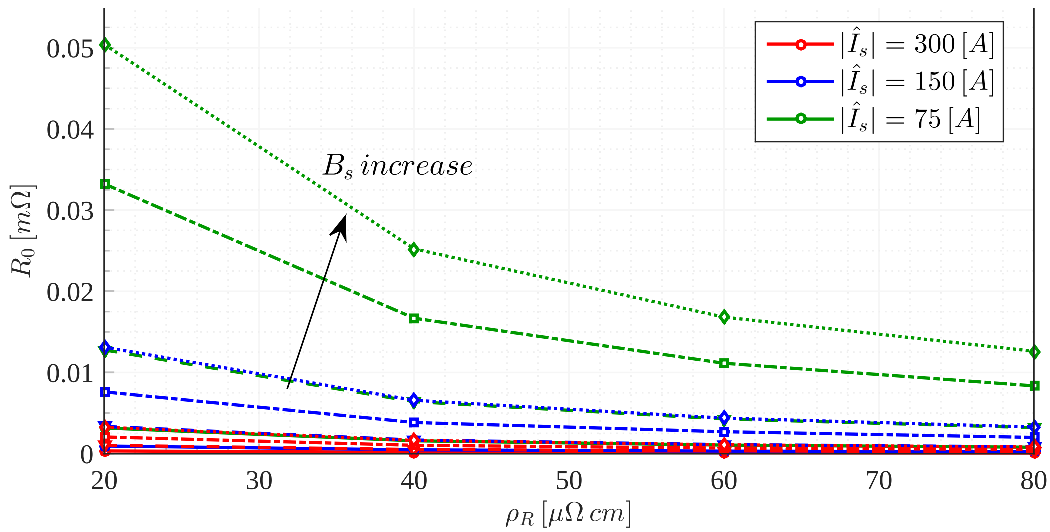

Figure 4.14: Rotor resistance variation with respect the rotor resistivity for different input current and saturation flux densities.

Figure 4.15 and Figure 4.16 present the variation of the rotor leakage inductance with respect the slip for $B_s = 1\,[T]$ and $B_s = 2\,[T]$ respectively.

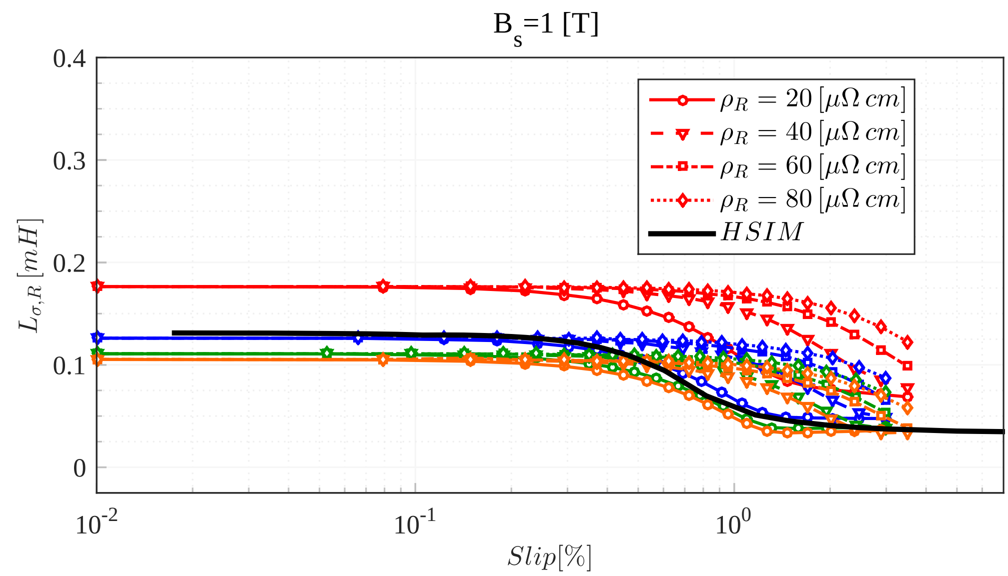

Figure 4.15: Rotor leakage inductance at $\hat{I}_s = 300\,[A]$ and $B_s = 1\,[T]$. The markers are used to distinguish between the different resistivity whilst colours identify the various relative permeability.

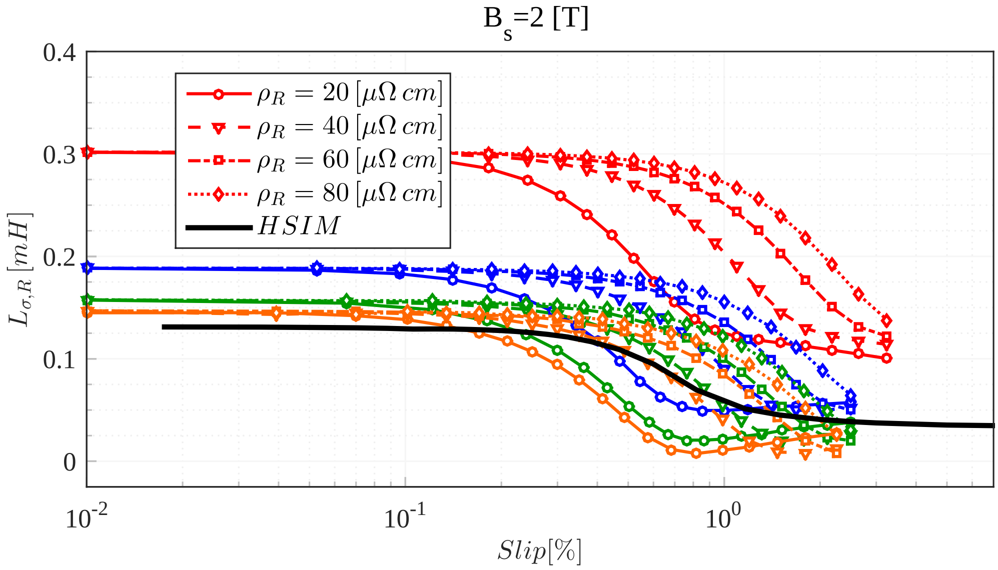

Figure 4.16: Rotor leakage inductance at $\hat{I}_s = 300\,[A]$ and $B_s = 2\,[T]$. The markers are used to distinguish between the different resistivity whilst colours identify the various relative permeability.

The above results are presented for a constant current amplitude of $|\hat{I}_s| = 300\,[A]$. The dependency of the rotor leakage inductance on the parameters which define the rotor material are different with respect to the resistive case. The inductance features a quasi-constant trend for low slip values while significant drop can be observed for lower rotor speed. The impact of the rotor resistivity is negligible at very low slip as can be observed in Figure 4.15 and Figure 4.16. Decreasing values of resistivity cause the inductance drop at higher slip values. This is mainly caused by the fact that the low resistivity induces higher rotor current and therefore early saturation of the material core. The saturation flux density impact on both the inductance saturation slip point as well as on its non saturated value. The latter conclusion is summarised in Figure 4.17. The values of the leakage rotor inductance however tends to be similar each other considering different materials for high excitation current level. The saturation effect is dominant in those condition leading the inductance to drastically drop.

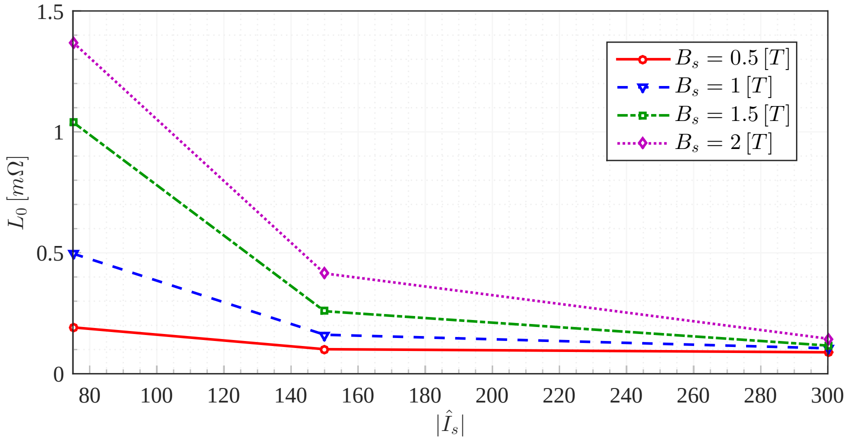

Figure 4.17: Un-saturated rotor leakage inductance variation with respect the excitation current considering different saturation flux density levels.

4.4 Solid Rotor Material

The rotor structure is the media that carries both electric and magnetic fields and in the previous section the effect of the electromagnetic properties of the material on performance has been investigated. Further considerations regarding the output torque and rotor losses can be found in [99]. In fact, both resistivity and permeability in combination with the magnetization curve have to be determined to define the best material for the solid rotor. However, the mechanical properties have to be taken into account since they constitute an important limiting factor on the maximum speed that can be achieved. In Table 4.3 the characteristics of the most promising material selected for SR applications are reported [1].

The bulk of a row material is required to be machined in order to manufacture the rotor structure. The materials featuring high tensile strength, e.g. *Maraging* steel, are expensive and difficult to machine. A good compromise between the mechanical, electromagnetic, availability characteristic can be found in construction steel materials. Their mechanical properties are well documented on the contrary of the electromagnetic characteristics. Further-

Table 4.3: Summary of solid material properties from [1] and material data sheet.

Material	B_s $[T]$	μ_r	ρ $[\mu\,\Omega cm]$	α $[1/K]$	σ_t $[MPa]$	δ $[^{kg}/_{m^3}]$
Maraging	1.9	~ 1000	50	$\sim 4.5^{-3}$	2250	7870
C15	1.9	~ 1000	15.9	$\sim 4.5^{-3}$	440	7870
Fe52	1.9	~ 1000	25.7	$\sim 4.5^{-3}$	520	7870
Vacodur 49	2.3	~ 1000	40	$\sim 4.5^{-3}$	720	8100

more, according to the sensitivity analysis results, the material featuring low electric resistivity is preferred. Considering the materials listed in Table 4.3, the low resistivity comes along with poor mechanical properties.

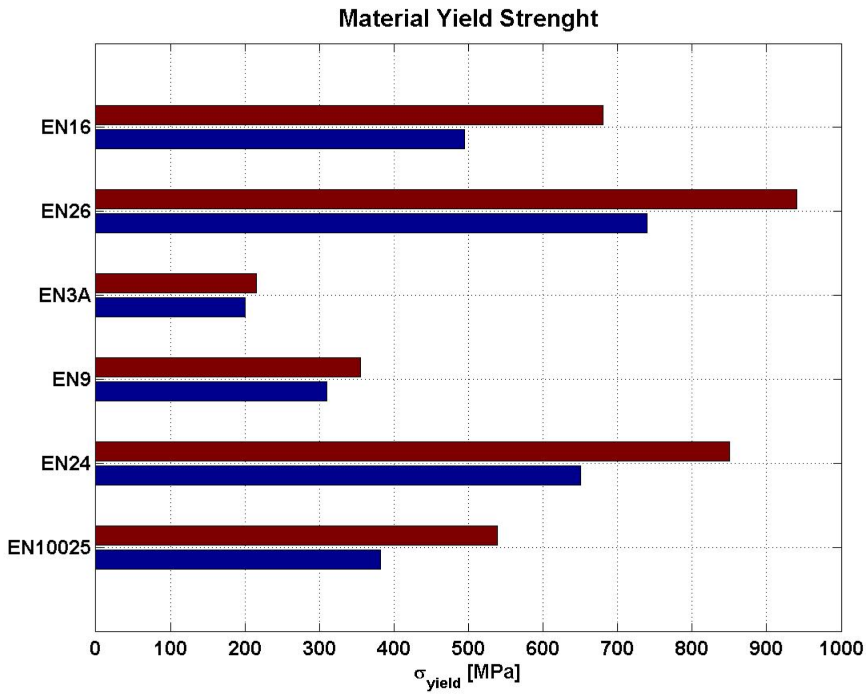

Figure 4.18: Yield strength of construction steel. In red and blue are highlighted the maximum and minimum variation range.

The available database for the electromagnetic characteristic of solid material is small compared to electrical steel. Solid material are mainly adopted for construction and transmission purposes and therefore their characterization focuses on the mechanical aspects. In Figure 4.18 the yield strength of various common construction material is presented according to manufacturer's data sheet. The analysis on the mechanical stress on the rotor summarised in Figure 3.10 shows that the maximum peripheral speed of $v \approx 350\,[^m/_s]$ can be achieved selecting $EN24$, which translate in $\omega_m \approx 75\,[krpm]$ for a rotor radius of $r_R = 45\,[mm]$ considering a safety factor $\kappa_\sigma = 2$ featuring full rotor structure and a rotor dynamic safety factor of $\kappa_{rd} \approx 5$. The operative speed of the machine can be increased to $\omega_m = 40\,[krpm]$ considering a safety factor $\kappa_{rd} = 9.5$ with respect the first critical frequency of the system and remain limited by the second rigid mode which occurs in proximity of the maximum speed imposed by the mechanical properties.

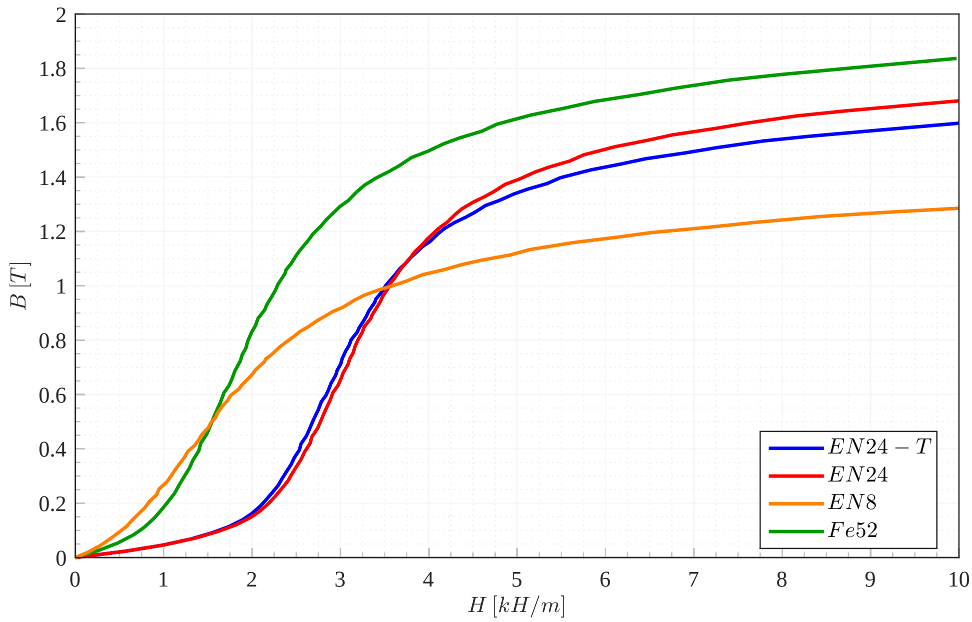

Figure 4.19: Measured DC B-H characteristic

In order to compensate for the lack of data available on the magnetic characteristic of construction steel, a state of art testing facility that is available in-house was used to characterize samples of solid rotors materials. The normalized magnetization curve is assumed to be representative of the rotor material behaviour for low operative slip as the frequency of the electromagnetic field in the rotating element is small. A selection of solid steel grades is considered and toroidal samples have been manufactured. In Figure 4.19 the measured magnetisation curves for the solid materials are presented.

Only combining the mechanical properties Figure 4.18 and the electromagnetic characteristic Figure 4.19 of various construction steel, the rotor material is selected. $EN24$ and $EN24-T$ presents similar magnetic characteristic while the mild steel grade $EN8$ features low saturation flux densities. The magnetisation curve of $Fe52$ is also presented and the experimental data confirm the values proposed in literature. $EN24$ features electrical resistivity of $\rho \approx 20[\mu\Omega\, cm]$ [178], saturation flux density of $B_s = 1.65\,[T]$ with $\mu_{r,r} > 500$. The material is selected as a good compromise between the mechanical properties and electromagnetic characteristics required for SRIM applications.

4.5 Summary

The chapter provided a complementary analysis to the multi-physics tool presented in Chapter 2. The performances of SRIM are affected by the environmental conditions such as the temperature distribution. Furthermore, the strong impact of the electromagnetic properties of the rotor material is demonstrated by the equivalent circuit parameter sensitivity analysis. Low resistivity values for the rotor material lead to high output torque, although associated with high rotor losses, which require an increased effort in the thermal management aspects. The impact of the relative permeability for $\mu_{r,r} > 250$ is negligible in both magnetising and rotor parameters. The saturation flux density strongly affects the parameters of the equivalent circuit allowing higher field and consequently high output torque. The intricate dependency of the equivalent circuit parameters with respect to the electromagnetic properties of the material above discussed, confirm the need of full characterisation of the non-linear equivalent circuit in order to improve the calculation accuracy. The DC-magnetisation curve measurement of construction steel is presented in order to determine their feasibility for SRIM application. Comparing the caged rotor IM equivalent circuit parameters and considering a range of available materials, the $EN24$ is selected as the candidate to achieve a reliable, economical yet performing technological alternative.

CHAPTER

FIVE

MODEL VALIDATION AND COMPARISON

The analytical and numerical approaches for the analysis of SRIM are discussed in Chapter 2 and Chapter 3. The end region correction factor has been introduced aiming to account for the intrinsic three-dimensional nature of the field distribution when considering simplified bi-dimensional models. In order to validate the 2-D TH-FE prediction, the bi-dimensional model of the SRIM has been extended in the three-dimensional domain. The high computational time required for the convergence of non linear TH 3-D simulations limits their application only at the validation stage. A fine mesh grid is required on the rotor surface to accurately compute the effects of high order space harmonics. Solid rotor material featuring low electrical resistivity, high saturation flux density and initial relative permeability > 250 are suitable for the application as discussed in Chapter 4. Furthermore, the mechanical aspects, material and manufacturing cost play an important role when comes to the material selection. SRIM equipped with $EN24$ is therefore modelled and 3-D FEA is considered to validate the performance prediction.

Furthermore, the SRIM considered is benchmarked against the cage rotor IM machine. The assessment of the variation in the performances between the caged structure and the solid rotor is achieved considering the same power-speed node defined by the application. The structural limitations that constrain the rotational speed of the caged IM at $32\,[krpm]$ do not stand for the smooth solid structure. However, the stator structure is designed to operate at the rated electrical frequency of the caged rotor IM and therefore high losses occur when increasing the operative speed of the machine.

The rotor structure is demonstrated as being mechanically robust according to the analytical calculations. A wide operative speed range has been predicted according to the rotor dynamic analysis. A bump test is performed on a prototyped rotor with the aim to assess the validity of the computations. Furthermore, the vibrations level in high speed applications can cause severe damages and therefore fine balancing tolerances have to be reached for the manufactured structure.

5.1 Model Validation

In order to validate the analytical and 2-D FE calculation, the three-dimensional field distribution is computed using 3-D FEA. The technique is known as the most accurate analysis tool to achieve good performance prediction. The end-winding structure has been neglected and therefore no interaction between the rotor and stator structure is assumed as can be observed in Figure 5.1.

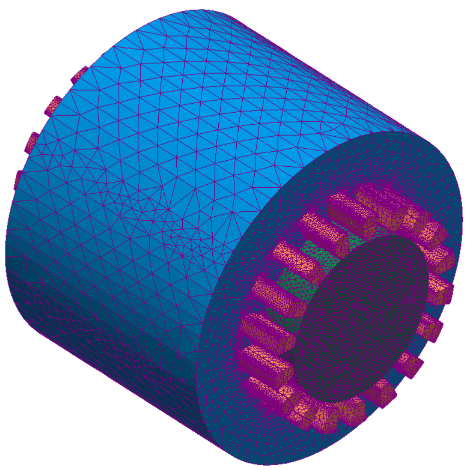

Figure 5.1: Three-dimensional FE computational mesh.

The geometrical dimension of the machine are listed in Table 1.2 and Table 2.2. The *rms* fundamental magnetisation curve of the material is computed according to the data presented in Figure 4.19. Two different rotor axial lengths are considered featuring small and large over length. The end region lengths selected are $\ell_{er} = 5\,[mm]$ and $15\,[mm]$, resulting in $\ell_R = 160\,[mm]$ and $\ell_R = 180\,[mm]$, respectively. The rotor resistivity for the three dimensional calculation is considered ${}^{3D}\rho_R = 25\,[\mu\Omega cm]$ and the non linear simulations are performed for a synchronous rotor speed of $32\,[krpm]$. In Table 2.1 a review on the end region factor is presented and its important to highlight that most of these parameters do not depend on the operative slip of the machine.

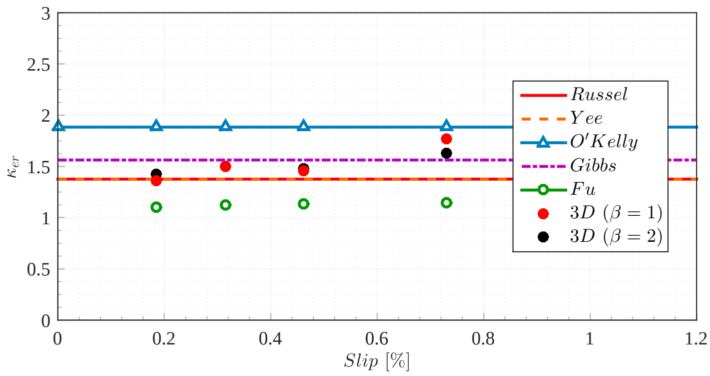

(a) Axial rotor length $\ell_R = 160$

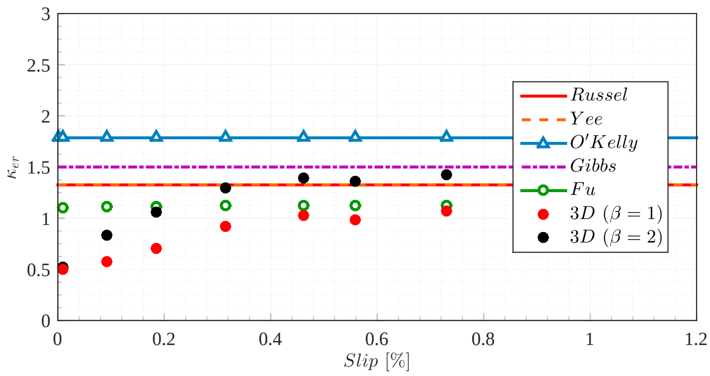

(b) Axial rotor length $\ell_R = 180$

Figure 5.2: Comparison of literature review end region correction factor κ_{er} and 3-D FE calculations.

The equivalent resistivity is computed by means of (2.48). The end region factor κ_{er} is the key parameter to be considered in order to validate the model.

The correction factor can be computed considering the total power losses of the machine in both bi- and tri-dimensional domain. The parameter β has been introduced in Chapter 2 to account for the different options proposed in literature. According to (2.48), the end region factor for both $\beta = 1$ and $\beta = 2$ is presented in Figure 5.2a and Figure 5.2b considering $\ell_r = 160\,[mm]$ and $\ell_r = 180\,[mm]$, respectively. The end region coefficient from the literature are also presented in order to assess their validity. The results highlight two main aspects. Considering smooth solid rotor structure, the correction coefficient applied by means of $\beta = 2$ is demonstrated more effective.

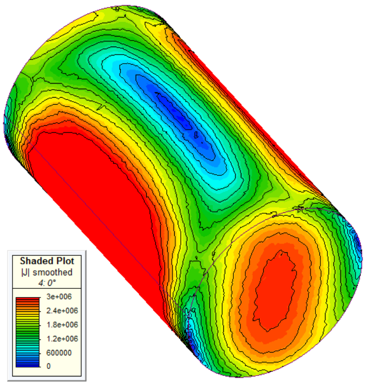

(a) Rotor 3-D view ($\ell_r = 160$)

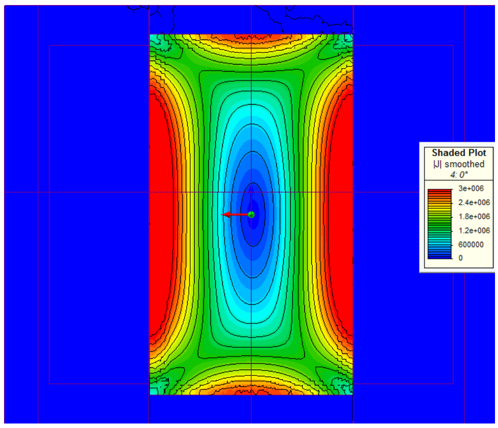

(b) Axial cross section view ($\ell_r = 160$)

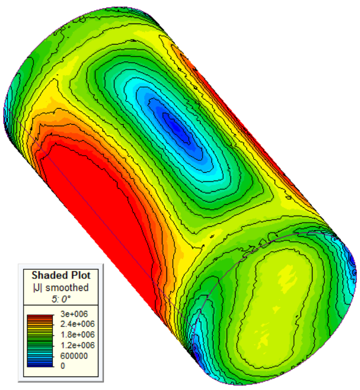

(c) Rotor 3-D view ($\ell_r = 180$)

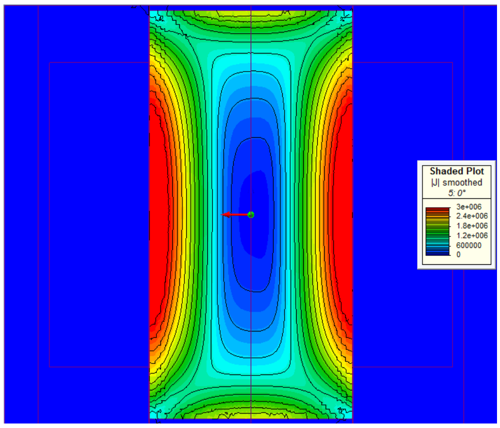

(d) Axial cross section view ($\ell_r = 180$)

Figure 5.3: Eddy current density distribution in the rotor structure for $s = 0.5\%$, $I_s = 300\,[A]$. The 3-D view and the axial cross section are presented for both $\ell_r = 160$ and $\ell_r = 180$ rotor axial length.

Moreover, the dependency upon the slip characterises the end region factor for long rotor structure. The eddy current distribution within the rotor structure along its axial development presented in Figure 5.3 highlights the differences between the models investigated. The eddy current in the end region is more intense and concentrated within the over length region for the short rotor structure as highlighted in Figure 5.3a. Furthermore, the comparison between the eddy currents in the stator-rotor overlap region between Figure 5.3b and Figure 5.3d shows how the axial length is more evenly covered when the rotor features long ferromagnetic end region.

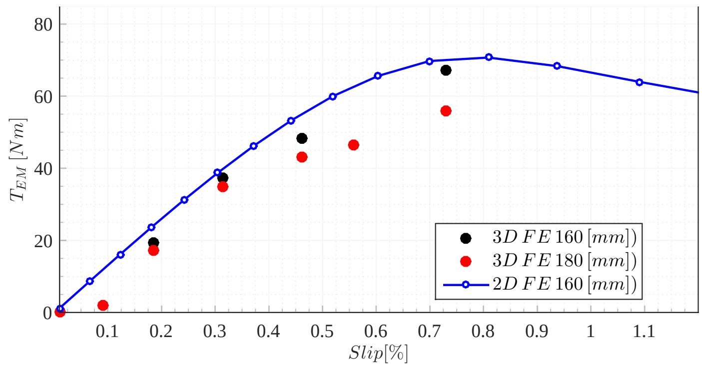

(a) SRIM output torque against slip.

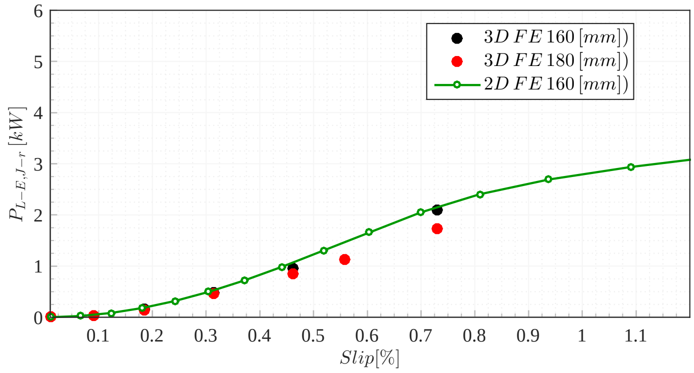

(b) SRIM power losses against slip.

Figure 5.4: Comparison of 2D output torque and rotor eddy current losses against the 3D case study considered.

Finally, the comparison of torque and power losses between the bi-dimensional and the two 3-D FE solutions is presented in Figure 5.4. The rotor resistivity used in the bi-dimensional computations have been modified by means of the end region correction factor, in particular the *Gibbs* end region factor is used as the more accurate in predicting the rotor losses according to Figure 5.2. The result enables the conclusion that the shorter rotor structure leads to higher output torque although also featuring higher rotor losses.

5.2 Air gap thickness selection

The performances of SRIMs, as for most electrical machines, are very sensitive to the air gap thickness. The clearance between the stator and the rotor is selected in order to maximise the mechanical output and minimise the losses. The mechanical to electrical (or vice versa) energy transformation in rotating electrical machines take place mainly in the air gap. The thickness of the clearance has a strong impact on the harmonic content of the flux density distribution. Analytical formulations have been validated [179] and demonstrate the filtering effect of the air gap on the order field harmonics. The high space harmonic order of the flux density in the air gap does not strongly impact on the torque generated thus affecting the losses generated in the rotor. The rotor losses, in particular the rotor surface losses, are significantly dependant on the harmonic content of the electromagnetic field in the air gap (see *Chapter* 2) and their minimisation leads to increased efficiency of the machine.

Analytical formulations have been proposed [65, 85, 180] to select the optimum air gap length for a given power-speed node. In particular, [85] presents a formulation where the clearance thickness is a function of the rotor diameter and the peripheral speed of the machine. An increased clearance is selected in high speed applications in order to achieve high efficiency. The eddy current and friction losses are an important component of the losses in high speed application and results are inversely proportional to the size of the air gap [85]. The eddy current rotor loss minimisation is the main aspect to be accounted in a high speed solid rotor induction machine [85, 90]. The high order space harmonics introduced by the stator structure are filtered by the increased air gap length. In Figure 5.5, the selected air gap against the rotor speed of high speed induction machines results that can be found in literature are presented.

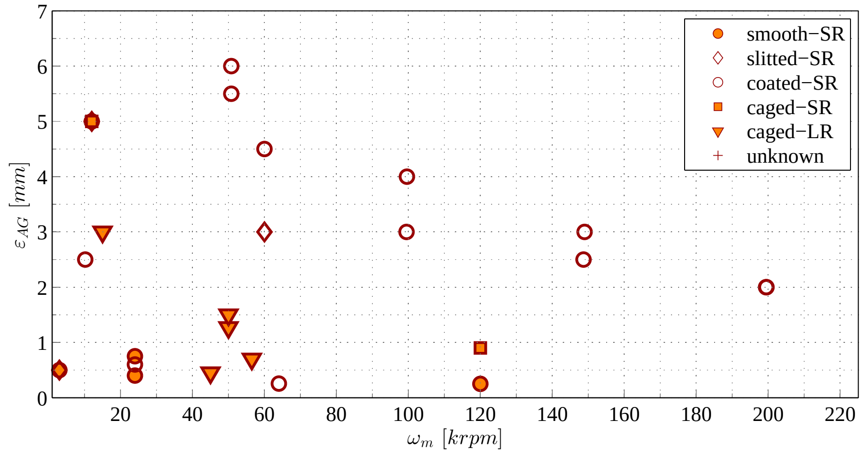

Figure 5.5: Aig gap (ε_g) against speed (ω_m) for IMs topology from literature.

The selection of the air gap thickness is performed evaluating the rated slip of the machine for a given output power. The related eddy current and air friction losses are calculated and the clearance which minimises the above is considered. It is important to highlight that the air gap thickness affects the rotor outer diameter having the stator structure fixed. The output power is presented in Figure 5.6a. The operative slips are highlighted and considered to identify the losses level in Figure 5.6b. The calculation are performed for a fixed rotor temperature of 200 $°C$

The results suggests that the minimum slip is achieved considering the minimum air gap clearance. The increase in the air gap thickness leads to a reduction of the rotor losses and friction losses, however affecting the output power of the machine. In order to minimise the rotor eddy current losses, the clearance of $\varepsilon_g = 1\,[mm]$ is therefore selected. The optimisation of the air gap clearance for SRIM without fixed stator structure and fixed axial length would lead to higher air gap clearance as can be seen in Figure 5.5. Furthermore, is important to highlight that the slotting space harmonic can be reduced adopting semi-magnetic slot wedge on the stator slot opening [119]. The slot wedge geometry might affect the air friction losses and therefore have to be accurately designed in high speed applications.

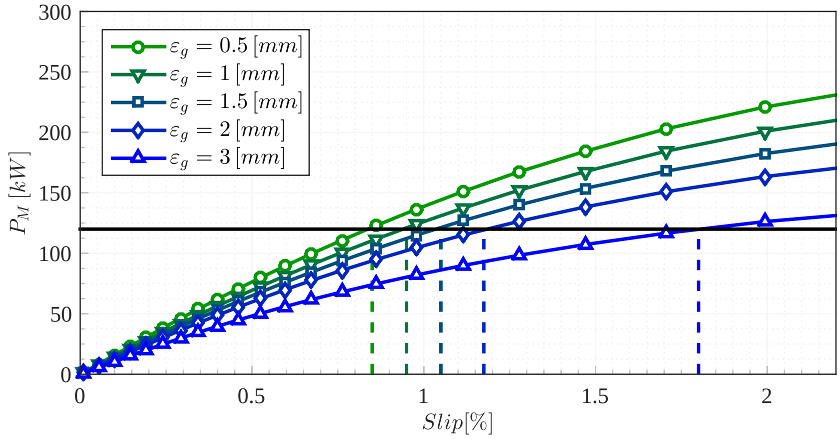

(a) Output power against slip

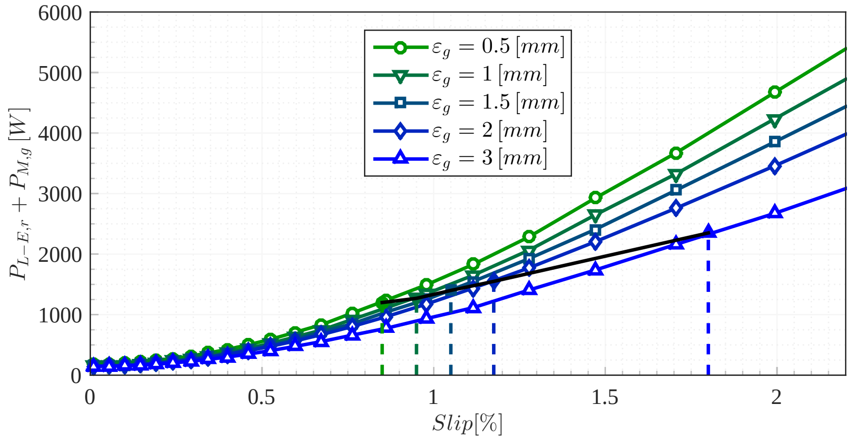

(b) Eddy current and air friction losses against slip

Figure 5.6: Air gap thickness sensitivity analysis for SRIM featuring inner stator bore $r_S = 45.6\,[mm]$ at $\omega_m = 32\,[krpm]$ equipped with $EN24$ rotor.

5.3 Rotor dynamic validation

The validation of the predicted rotor dynamic characteristics is performed by means of bump test. The rotor structure is seated suspended on elastic supports as presented in Figure 5.7.

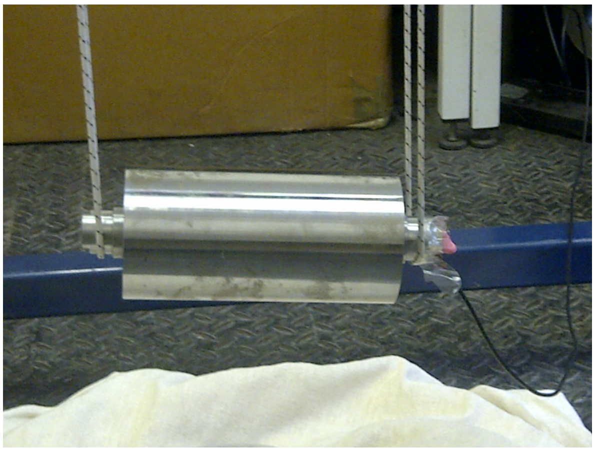

Figure 5.7: Test set-up for bump test on prototyped solid rotor.

The vibrations caused by hammering the rotor excite its natural modes that can be therefore detected by means of accelerometers. Furthermore, the residual noise level emitted by the structure is a good indicator of the modes that are excited. In Figure 5.8a and Figure 5.8b the bump test results are presented. The predominant frequency level excited are highlighted and result at $8030\,[Hz]$ and $13630\,[Hz]$.

The *Campbell Diagram* of the system is computed according to the model proposed in *Chapter* 3 and is presented in Figure 5.9. The predicted natural frequencies match with the measured values presented in Figure 5.8 and the critical frequencies related with the bending modes are highlighted with solid horizontal lines.

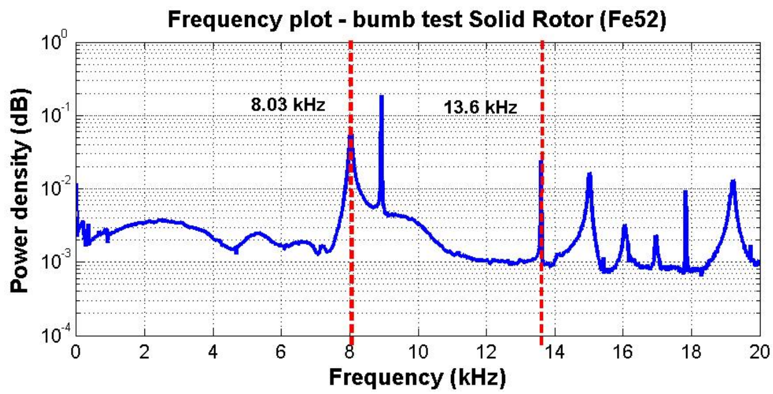

(a) Frequency plot of accelerometer signals.

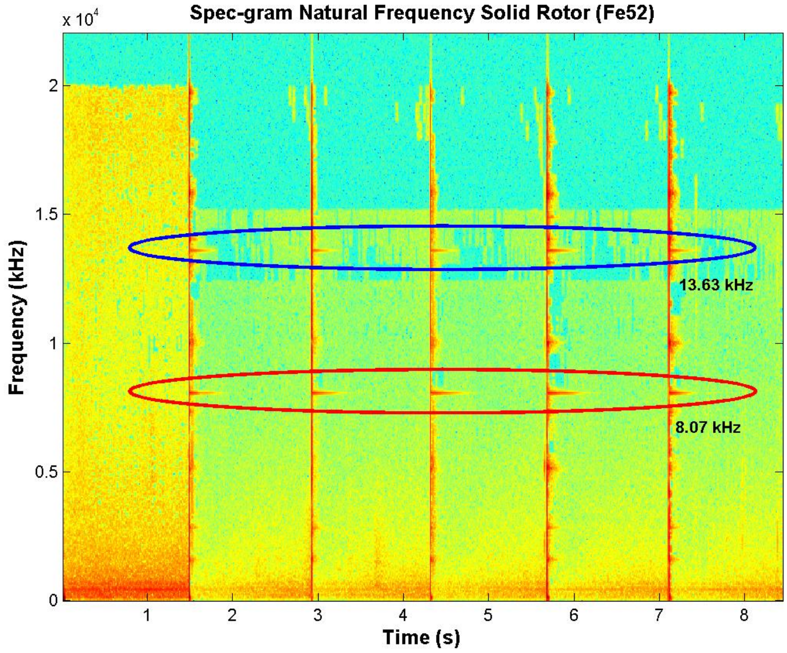

(b) Recorded sound spectrogram.

Figure 5.8: Bump test results. The frequency spectrum of the output signal of the accelerometer is presented together with the spectrogram of the recorded sound level.

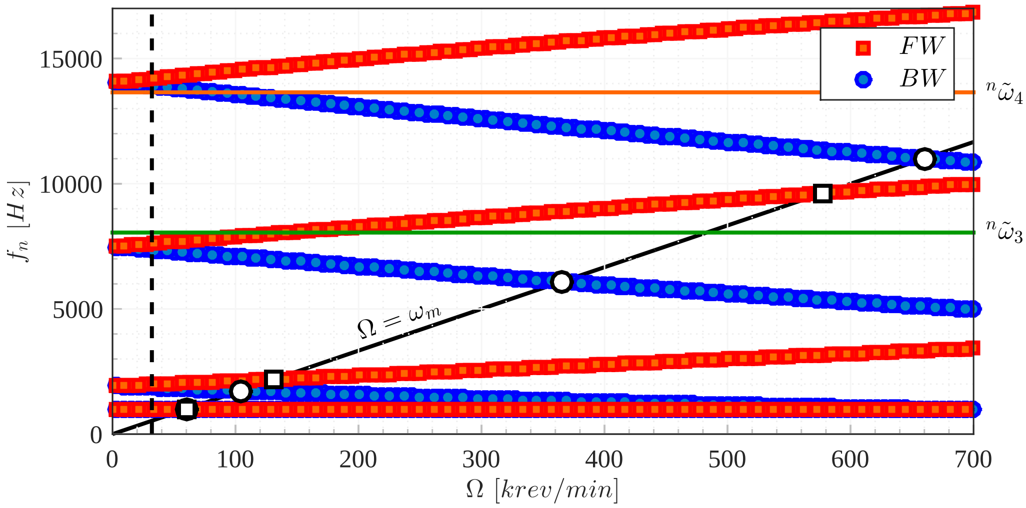

Figure 5.9: Campbell diagram for SRIM considering $\kappa_b = 150\,[^{MN}/_m]$. The green (—) and orange (—) solid line represents the measured natural frequencies of the system. The vertical dashed line (- - -) indicates the rotation speed of $\omega_m = 32\,[krpm]$.

5.4 Rotor balancing

The rotors of high speed machines require fine balancing in order to avoid excessive vibrations. The unbalances introduced in the manufacturing process are compensated by removing mass from the end region of the structure or dedicated balancing planes selected at the design stage. The standards define the criteria to select the balancing levels. A 2 plane balancing procedure has been performed on the solid rotor prototyped. The total maximum permissible residual unbalance $\mathcal{U}_{per}$ can be determined by

$$\mathcal{U}_{per} = 1000\,\frac{(e_{per}\,\Omega_m)\,M}{\Omega_m} \tag{5.1}$$

where M$[kg]$ is the rotor mass, $\Omega_{\mathrm{m}}[^{rad}/_s]$ is the service speed and $(\mathrm{e}_{\mathrm{per}}\,\omega_{\mathrm{m}})[^{mm}/_s]$ is the selected balance quality grade. The symmetry of the structure with respect the center of mass defines the maximum permissible residual unbalance for each plane to be identical and $\mathcal{U}_{per,P}$ amounting at half the total maximum permissible residual unbalance.

Table 5.1: Permissible Residual Unbalance Value for each plane. In brackets the value of $\mathcal{U}_{per}$ is presented.

G	**Speed** $\omega_{\mathrm{m}}[krpm]$	$\mathrm{e_{per}}[g \cdot mm/kg]$	$\mathcal{U}_{\mathrm{per}}[g \cdot mm]$
2.5	35	0.7	6.1388 (3.0234)
	50	0.5	4.2972 (2.11635)
1	35	0.28	2.4555 (1.20935)
	50	0.2	1.7189 (0.84655)

In Figure 5.10a the steps performed to achieve the $G1$ balancing level are shown and Figure 5.10b presents the detail of the final balancing grade achieved.

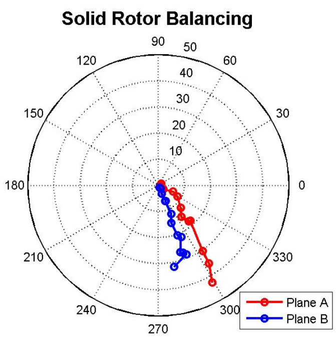

(a) Solid rotor prototype balancing steps.

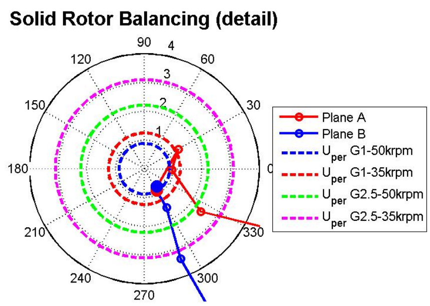

(b) Solid rotor final balancing level detail.

Figure 5.10: Solid rotor balancing procedure.

5.5 Comparison between solid rotor and cage rotor high speed machine

The analysis performed in the previous chapter enables the selection of the rotor structure suitable to challenge the cage rotor induction machine. The $EN24$ solid rotor structure featuring $160\,[mm]$ axial length model is therefore considered. FE analysis has been performed for both structures. In Chapter 3 the rotor parameters together with the magnetising inductance have been compared with the solid rotor ones. Both solid rotor and cage rotor structures are presented in Figure 5.11.

(a) cage rotor structure.

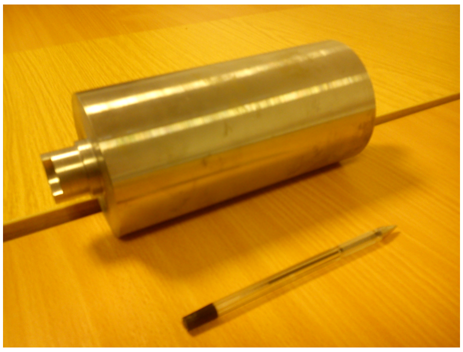

(b) Solid rotor.

Figure 5.11: Cage rotor and solid rotor prototype for high speed applications.

The 120 $[kW]$ power node is the design point of the cage rotor induction machine (HSIM) operating at rotor temperature of 200 $[°C]$. The cage rotor structure is superior in output power level and efficiency with respect to the SRIM. However, the design point of the HSIM is selected in order to enable mechanical integrity. Higher rotational speed would cause damage to the rotor structure whilst the SRIM could be operated at higher rotational speed. The material stress is more of a limiting factor than the rotor dynamics aspects and the HSIM could be therefore operated just below 75 $[krpm]$. In Figure 5.12, the power against slip curve at constant input current for the different machine topologies and the SRIM operating at 75 $[krpm]$ is presented. The operative slip results as $s = 0.46\%$ for the HSIM while $s = 1.05\%$ defines the operative point of the SRIM operated at 32 $[krpm]$.

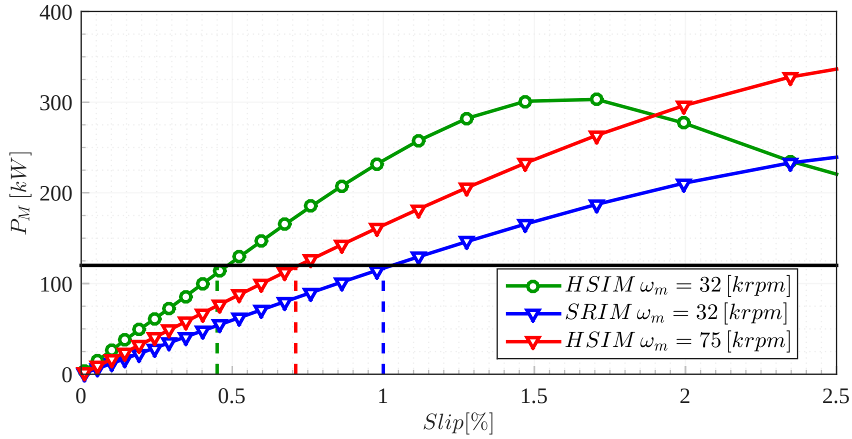

Figure 5.12: Power against slip of both solid rotor and cage rotor induction machine. The dashed line is presented to highlight the 120 $[kW]$ power level.

The SRIM operated at higher rotation speed enables exploitation of the benefits arising from the simple rotor structure, reaching peripheral speed of $\approx 350\,{}^{m}\!/_{s}$. In Table 5.2 the comparison of the SRIM and HSIM is presented. The bi-dimensional calculations are performed with *Gibbs* end region correction factor for the solid rotor induction machine. The reduced performances of the solid rotor induction machine with respect the HSIM are clear considering both the same operative speed and the higher one. However, the solid rotor induction machine is capable to operate at rotating speeds which are prohibitive for the laminated structure. According to the rotor dynamics considerations, the bearing stiffness has to be selected in order to avoid operation around the first critical speed. The reduction of the stiffness leads to reduced first critical speed and the rotor can be operated in super-critical conditions. Alternative solutions can be considered as the increase of the bearing stiffness to move the first critical speed to higher values with respect the maximum speed or the adoption of magnetic bearings. The rotor, stator and bearing losses management at high rotational speed have to be challenged with active magnetic bearing systems, air gap direct cooling and more complex rotor structures. Slitted solid rotor, rotor structure featuring copper coating and solid rotor with rotor bars have been presented in Chapter 1 as the main structures proposed to compensate the existing differences in the performances between the HSIM and induction machines equipped with solid rotor.

Table 5.2: Induction Machine Comparison

		HSIM	**SRIM**-32	**SRIM**-75
Shaft Power	$[kW]$	120	120	120
Torque	$[Nm]$	36	36.2	15.3
Supply frequency	$[Hz]$	533	533	1250
Rotation Speed	$[rpm]$	31853	31664	74460
Slip	[%]	0.46	1.05	0.72
Rotor diameter	$[mm]$	45	44.6	44
Rotor length	$[mm]$	150	160	160
Air gap length	$[mm]$	0.6	1	1.6
Peripheral speed	$[m/s]$	150	148	343
Losses	$[W]$			
Stator		2762	2762	2762
Rotor		573	1355	2662
Windage		183	173	1608
Efficiency	[%]	97.1	96.4	94.1

5.6 Summary

The validation through three dimensional finite element of the electromagnetic calculations of solid rotor induction machines is presented. The end region factor is commonly adopted to account for the three dimensional effect while considering a bi-dimensional computational domain. The various end region factors found in literature do not enable to account for the parameter with respect the operative slip. The calculation performed shows that for large rotor over length, the end region factor is strongly dependant with the slip. The selection of rotor material, rotor length and air gap length is discussed. The characteristic of a 120 $[kW]$ laminated rotor induction machine compared with the solid rotor induction machine designed for the same power rating is presented. The effect of the operative temperature and the high rotor losses levels makes the solid rotor structure non competitive for the selected power-speed node. However, the rotor dynamic and mechanical considerations highlight that the operative speed of the machine can be increased up to 75000 $[rpm]$ by adopting solid rotor structures. The poor efficiency comes along with operation at rotational speeds which are prohibitive for the other machine topologies. The mechanical robustness of the structure enable the integration of the machine with compressor and high speed turbines taking advantage of the capabilities to operate in high temperature, corrosive environments. Whilst the performances are somewhat inferior, solid rotor technologies are very attractive considering the huge manufacturing and mechanical and rotor-dynamic advantages. The higher rotor losses are manageable selecting particular cooling techniques and by correct selection of materials and design parameters. Innovative materials, more advanced manufacturing techniques and the investigation of alternative structure as presented in *Chapter* 1 are some of the aspects which require more research effort in order to improve the electromagnetic performance of SRIM. The gain in being able to increase speed is very attractive for many applications and solid rotor induction machines are able to operate above the speed limits of the other electrical machines topologies.

CHAPTER

SIX

CONCLUSION

The thesis focuses on the multi-physics aspects of high speed solid rotor induction machines. The trends and limitations of the high speed technology have been initially discussed. The mechanical, thermal, structural, and rotor dynamic solutions currently adopted have been presented and compared. The technology limits have been proposed highlighting the main challenges in pushing the boundaries of high speed electrical machines. The mechanical robustness of induction machines makes them suitable for high speed applications. Among all the different topologies, solid rotor induction machines have been found capable of peripheral speed which exceeds 400 $[m/s]$. The design of high performance high speed solid rotor induction machines requires a multi disciplinary approach. The thermal and mechanical aspects strongly impact on the electromagnetic performances of the device. A flexible multi-physics environment has been developed. The discrete domain method is presented in this thesis as a computationally efficient solution to characterise solid rotor induction machines accounting for high space-time harmonic orders. Based on the discretisation of the computational domain, thermal and mechanical models have been developed. The finite difference approach is used to compute the temperature distribution in the solid rotor and stator core; multi-layer model is presented to account for non homogeneous rotor structures. The proposed models feature temperature dependent material properties. The models of the different disciplines are linked in a flexible multi-physics environment that enables to account for the interaction between the phenomena which occur in high speed machines. The model proposed can be adopted for a wide range of purposes, from the analysis of different machine topologies (i.g. permanent magnet machines) to the mechanical design of retaining sleeves for high speed machines.

The multi-physics approach presented relies on the general solution of the equations that govern the physics of the various phenomena considered. Mainly bi-dimensional models are presented while the three-dimensional effect might strongly affect the accuracy of the calculations. Furthermore, by means of numerical-analytical solutions, only linear material behaviour can be considered. The details and tuning of the models is still required to achieve good predictions with respect non linear bi/three-dimensional FE solutions. The methodology proposed has to be considered the base of further activities aiming to overcome the limitations highlighted in combination with further generalisation aiming to extend the approach to a wide variety of electrical machine topologies.

The non linear electromagnetic characteristic of solid materials required a separate investigation. The impact of the electromagnetic properties of solid material applied to solid rotor technologies is presented. The dependency of the equivalent circuit parameters with respect to the material properties is discussed based on the finite element simulations performed. General guidelines for material selection have been found and the characteristics of construction steel are presented.

The accuracy of bi-dimensional field calculations applied to solid rotor induction machines relies on a correction factor to account for the effect of the intrinsic three-dimensional field distribution. The validation of the correction factor is presented. The computation of the three dimensional field distribution by means of finite element highlights the dependency of the correction factor with respect to the operative slip. The rotor structure of a $120\,[kW] - 25000\,[rpm]$ laminated rotor induction machine is replaced with a solid element and the performances are compared. The laminated rotor features higher efficiency and higher power factor however being limited at the speed level considered. The robustness of solid rotor induction machines enables them to challenge the other topologies when comes to operate at peripheral speed above 300 [$^m/_s$]. Performance improvement can be achieved considering multi-layer structure and the optimum design is achieved only when considering the impact of the various disciplines involved in the behaviour of induction machines at high rotational speed.

BIBLIOGRAPHY

[1] T. Aho, V. Sihvo, J. Nerg, and J. Pyrhonen, "Rotor materials for medium-speed solid-rotor induction motors," in *2007 IEEE International Electric Machines Drives Conference*, vol. 1, pp. 525–530, May 2007.

[2] T. R. Hawkins, O. M. Gausen, and A. H. Stromman, "Environmental impacts of hybrid and electric vehicles - a review," *The International Journal of Life Cycle Assessment*, vol. 17, no. 8, pp. 997–1014, 2012.

[3] A. K. Sehra and W. Whitlow, "Propulsion and power for 21st century aviation," *Progress in Aerospace Sciences*, vol. 40, no. 4, pp. 199–235, 2004.

[4] R. Abebe, M. D. Nardo, D. Gerada, G. L. Calzo, L. Papini, and C. Gerada, "High speed drives review: Machines, converters and applications," in *IECON 2016 - 42nd Annual Conference of the IEEE Industrial Electronics Society*, pp. 1675–1679, Oct 2016.

[5] D. Gerada, A. Mebarki, N. L. Brown, C. Gerada, A. Cavagnino, and A. Boglietti, "High-speed electrical machines: Technologies, trends, and developments," *IEEE Transactions on Industrial Electronics*, vol. 61, pp. 2946–2959, June 2014.

[6] K. Reichert and G. Pasquarella, "High speed electric machines, status, trend and problems," in *IEEE/KTH Stockholm Tech. Conf., Stockholm, Sweden*, pp. 41–49, June 1995.

[7] S. Li and B. Sarlioglu, "Assessment of high-speed multi-megawatt electric machines," in *2015 IEEE International Electric Machines Drives Conference (IEMDC)*, pp. 1573–1579, May 2015.

[8] A. Boglietti, A. Cavagnino, A. Tenconi, and S. Vaschetto, "Key design aspects of electrical machines for high-speed spindle applications," in *IECON 2010 - 36th Annual Conference on IEEE Industrial Electronics Society*, pp. 1735–1740, Nov 2010.

[9] R. R. Moghaddam, "High speed operation of electrical machines, a review on technology, benefits and challenges," in *2014 IEEE Energy Conversion Congress and Exposition (ECCE)*, pp. 5539–5546, Sept 2014.

[10] A. Binder and T. Schneider, "High-speed inverter-fed ac drives," in *Electrical Machines and Power Electronics, 2007. ACEMP '07. International Aegean Conference on*, pp. 9–16, Sept 2007.

[11] J. B. Bartolo, H. Zhang, D. Gerada, L. D. Lillo, and C. Gerada, "High speed electrical generators, application, materials and design," in *Electrical Machines Design Control and Diagnosis (WEMDCD), 2013 IEEE Workshop on*, pp. 47–59, March 2013.

[12] J. D. v. M. R. D. van Millingen, "Phase shift torquemeters for gas turbine development and monitoring," in *Int. Gas Turbine Aeroengine Cong. Expo*, pp. 1–10, June 1991.

[13] M. Xiaohe, S. Rong, T. K. Jetl, W. Shuai, Z. Xiaolong, V. VaiyapurP, Gajanayake, Chandana, G. Amit, and N. Sivakumar, "Review of high speed electrical machines in gas turbine electrical power generation," in *TENCON 2015 - 2015 IEEE Region 10 Conference, Macao, 2015*, IEEE.

[14] L. B. D. C. Gildon, "Experience with high speed induction motors for direct driving compressors," in *27th Turbomachinery Symposium*, 1994. High power electrical machines.

[15] A. Tenconi, S. Vaschetto, and A. Vigliani, "Electrical machines for high-speed applications: Design considerations and tradeoffs," *IEEE Transactions on Industrial Electronics*, vol. 61, pp. 3022–3029, June 2014.

[16] S. Li, Y. Li, W. Choi, and B. Sarlioglu, "High-speed electric machines: Challenges and design considerations," *IEEE Transactions on Transportation Electrification*, vol. 2, pp. 2–13, March 2016.

[17] V. N. Antipov and Y. B. Danilevich, "High-speed electrical machines for power engineering: Current state and development trends," *Russian Electrical Engineering*, vol. 78, no. 6, pp. 277–279, 2007.

[18] M. A. Rahman, A. Chiba, and T. Fukao, "Super high speed electrical machines - summary," in *Power Engineering Society General Meeting, 2004. IEEE*, pp. 1272–1275 Vol.2, June 2004.

[19] D. P. Arnold, "Review of microscale magnetic power generation," *IEEE Transactions on Magnetics*, vol. 43, pp. 3940–3951, Nov 2007.

[20] N. Zabihi and R. Gouws, "A review on switched reluctance machines for electric vehicles," in *2016 IEEE 25th International Symposium on Industrial Electronics (ISIE)*, pp. 799–804, June 2016.

[21] C. Zwyssig, J. W. Kolar, and S. D. Round, "Megaspeed drive systems: Pushing beyond 1 million r/min," *IEEE/ASME Transactions on Mechatronics*, vol. 14, pp. 564–574, Oct 2009.

[22] S. Singhal, H. Walter, and T. Tyer, "Concept, design and testing of a 12mw 9500 rpm induction motor with oil film bearings for pipeline applications in north america," in *Industry Applications Society 60th Annual Petroleum and Chemical Industry Conference*, pp. 1–16, Sept 2013.

[23] B. M. Wood, C. L. Olsen, G. D. Hartzo, J. C. Rama, and F. R. Szenasi, "Development of an 11000-r/min 3500-hp induction motor and adjustable-speed drive for refinery service," *IEEE Transactions on Industry Applications*, vol. 33, pp. 815–825, May 1997.

[24] J. Pyrhonen, J. Nerg, P. Kurronen, and U. Lauber, "High-speed high-output solid-rotor induction-motor technology for gas compression," *IEEE Transactions on Industrial Electronics*, vol. 57, pp. 272–280, Jan 2010.

[25] J. Pyrhonen, J. Nerg, P. Kurronen, and U. Lauber, “High-speed, 8 mw, solid-rotor induction motor for gas compression,” in *Electrical Machines, 2008. ICEM 2008. 18th International Conference on*, pp. 1–6, Sept 2008.

[26] J. F. Gieras and J. Saari, “Performance calculation for a high-speed solid-rotor induction motor,” *IEEE Transactions on Industrial Electronics*, vol. 59, pp. 2689–2700, June 2012.

[27] A. Smirnov, N. Uzhegov, T. Sillanpaa, J. Pyrhonen, and O. P. Pyrhonen, “High-speed electrical machine with active magnetic bearing system optimization,” *IEEE Transactions on Industrial Electronics*, vol. PP, no. 99, pp. 1–1, 2017.

[28] J. Larjola, “Electricity from industrial waste heat using high-speed organic rankine cycle (orc),” *International Journal of Production Economics*, vol. 41, no. 1, pp. 227 – 235, 1995.

[29] D. Gerada, A. Mebarki, N. L. Brown, H. Zhang, and C. Gerada, “Design, modelling and testing of a high speed induction machine drive,” in *2012 IEEE Energy Conversion Congress and Exposition (ECCE)*, pp. 4649–4655, Sept 2012.

[30] L. Papini, D. Gerada, and C. Gerada, “Development and testing aspects of high speed induction machines,” in *2016 19th International Conference on Electrical Machines and Systems (ICEMS)*, pp. 1–6, Nov 2016.

[31] Y.-K. Kim, M.-C. Choi, K.-H. Suh, Y.-C. Ji, and D.-S. Wang, “High-speed induction motor development for small centrifugal compressor,” in *Electrical Machines and Systems, 2001. ICEMS 2001. Proceedings of the Fifth International Conference on*, vol. 2, pp. 891–894 vol.2, Aug 2001.

[32] J. Wilson, E. Erdelyi, and R. Hopkins, “Aerospace composite-rotor induction motors,” *IEEE Transactions on Aerospace*, no. 2, pp. 18–23, 1965.

[33] J. Barta, C. Ondrusek, P. Losak, and R. Vlach, “Design of high-speed induction machine for the 6 kw, 120 000 rpm helium turbo-circulator,” in *2016 XXII International Conference on Electrical Machines (ICEM)*, pp. 1552–1558, Sept 2016.

[34] M. T. Caprio, V. Lelos, and J. D. Herbst, "Design and stress analysis of a high speed rotor for an advanced induction motor," *CEM Publications*, 2016.

[35] M. van der Geest, H. Polinder, J. A. Ferreira, and M. Christmann, "Power density limits and design trends of high-speed permanent magnet synchronous machines," *IEEE Transactions on Transportation Electrification*, vol. 1, no. 3, pp. 266–276, 2015.

[36] L. Papini, T. Raminosoa, D. Gerada, and C. Gerada, "A high-speed permanent-magnet machine for fault-tolerant drivetrains," *IEEE Transactions on Industrial Electronics*, vol. 61, pp. 3071–3080, June 2014.

[37] A. Cavagnino, Z. Li, A. Tenconi, and S. Vaschetto, "Integrated generator for more electric engine: Design and testing of a scaled-size prototype," *IEEE Transactions on Industry Applications*, vol. 49, pp. 2034–2043, Sept 2013.

[38] D. K. Hong, B. C. Woo, J. Y. Lee, and D. H. Koo, "Ultra high speed motor supported by air foil bearings for air blower cooling fuel cells," *IEEE Transactions on Magnetics*, vol. 48, pp. 871–874, Feb 2012.

[39] D. Steinert, T. Nussbaumer, and J. W. Kolar, "Slotless bearingless disk drive for high-speed and high-purity applications," *IEEE Transactions on Industrial Electronics*, vol. 61, pp. 5974–5986, Nov 2014.

[40] R. P. Jastrzebski, P. Jaatinen, H. Sugimoto, O. Pyrhonen, and A. Chiba, "Design of a bearingless 100 kw electric motor for high-speed applications," in *Electrical Machines and Systems (ICEMS), 2015 18th International Conference on*, pp. 2008–2014, Oct 2015.

[41] G. R. Slemon, "Electrical machines for variable-frequency drives," *Proceedings of the IEEE*, vol. 82, no. 8, pp. 1123–1139, 1994.

[42] A. Maeda, H. Tomita, and O. Miyashita, "Power and speed limitations in high speed electrical machines," in *Proc. IPEC-Yokohama*, pp. 1321–1326, 1995.

[43] J. Gieras, *Advancements in Electric Machines.* Power Systems, Springer Netherlands, 2008.

[44] D. Gerada, A. Mebarki, N. L. Brown, H. Zhang, and C. Gerada, "Design, modelling and testing of a high speed induction machine drive," in *2012 IEEE Energy Conversion Congress and Exposition (ECCE)*, pp. 4649–4655, Sept 2012.

[45] A. Boglietti, A. Cavagnino, and M. Lazzari, "Modelling of the closed rotor slot effects in the induction motor equivalent circuit," in *Electrical Machines, 2008. ICEM 2008. 18th International Conference on*, pp. 1–4, Sept 2008.

[46] M. Caprio, V. Lelos, J. Herbst, S. Manifold, and H. Jordon, "High strength induction machine, rotor, rotor cage end ring and bar joint, rotor end ring, and related methods," Mar. 17 2009. US Patent 7,504,756.

[47] Y. Mekuria, *Development of a High Speed Solid Rotor Asynchronous Drive fed by a Frequency Converter System.* PhD thesis, Dissertation, Technische Universität Darmstadt, 01.02, 2013.

[48] T. Aho, J. Nerg, and J. Pyrhonen, "The effect of the number of rotor slits on the performance characteristics of medium-speed solid rotor induction motor," in *The 3rd IET International Conference on Power Electronics, Machines and Drives, 2006. PEMD 2006*, pp. 515–519, April 2006.

[49] M. Ito, K. Arai, N. Takahashi, H. Kiwaki, and T. Seya, "Magnetically anisotropic solid rotor of an induction motor," *IEEE Transactions on Energy Conversion*, vol. 3, pp. 427–432, Jun 1988.

[50] M. S. Sarma and G. R. Soni, "Solid-rotor and composite-rotor induction machines," *IEEE Transactions on Aerospace and Electronic Systems*, vol. AES-8, pp. 147–155, March 1972.

[51] A. Arkkio *et al.*, *Analysis of induction motors based on the numerical solution of the magnetic field and circuit equations.* Helsinki University of Technology, 1987.

[52] L. Alberti, N. Bianchi, and S. Bolognani, "A very rapid prediction of im performance combining analytical and finite-element analysis," *IEEE Transactions on Industry Applications*, vol. 44, pp. 1505–1512, Sept 2008.

[53] K. Boughrara, F. Dubas, and R. Ibtiouen, "2-d analytical prediction of eddy currents, circuit model parameters, and steady-state performances in solid rotor induction motors," *IEEE Transactions on Magnetics*, vol. 50, pp. 1–14, Dec 2014.

[54] R. Ibtiouen, R. Kechroud, O. Touhami, and S. Mekhtoub, "Complex finite element analysis of a solid rotor induction motor," in *Electric Machines and Drives Conference, 2003. IEMDC'03. IEEE International*, vol. 3, pp. 1606–1610 vol.3, June 2003.

[55] D. Marcsa and M. Kuczmann, "Comparison of the $mbiA^{*}-mbiA$ and $mbiT, phi-phi$ formulations for the 2-d analysis of solid-rotor induction machines," *IEEE Transactions on Magnetics*, vol. 45, pp. 3329–3333, Sept 2009.

[56] J. Pyrhonen, *The high-speed induction motor: Calculating the effects of solid-rotor material on machine characteristics.* the Finnish Academy of Technology, 1991.

[57] J. Huppunen *et al.*, *High-speed solid-rotor induction machine - Electromagnetic calculation and design.* Lappeenranta University of Technology, 2004.

[58] J. Driesen and R. Belmans, "Specific problems of high speed electrical drives," in *Micro-Gas Turbine*, pp. 12–1, 12–6, 2005.

[59] J. Saari, *Thermal analysis of high-speed induction machines.* PhD thesis, Helsinki University of Technology, Laboratory of Electro-mechanics, 1998.

[60] A. Damiano, A. Floris, G. Fois, M. Porru, and A. Serpi, "Modelling and design of pm retention sleeves for high-speed pm synchronous machines," in *2016 6th International Electric Drives Production Conference (EDPC)*, pp. 118–125, Nov 2016.

[61] F. Zhang, G. Du, T. Wang, G. Liu, and W. Cao, “Rotor retaining sleeve design for a 1.12-mw high-speed pm machine,” *IEEE Transactions on Industry Applications*, vol. 51, pp. 3675–3685, Sept 2015.

[62] W. Li, H. Qiu, X. Zhang, J. Cao, S. Zhang, and R. Yi, “Influence of rotor-sleeve electromagnetic characteristics on high-speed permanent-magnet generator,” *IEEE Transactions on Industrial Electronics*, vol. 61, pp. 3030–3037, June 2014.

[63] T. Epskamp, B. Butz, and M. Doppelbauer, “Design and analysis of a high-speed induction machine as electric vehicle traction drive,” in *2016 18th European Conference on Power Electronics and Applications (EPE’16 ECCE Europe)*, pp. 1–10, Sept 2016.

[64] J. F. Gieras, “Multimegawatt synchronous generators for airborne applications: A review,” in *Electric Machines & Drives Conference (IEMDC), 2013 IEEE International*, pp. 626–633, IEEE, 2013.

[65] J. Pyrhonen, T. Jokinen, and V. Hrabovcova, *Design of Rotating Electrical Machines.* Wiley, 2009.

[66] J. Le Besnerais, V. Lanfranchi, M. Hecquet, and P. Brochet, “Characterization of the audible magnetic noise emitted by traction motors in railway rolling stock,” *Noise Control Engineering Journal*, vol. 57, no. 5, pp. 391–399, 2009.

[67] E. L. Owen, “Flexible shaft versus rigid shaft electric machines for petroleum and chemical plants,” *IEEE Transactions on Industry Applications*, vol. 27, pp. 245–253, Mar 1991.

[68] S. Singhal, “Vibration and rotor dynamics of large high-speed motors driving compressors in the oil and gas industry,” in *Petroleum and Chemical Industry Technical Conference (PCIC), 2012 Record of Conference Papers Industry Applications Society 59th Annual IEEE*, pp. 1–12, Sept 2012.

[69] A. Boglietti, P. Ferraris, M. Lazzari, and F. Profumo, “About the design of very high frequency induction motors for spindle applications,” in

Industry Applications Society Annual Meeting, 1992., Conference Record of the 1992 IEEE, pp. 25–32 vol.1, Oct 1992.

[70] "Balance quality requirements of rigid rotors." ISO 1940-1, 2003.

[71] Y. M. Grekov, I. I. Radchik, E. S. Trunin, and O. V. Bol'shakov, "Balancing a high-speed rotor on a balancing machine," *Power Technology and Engineering*, vol. 49, no. 1, pp. 57–60, 2015.

[72] M. Friswell, *Dynamics of Rotating Machines.* Cambridge Aerospace Series, Cambridge University Press, 2010.

[73] A. Borisavljevic, H. Polinder, and B. Ferreira, "Overcoming limits of high-speed pm machines," in *2008 18th International Conference on Electrical Machines*, 2008.

[74] *SKF Uk Ltd., Bearing in centrifugal pumps - Application Handbook.* http://www.skf.com/binary/26-154513/100-955-Bearings-in-centrifugal-pumps.pdf.

[75] H. Mizumoto, S. Arii, Y. Yabuta, and Y. Tazoe, "Vibration control of a high-speed air-bearing spindle using an active aerodynamic bearing," in *Control Automation and Systems (ICCAS), 2010 International Conference on*, pp. 2261–2264, Oct 2010.

[76] A. Looser and J. W. Kolar, "An active magnetic damper concept for stabilization of gas bearings in high-speed permanent-magnet machines," *IEEE Transactions on Industrial Electronics*, vol. 61, pp. 3089–3098, June 2014.

[77] G. Schweitzer, "Applications and research topics for active magnetic bearings," in *IUTAM Symposium on Emerging Trends in Rotor Dynamics*, pp. 263–273, Springer, 2011.

[78] C. R. Knospe, "Active magnetic bearings for machining applications," *Control Engineering Practice*, vol. 15, no. 3, pp. 307 – 313, 2007. Selected Papers Presented at the Third {IFAC} Symposium on Mechatronic Systems (2004)Third {IFAC} Symposium on Mechatronic Systems.

[79] X. Xie, "Comparison of bearings: For the bearing choosing of high-speed spindle design," *Dept. of Mechanical Engineering, U. of Utah*, 2003.

[80] G. Tornquist, R. Borden, J. Lengel, G. McDowall, and K. Doherty, "Rotor end caps and a method of cooling a high speed generator," May 11 2004. US Patent 6,734,585.

[81] E. Zysset, "Liquid cooled asynchronous electric machine," Feb. 20 2001. US Patent 6,191,511.

[82] P. Zhou, N. Kalayjian, G. Cutler, and P. Augenbergs, "Liquid cooled rotor assembly," Feb. 10 2009. US Patent 7,489,057.

[83] M. Schiefer and M. Doppelbauer, "Indirect slot cooling for high-power-density machines with concentrated winding," in *2015 IEEE International Electric Machines Drives Conference (IEMDC)*, pp. 1820–1825, May 2015.

[84] A. L. Rocca, Z. Xu, P. Arumugam, S. J. Pickering, C. N. Eastwick, C. Gerada, and S. Bozhko, "Thermal management of a high speed permanent magnet machine for an aeroengine," in *2016 XXII International Conference on Electrical Machines (ICEM)*, pp. 2732–2737, Sept 2016.

[85] A. Arkkio, "Asynchronous electric machine and rotor and stator for use in association therewith," Dec. 5 1995. US Patent 5,473,211.

[86] A. Boglietti, A. Cavagnino, and D. Staton, "Determination of critical parameters in electrical machine thermal models," *IEEE Transactions on Industry Applications*, vol. 44, pp. 1150–1159, July 2008.

[87] A. Boglietti, E. Carpaneto, M. Cossale, A. L. Borlera, D. Staton, and M. Popescu, "Electrical machine first order short-time thermal transients model: Measurements and parameters evaluation," in *IECON 2014 - 40th Annual Conference of the IEEE Industrial Electronics Society*, pp. 555–561, Oct 2014.

[88] L. Alberti and N. Bianchi, "A coupled thermal - electromagnetic analysis for a rapid and accurate prediction of im performance," *IEEE Transactions on Industrial Electronics*, vol. 55, pp. 3575–3582, Oct 2008.

[89] C. Sciascera, P. Giangrande, L. Papini, C. Gerada, and M. Galea, "Analytical thermal model for fast stator winding temperature prediction," *IEEE Transactions on Industrial Electronics*, vol. 64, pp. 6116–6126, Aug 2017.

[90] M. R. Shah and S. B. Lee, "Rapid analytical optimization of eddy-current shield thickness for associated loss minimization in electrical machines," *IEEE Transactions on Industry Applications*, vol. 42, pp. 642–649, May 2006.

[91] D. A. Howey, P. R. N. Childs, and A. S. Holmes, "Air-gap convection in rotating electrical machines," *IEEE Transactions on Industrial Electronics*, vol. 59, pp. 1367–1375, March 2012.

[92] G. I. Taylor, "Stability of a viscous liquid contained between two rotating cylinders," *Philosophical Transactions of the Royal Society of London A: Mathematical, Physical and Engineering Sciences*, vol. 223, no. 605-615, pp. 289–343, 1923.

[93] A. Krings, M. Cossale, A. Tenconi, J. Soulard, A. Cavagnino, and A. Boglietti, "Characteristics comparison and selection guide for magnetic materials used in electrical machines," in *2015 IEEE International Electric Machines Drives Conference (IEMDC)*, pp. 1152–1157, May 2015.

[94] A. Krings and J. Soulard, "Overview and comparison of iron loss models for electrical machines," *Journal of Electrical Engineering*, vol. 10, no. 3, pp. 162–169, 2010. Updated and revised version of conference paper from the 5th International Conference and Exhibition on Ecological Vehicles and Renewable Energies (EVER 10), Monte-Carlo, MONACO, MAR 25-28, 2010QC 20120120.

[95] P. L. and G. C., "Analytical-numerical modelling of solid rotor induction machine," in *ELECTRIMACS 2014, 19th-22ndMay 2014, Valencia, Spain*, 2014.

[96] L. Papini and C. Gerada, "Thermal-electromagnetic analysis of solid rotor induction machine," in *7th IET International Conference on Power Electronics, Machines and Drives (PEMD 2014)*, pp. 1–6, April 2014.

[97] L. Papini, C. Gerada, D. Gerada, and A. Mebarki, "High speed solid rotor induction machine: Analysis and performances," in *2014 17th International Conference on Electrical Machines and Systems (ICEMS)*, pp. 2759–2765, Oct 2014.

[98] L. Papini and C. Gerada, "Sensitivity analysis of magnetizing inductance in solid rotor induction machine," in *2016 19th International Conference on Electrical Machines and Systems (ICEMS)*, pp. 1–6, Nov 2016.

[99] L. Papini and C. Gerada, "Sensitivity analysis of rotor parameters in solid rotor induction machine," in *2017 International Electric Machines and Drives Conference (IEMDC)*, May 2017.

[100] L. D. Landau and E. M. Lifshitz, *Mechanics and electrodynamics*. Elsevier, 2013.

[101] P. Bolognesi, "A mid-complexity analysis of long-drum-type electric machines suitable for circuital modeling," in *2008 18th International Conference on Electrical Machines*, pp. 1–5, Sept 2008.

[102] L. D. Landau and E. M. Lifshitz, *Mechanics and electrodynamics*. Elsevier, 2013.

[103] R. P. Feynman, R. B. Leighton, and M. L. Sands, *The Feynman Lectures on Physics: Vol. 2: The Electromagnetic Field*. Addison-Wesley, 1965.

[104] L. D. Landau, *The classical theory of fields*, vol. 2. Elsevier, 2013.

[105] V. Raisanen, S. Suuriniemi, S. Kurz, and L. Kettunen, "Rapid computation of harmonic eddy-current losses in high-speed solid-rotor induction machines," *IEEE Transactions on Energy Conversion*, vol. 28, pp. 782–790, Sept 2013.

[106] P. D. Agarwal, "Eddy-current losses in solid and laminated iron," *Transactions of the American Institute of Electrical Engineers, Part I: Communication and Electronics*, vol. 78, pp. 169–181, May 1959.

[107] A. J. Wood and C. Concordia, “An analysis of solid rotor machines part iv. an approximate nonlinear analysis,” *Transactions of the American Institute of Electrical Engineers. Part III: Power Apparatus and Systems*, vol. 79, pp. 26–31, April 1960.

[108] D. O’Kelly, “Theory and performance of solid - rotor induction and hysteresis machines,” *Electrical Engineers, Proceedings of the Institution of*, vol. 123, pp. 421–428, May 1976.

[109] M. Fratila, A. Benabou, A. Tounzi, and M. Dessoude, “Calculation of iron losses in solid rotor induction machine using fem,” *IEEE Transactions on Magnetics*, vol. 50, pp. 825–828, Feb 2014.

[110] J. Gieras, “Analytical method of calculating the electromagnetic field and power losses in ferromagnetic halfspace, taking into account saturation and hysteresis,” *Proceedings of the IEEE*, vol. 124, no. 11, pp. 1098–1104, 1977.

[111] A. J. Wood and C. Concordia, “An analysis of solid rotor machines part ii. the effects of curvature,” *Transactions of the American Institute of Electrical Engineers. Part III: Power Apparatus and Systems*, vol. 78, pp. 1666–1672, Dec 1959.

[112] L. Zhang, “The finite difference method for the helmholtz equation with applications to cloaking,”

[113] Y. A. Erlangga, “Advances in iterative methods and preconditioners for the helmholtz equation,” *Archives of Computational Methods in Engineering*, vol. 15, no. 1, pp. 37–66, 2008.

[114] L. N. Trefethen, *Spectral methods in MATLAB*. SIAM, 2000.

[115] T. Lubin, S. Mezani, and A. Rezzoug, “Analytic calculation of eddy currents in the slots of electrical machines: Application to cage rotor induction motors,” *IEEE Transactions on Magnetics*, vol. 47, pp. 4650–4659, Nov 2011.

[116] M. Abramowitz and I. Stegun, “Handbook of mathematical functions, new york,” *NY: Dover Publications*, 1972.

[117] M. Benzi, "Preconditioning techniques for large linear systems: a survey," *Journal of computational Physics*, vol. 182, no. 2, pp. 418–477, 2002.

[118] S. Basu and P. Mukhopadhyay, "Analysis of solid-rotor induction machine," *India, IEE-IERE Proceedings* -, vol. 10, pp. 87–93, May 1972.

[119] T. Aho *et al.*, "Electromagnetic design of a solid steel rotor motor for demanding operation environments," *Acta Universitatis Lappeenrantaensis*, 2007.

[120] S. Zhu, M. Cheng, J. Dong, and J. Du, "Core loss analysis and calculation of stator permanent-magnet machine considering dc-biased magnetic induction," *IEEE Transactions on Industrial Electronics*, vol. 61, pp. 5203–5212, Oct 2014.

[121] J. A. Ferreira, "Improved analytical modeling of conductive losses in magnetic components," *IEEE Transactions on Power Electronics*, vol. 9, pp. 127–131, Jan 1994.

[122] X. Tang and C. R. Sullivan, "Optimization of stranded-wire windings and comparison with litz wire on the basis of cost and loss," in *2004 IEEE 35th Annual Power Electronics Specialists Conference (IEEE Cat. No.04CH37551)*, vol. 2, pp. 854–860 Vol.2, June 2004.

[123] S. Guo, L. Zhou, and T. Yang, "An analytical method for determining circuit parameter of a solid rotor induction motor," in *2012 15th International Conference on Electrical Machines and Systems (ICEMS)*, pp. 1–6, Oct 2012.

[124] K. J. Meessen, J. J. H. Paulides, and E. A. Lomonova, "Force calculations in 3-d cylindrical structures using fourier analysis and the maxwell stress tensor," *IEEE Transactions on Magnetics*, vol. 49, pp. 536–545, Jan 2013.

[125] S. Elia, M. Pasquali, G. Remigi, M. Sabene, and E. Santini, "A modified maxwell stress tensor method for the evaluation of electromagnetic torque," *WIT Transactions on Engineering Sciences*, vol. 31, 2001.

[126] A. Bermudez, A. L. Rodriguez, and I. Villar, "Extended formulas to compute resultant and contact electromagnetic force and torque from maxwell stress tensors," *IEEE Transactions on Magnetics*, vol. 53, pp. 1–9, April 2017.

[127] M. Markovic and Y. Perriard, "An analytical solution for the torque and power of a solid-rotor induction motor," in *2011 IEEE International Electric Machines Drives Conference (IEMDC)*, pp. 1053–1057, May 2011.

[128] O. Aglen, "Loss calculation and thermal analysis of a high-speed generator," in *Electric Machines and Drives Conference, 2003. IEMDC'03. IEEE International*, vol. 2, pp. 1117–1123 vol.2, June 2003.

[129] D. Zhang, F. Wang, and X. Kong, "Air friction loss calculation of high speed permanent magnet machines," in *2008 International Conference on Electrical Machines and Systems*, pp. 320–323, Oct 2008.

[130] K. Nakabayashi, Y. Yamada, and T. Kishimoto, "Viscous frictional torque in the flow between two concentric rotating rough cylinders," *Journal of fluid mechanics*, vol. 119, pp. 409–422, 1982.

[131] T. Garbiec, "Fast computation of performance characteristics for solid-rotor induction motors with electrically inhomogenous rotors," *IEEE Transactions on Energy Conversion*, vol. PP, no. 99, pp. 1–1, 2016.

[132] T. Aho, J. Nerg, and J. Pyrhonen, "Experimental and finite element analysis of solid rotor end effects," in *2007 IEEE International Symposium on Industrial Electronics*, pp. 1242–1247, June 2007.

[133] S. Wang, Z. Huang, Y. Sun, and H. Cao, "Rotor end factors for 2-d fea of induction motors with smooth or slitted solid rotor," *CES Transactions on Electrical Machines and Systems*, vol. 1, no. 2, pp. 132–139, 2017.

[134] J. J. Pyrhonen, J. K. Nerg, T. Aho, and P. T. Kurronen, "Solid rotor end effects - analytic and experimental results for high-power high-speed machines," in *IEEE EUROCON 2009*, pp. 688–695, May 2009.

[135] R. L. Russell and K. H. Norsworthy, "Eddy currents and wall losses in screened-rotor induction motors," *Proceedings of the IEE - Part A: Power Engineering*, vol. 105, pp. 163–175, April 1958.

[136] W. Gibbs, "Induction and synchronous motors with unlaminated rotors," *Journal of the Institution of Electrical Engineers-Part II: Power Engineering*, vol. 95, no. 46, pp. 411–420, 1948.

[137] H. Yee and T. Wilson, "Saturation and finite-length effects in solid-rotor induction machines," *Electrical Engineers, Proceedings of the Institution of*, vol. 119, pp. 877–882, July 1972.

[138] T. Aho, J. Nerg, and J. Pyrhonen, "Optimizing the axial length of the slitted solid iron rotor," in *2007 2nd IEEE Conference on Industrial Electronics and Applications*, pp. 255–259, May 2007.

[139] Z. Xu, M. Galea, C. Tighe, T. Hamiti, C. Gerada, and S. J. Pickering, "Mechanical and thermal management design of a motor for an aircraft wheel actuator," in *2014 17th International Conference on Electrical Machines and Systems (ICEMS)*, pp. 3268–3273, Oct 2014.

[140] Y. Zhang, S. McLoone, W. Cao, F. Qiu, and C. Gerada, "Power loss and thermal analysis of a mw high speed permanent magnet synchronous machine," *IEEE Transactions on Energy Conversion*, vol. PP, no. 99, pp. 1–1, 2017.

[141] M. A. Vogelsberger, J. Buschbeck, A. Orellano, E. Schmidt, and M. Bazant, "Electromagnetic 2014; thermal coupled optimization of high power traction drive induction machines," in *IECON 2014 - 40th Annual Conference of the IEEE Industrial Electronics Society*, pp. 562–568, Oct 2014.

[142] A. Tuysuz, F. Meyer, M. Steichen, C. Zwyssig, and J. W. Kolar, "Advanced cooling methods for high-speed electrical machines," *IEEE Transactions on Industry Applications*, vol. 53, pp. 2077–2087, May 2017.

[143] J. Borg Bartolo, *A high performance switched reluctance drive for aerospace applications.* PhD thesis, University of Nottingham, 2016.

[144] S. Nategh, *Thermal analysis and management of high-performance electrical machines.* PhD thesis, KTH Royal Institute of Technology, 2013.

[145] A. Boglietti, A. Cavagnino, M. Lazzari, and M. Pastorelli, "A simplified thermal model for variable-speed self-cooled industrial induction motor," *IEEE Transactions on Industry Applications*, vol. 39, pp. 945–952, July 2003.

[146] C. Kral, A. Haumer, M. Haigis, H. Lang, and H. Kapeller, "Comparison of a cfd analysis and a thermal equivalent circuit model of a tefc induction machine with measurements," *IEEE Transactions on Energy Conversion*, vol. 24, pp. 809–818, Dec 2009.

[147] A. Boglietti, A. Cavagnino, D. Staton, M. Shanel, M. Mueller, and C. Mejuto, "Evolution and modern approaches for thermal analysis of electrical machines," *IEEE Transactions on Industrial Electronics*, vol. 56, pp. 871–882, March 2009.

[148] J. R. Mayor and S. A. Semidey, "Generic electric machine thermal model development using an automated finite difference approach," in *2009 IEEE International Electric Machines and Drives Conference*, pp. 137–143, May 2009.

[149] M. Kaminski, "The use of the finite differences method to solve nonlinear equation of thermal conduction," in *Proceedings of the International Conference Modern Problems of Radio Engineering, Telecommunications and Computer Science, 2004.*, pp. 52–55, Feb 2004.

[150] N. Hay, D. Lampard, S. J. Pickering, and T. F. Roylance, "Convection heat transfer correlations relevant to cooling situations in electric motors," 1993 1993.

[151] A. Boglietti and A. Cavagnino, "Analysis of the endwinding cooling effects in tefc induction motors," *IEEE Transactions on Industry Applications*, vol. 43, pp. 1214–1222, Sept 2007.

[152] M. Popescu, D. A. Staton, A. Boglietti, A. Cavagnino, D. Hawkins, and J. Goss, "Modern heat extraction systems for power traction machines: A

review," *IEEE Transactions on Industry Applications*, vol. 52, pp. 2167–2175, May 2016.

[153] M. Galea, C. Gerada, T. Raminosoa, and P. Wheeler, "A thermal improvement technique for the phase windings of electrical machines," *IEEE Transactions on Industry Applications*, vol. 48, Jan 2012.

[154] A. Boglietti, A. Cavagnino, and D. Staton, "Determination of critical parameters in electrical machine thermal models," *IEEE Transactions on Industry Applications*, vol. 44, no. 4, pp. 1150–1159, 2008.

[155] M. Fenot, Y. Bertin, E. Dorignac, and G. Lalizel, "A review of heat transfer between concentric rotating cylinders with or without axial flow," *International Journal of Thermal Sciences*, vol. 50, no. 7, pp. 1138 – 1155, 2011.

[156] R. J. Fritz, "The effects of an annular fluid on the vibrations of a long rotor, part 1 - theory," *Journal of Basic Engineering*, vol. 92, pp. 923–929, Dec 1970.

[157] K. M. Becker and J. Kaye, "Measurements of diabatic flow in an annulus with an inner rotating cylinder," *Journal of Heat Transfer*, vol. 84, pp. 97–104, May 1962.

[158] R. Larsonneur, *Design and control of active magnetic bearing systems for high speed rotation.* PhD thesis, 1990.

[159] D. Xu, X. Wang, and G. Li, "Optimization design of the sleeve for high speed permanent magnet machine," in *2016 IEEE 11th Conference on Industrial Electronics and Applications (ICIEA)*, June 2016.

[160] A. Damiano, A. Floris, G. Fois, M. Porru, and A. Serpi, "Modelling and design of pm retention sleeves for high-speed pm synchronous machines," in *2016 6th International Electric Drives Production Conference (EDPC)*, pp. 118–125, Nov 2016.

[161] E. J. Hearn, *Mechanics of Materials 2: The mechanics of elastic and plastic deformation of solids and structural materials.* Butterworth-Heinemann, 1997.

[162] D. Gerada, *High speed electrical machines for the more-electric engine.* PhD thesis, University of Nottingham, 2012.

[163] T. Wang, F. Wang, H. Bai, and J. Xing, "Optimization design of rotor structure for high speed permanent magnet machines," in *Electrical Machines and Systems, 2007. ICEMS. International Conference on*, pp. 1438–1442, IEEE, 2007.

[164] T. Wang, F. Wang, H. Bai, and J. Xing, "Optimization design of rotor structure for high speed permanent magnet machines," in *2007 International Conference on Electrical Machines and Systems (ICEMS)*, pp. 1438–1442, Oct 2007.

[165] A. Labuschagne, N. van Rensburg, and A. van der Merwe, "Comparison of linear beam theories," *Mathematical and Computer Modelling*, vol. 49, no. 1, pp. 20 – 30, 2009.

[166] S. M. Han, H. Benaroya, and T. Wei, "Dynamics of transversely vibrating beams using four engineering theories," *Journal of sound and vibration*, vol. 225, no. 5, pp. 935–988, 1999.

[167] N. van Rensburg and A. van der Merwe, "Natural frequencies and modes of a timoshenko beam," *Wave Motion*, vol. 44, no. 1, pp. 58 – 69, 2006.

[168] J. Akpobi and C. Ovuworie, "Computer–aided design of the critical speed of shafts," *Journal of Applied Sciences and Environmental Management*, vol. 12, no. 4, 2008.

[169] S. Bashash, A. Salehi-Khojin, and N. Jalili, "Forced vibration analysis of flexible euler-bernoulli beams with geometrical discontinuities," in *2008 American Control Conference*, pp. 4029–4034, June 2008.

[170] E. Dikmen, *Multiphysical effects on high-speed rotordynamics.* University of Twente, 2010.

[171] S. Naguleswaran, "Vibration of an euler–bernoulli beam on elastic end supports and with up to three step changes in cross-section," *International journal of mechanical sciences*, vol. 44, no. 12, pp. 2541–2555, 2002.

[172] D. Genovese, P. Bolognesi, M. D. Martin, and F. Luise, "A contextual parameter identification method for the equivalent circuit of induction machine," in *2016 XXII International Conference on Electrical Machines (ICEM)*, pp. 25–31, Sept 2016.

[173] J. R. Bumby, E. Spooner, and M. Jagiela, "Equivalent circuit analysis of solid-rotor induction machines with reference to turbocharger accelerator applications," *IEE Proceedings - Electric Power Applications*, vol. 153, pp. 31–39, Jan 2006.

[174] IEEE, "Ieee standard test procedure for polyphase induction motors and generators," *IEEE Std 112-2004 (Revision of IEEE Std 112-1996)*, pp. 1–79, 2004.

[175] M. Jesenik, A. Hamler, P. Kitak, and M. Trlep, "Parameters for expressing an analytical magnetization curve obtained using a genetic algorithm," *a a*, vol. 2, no. 1, p. 1, 2013.

[176] M. D. Martin, M. Bailoni, A. Tessarolo, M. Bortolozzi, D. Giulivo, F. Agnolet, and R. Santarossa, "Investigation into induction motor equivalent circuit parameter dependency on current and frequency variations," in *2014 International Conference on Electrical Machines (ICEM)*, pp. 196–202, Sept 2014.

[177] O. Chiver, E. Micu, and C. Barz, "Stator winding leakage inductances determination using finite elements method," in *2008 11th International Conference on Optimization of Electrical and Electronic Equipment*, pp. 69–74, May 2008.

[178] "En24 material properties." http://asm.matweb.com/.

[179] Z. Q. Zhu and D. Howe, "Instantaneous magnetic field distribution in brushless permanent magnet dc motors. iii. effect of stator slotting," *IEEE Transactions on Magnetics*, vol. 29, pp. 143–151, Jan 1993.

[180] I. Boldea and S. A. Nasar, *The induction machine handbook*. CRC press, 2010.